

MATER. TEHNOL.	LETNIK VOLUME	45	ŠTEV. NO.	4	STR. P.	293–378	LJUBLJANA SLOVENIJA	JULY–AUG. 2011
-------------------	------------------	----	--------------	---	------------	---------	------------------------	-------------------

## VSEBINA – CONTENTS

### PREGLIEDNI ČLANKI – REVIEW ARTICLES

#### High-strength low-alloy (HSLA) steels

Visokotrдна malolegirana (HSLA) konstrukcijska jekla

D. A. Skobir ..... 295

#### TEM investigation of metallic materials – an advanced technique in materials science and metallurgy

Preiskave kovinskih materialov s presevno elektronsko mikroskopijo – moderna tehnika v znanosti o materialih in metalurgiji

D. Jenko ..... 303

### IZVIRNI ZNANSTVENI ČLANKI – ORIGINAL SCIENTIFIC ARTICLES

#### Modelling of hot tears in continuously cast steel

Modeliranje vročih razpok v kontinuirno litem jeklu

V. Grozdanić ..... 311

#### Thermodynamic investigation of the Al-Sb-Zn system

Termodinamska raziskava sistema Al-Sb-Zn

G. Klančnik, J. Medved ..... 317

#### XPS and SEM of unpolished and polished FeS surface

Rentgenska fotoelektronska spektroskopija in vrstična elektronska mikroskopija nepolirane in polirane površine FeS

Dj. Mandrino ..... 325

#### Surface characterization and pickling characteristics of the oxide scale on duplex stainless steel

Površinska karakterizacija in lastnosti luženja oksidne plasti na dupleksnem nerjavnem jeklu

Č. Donik ..... 329

#### CFD analysis of exothermic reactions in Al-Au nano multi-layered foils

CFD-analiza eksotermnih reakcij v večplastnih nanofolijah Al-Au

K. T. Raić, R. Rudolf, P. Ternik, Z. Žunič, V. Lazić, D. Stamenković, T. Tanasković, I. Anžel ..... 335

#### Microstructure evolution in SAF 2507 super duplex stainless steel

Razvoj mikrostrukture v superdupleksnem nerjavnem jeklu SAF 2507

F. Tehovnik, B. Arzenšek, B. Arh, D. Skobir, B. Pirnar, B. Žužek ..... 339

#### Optimization of the quality of continuously cast steel slabs using the Firefly algorithm

Optimizacija kakovosti kontinuirno lite jeklene plošče z uporabo algoritma "Firefly"

T. Mauder, C. Sandera, J. Stetina, M. Seda ..... 347

#### Hot workability of 95MnWCr5 tool steel

Vroča preoblikovalnost orodnega jekla 95MnWCr5

A. Križaj, M. Fazarinc, M. Jenko, P. Fajfar ..... 351

#### Lifetime evaluation of a steam pipeline using NDE methods

Ocena preostale trajnostne dobe parovoda z uporabo neporušitvenih preiskav (NDE)

F. Kafexhiu, J. Vojvodić Tuma ..... 357

#### The influence of the chemical composition of steels on the numerical simulation of a continuously cast slab

Vpliv kemične sestave jekel na numerično simulacijo kontinuirno lite plošče

J. Stetina, F. Kavicka ..... 363

#### Prediction of the mechanical properties of cast Cr-Ni-Mo stainless steels with a two-phase microstructure

Napoved mehanskih lastnosti litih Cr-Ni-Mo nerjavnih jekel z dvofazno mikrostrukuro

M. Malešević, J. V. Tuma, B. Šuštaršič, P. Borković ..... 369

#### Relationship between mechanical strength and Young's modulus in traditional ceramics

Odvisnost med mehansko trdnostjo in Youngovim modulom pri tradicionalni keramiki

I. Štubňa, A. Trnák, P. Šín, R. Sokolář, I. Medved' ..... 375

#### 19. KONFERENCA O MATERIALIH IN TEHNOLOGIJAH, 22. – 23. november 2011, Portorož, Slovenija

19<sup>th</sup> CONFERENCE ON MATERIALS AND TECHNOLOGY, November 22–23, 2011, Portorož, Slovenia ..... 379



# HIGH-STRENGTH LOW-ALLOY (HSLA) STEELS

## VISOKOTRDNNA MALOLEGIRANA (HSLA) KONSTRUKCIJSKA JEKLA

**Danijela A. Skobir**

Institute of Metals and Technology, Lepi pot 11, 1000 Ljubljana, Slovenia  
danijela.skobir@imt.si

*Prejem rokopisa – received: 2011-05-09; sprejem za objavo – accepted for publication: 2011-07-04*

Micro-alloyed, high-strength, low-alloy (HSLA) steels are important structural materials and contain small amounts of alloying elements, such as niobium, titanium, vanadium, and aluminium, which enhance the strength through the formation of stable carbides, nitrides or carbonitrides and have an effect on the hardenability. Such steels contain less than 0.1 % of the alloying additions, used individually or in combination. Yield strength increments of two or three times that of plain carbon-manganese steel can be attained. Nowadays, also micro-alloyed cast steels have found many applications in the manufacturing of industrial parts that used to be produced by more expensive manufacturing processes.

Keywords: high-strength low-alloy (HSLA) steels, micro-alloying elements, carbides, nitrides, carbonitrides, mechanical properties

Visokotrдна malolegirana konstrukcijska jekla (HSLA) spadajo med tehnično pomembne konstrukcijske materiale in vsebujejo majhne količine legirnih elementov, kot so niobij, titan, vanadij, aluminij, ki zaradi tvorbe stabilnih karbidov, nitridov ali karbonitridov zvišajo natezno trdnost materiala in vplivajo na trdnost. Ta jekla vsebujejo manj kot 0.1 % legirnih elementov, ki se lahko uporabljajo posamezno ali v kombinaciji, natezna trdnost pa je lahko dva do trikrat višja kot pri navadnem ogljikovo-manganovem jeklu. Danes so v uporabi tudi mikrolegirana lita jekla, ki se največ uporabljajo za izdelavo raznih industrijskih delov, za kar so bili prej potrebni dragi proizvodni procesi.

Ključne besede: visokotrдна malolegirana jekla (HSLA), mikrolegirni elementi, karbidi, nitridi, karbonitridi, mehanske lastnosti

### 1 INTRODUCTION

High-strength, low-alloy (HSLA) steels, or micro-alloyed steels, are aimed to provide better mechanical properties and/or greater resistance to atmospheric corrosion than conventional carbon steels. They are designed to meet specific mechanical properties, such as a yield strength greater than 275 MPa,<sup>1,2</sup> rather than to obtain a specific chemical composition. The chemical composition of a specific HSLA steel may vary for different product thicknesses to meet mechanical property requirements.

The factors that led to the initial development of micro-alloyed steels, at least up to the late 1960s, were:<sup>3</sup>

- materials cost savings could be obtained directly by the application of micro-alloyed steels;
- in-service benefits could be obtained in the development of lighter goods;
- the need for a higher strength line-pipe that was easily weldable provided an expanding market for higher-yield-strength steels;
- the extensive use of welding as the principal fabrication method meant that conventional ways of increasing the strength would result in more expensive and much less practicable welding procedures, whilst the new micro-alloyed steels with their generally lower carbon and alloy levels could often be welded using existing procedures;

- the strength increase could be obtained relatively cheaply, as both niobium and vanadium, are not readily oxidised by steel melt processing.

The development of micro-alloyed steels was not restricted to plates; development work was already reported for hot-rolled strip and for bar material for reinforcement. Another significant development in the period between 1963 and 1967 concerned hot-rolling practices, when a process now known as "controlled rolling" was developed.<sup>3,4</sup> This enabled fine-grained microstructures to be obtained in the "as-rolled" condition, with benefits for both strength and toughness. By allowing the hot-rolling process to occur at lower temperatures, a finer austenite grain microstructure was produced, which resulted in finer ferrite grain sizes after transformation during cooling.<sup>5</sup>

The above described developments in micro-alloyed steels are summarised in **Figure 1**, where the various developments are shown on a time base and compared with external influences (modern welding methods, oil crises, development of environmental pressures).<sup>3</sup>

Micro-alloyed steels are nowadays divided into six categories:<sup>2,4-5</sup>

- Weathering steels, which contain small amounts of alloying elements such as copper and phosphorus for an improvement of the atmospheric corrosion resistance and solid-solution strengthening.

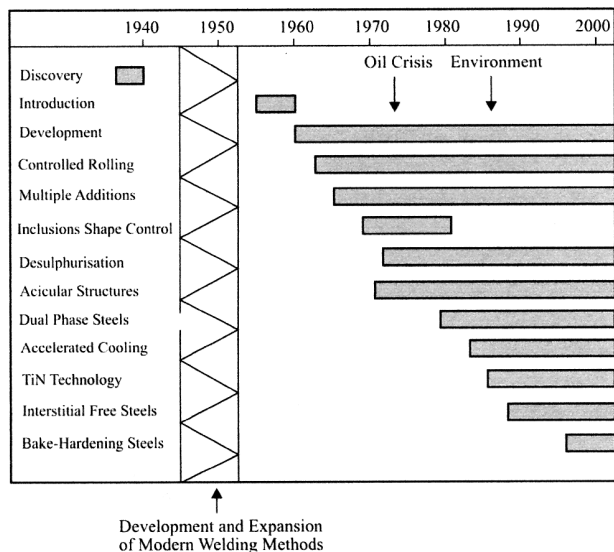


Figure 1: Development of HSLA steels from 1940 to 2000<sup>3</sup>

Slika 1: Razvoj HSLA-jekel od leta 1940 do 2000<sup>3</sup>

- b) Micro-alloyed ferrite-pearlite steels with very small (generally less than 0.1 %) additions of strong carbide- or carbonitride-forming elements, niobium, vanadium, and/or titanium, for precipitation strengthening, grain refinement, and possibly, transformation temperature control.
- c) As-rolled pearlitic steels, which may include carbon-manganese steels with small additions of other alloying elements to enhance strength, toughness, formability and weldability.
- d) Acicular ferrite (low-carbon bainite) steels are low-carbon (less than 0.05 % C) steels with an excellent combination of high yield strengths (as high as 690 MPa), weldability, formability and good toughness.
- e) Dual-phase steels with a microstructure of martensite inserts dispersed in ferritic matrix and with a good combination of ductility and high tensile strength.
- f) Inclusion-shape-controlled steels with improved ductility and through-thickness toughness due to small additions of calcium, zirconium, titanium or rare-earth elements that change the shape of sulphide inclusions from elongated stringers to small, dispersed, almost spherical globules.

The wide applications of HSLA steels include oil and gas pipelines, heavy-duty highway and off-road vehicles, construction and farm machinery, industrial equipment, storage tanks, bridges, offshore structures, power-transmission towers, light poles as well as building beams and panels.<sup>6-8</sup>

The choice of a specific high-strength steel depends on a number of application requirements, including thickness reduction, corrosion resistance, formability and weldability. For many applications, the most important factor in the selection is the favourable strength-to-weight ratio<sup>5</sup> of HSLA steels compared with conven-

tional low-carbon steels. This characteristic of HSLA steels has led to their increased use in automobile components.

## 2 STRENGTHENING MECHANISMS

The micro-alloyed steels used nowadays are obtained by means of a suitable combination of chemical composition and thermo-mechanical treatment parameters, with the aim to achieve the proper balance between strength, toughness, ductility and formability. These properties depend upon microstructural features, while weldability is generally accepted as being composition dependent.

The yield strength of steel can be increased by one or more of several strengthening mechanisms. These include:<sup>2,3,5,9,10</sup>

- a) Dislocation strengthening: the resistance to dislocation movement due to the obstacles presented to other dislocations. The limitations of this mechanism are due to the saturation of the structure with dislocations.
- b) Grain-boundary strengthening: grain-boundary hindering of dislocation movement. Grains can be refined to a very small size, and a very high strength may be achieved. Below a critical grain size the toughness may be lowered.
- c) Solid-solution strengthening: the resistance to dislocation movement due to the presence of interstitial or substitutional solute atoms in a crystal lattice. The limitation of this mechanism is imposed by the solubility limit in each alloying system.
- d) Precipitation strengthening: the resistance to dislocation movement due to the effect of second-phase particles. Second-phase particles may be dispersoids (stable particles mechanically added and sintered) or precipitates (particles formed from a supersaturated solid solution) which is more present in practice. The limitation of this mechanism is governed by the influence of the size and shape on toughness, not on the strengthening.
- e) Texture strengthening: the resistance to dislocation movement due to the presence of a texture-preferred orientation in the structure. This mechanism does not seem to be as potent as other strengthening mechanisms, while the development of texture is difficult in steels with a dispersed second phase.
- f) Phase-transformation strengthening: the resistance to dislocation movement due to the presence of newly formed phases introduced by a phase transformation that starts simultaneously with a deformation. This mechanism gives new opportunities and it may be considered as the main research challenge in the future.

From all six mechanisms, the dominant mechanism is grain-boundary strengthening, because the influence on the grain size can be accomplished by a modification of

the chemical composition, production parameters and/or routes.

## 2.1 Grain refinement

Grain refinement is an effect of micro-alloying on steels because it simultaneously produces increased strength and toughness, without affecting weldability and ductility<sup>1</sup> (Figure 2). The quantitative relationship between yield strength and grain size in metals is known as the Hall-Petch equation:<sup>11,12</sup>

$$\sigma_0 = \sigma_t + k_0 \cdot d^{-1/2} \quad (1)$$

where:

$\sigma_0$  – yield strength

$\sigma_t$  – yield strength of a single crystal

$k$  – Hall-Petch factor (a constant, representing the blocking effect of grain boundaries on the movement of dislocations at the initial stage of the plastic deformation)

$d$  – grain size

Grain refinement can be achieved by three types of precipitation:<sup>1</sup>

- small particles that do not dissolve, and therefore pin down austenite grain boundaries, during reheating prior to hot working (usually TiN, sometimes Nb(C,N));
- particles that dissolve during reheating, but precipitate in austenite during hot rolling and prevent recrystallisation and/or grain growth (usually Nb(C,N), sometimes VN);
- particles that precipitate after rolling, during the transformation of austenite to ferrite (usually V(C,N), sometimes NbC or TiC).

## 2.2 Precipitation strengthening

The precipitation strengthening is produced by the particles' precipitation in ferrite. These particles hinder dislocation movement under loading and increase the

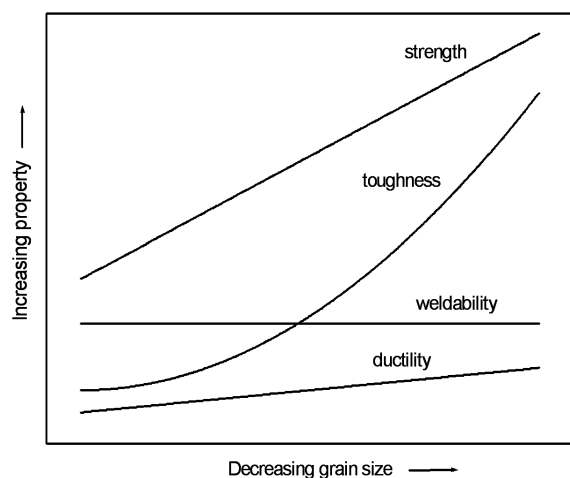


Figure 2: Effect of ferrite grain size on properties<sup>1</sup>

Slika 2: Vpliv velikosti feritnih zrn na mehanske lastnosti<sup>1</sup>

yield strength and tensile strength. The precipitates most often used to strengthen ferrite are V(C,N), although NbC and TiC particles can be used in low-carbon, low-nitrogen steels. TiN is a less soluble micro-alloying precipitate. TiN particles form at very high temperatures and, if finely distributed, prevent austenite grain growth at normal reheating temperatures. The content of the micro-alloying elements carbon and nitrogen as well as the thermomechanical processing determine whether TiC, NbC, VN or other complex carbonitrides precipitate in austenite or ferrite. The most soluble micro-alloying precipitate is VC, which normally precipitates only in ferrite.<sup>1,3,10</sup>

The relationship between the grain size ( $R$ ), the volume fraction ( $f$ ) and size of precipitates ( $r$ ) was first proposed by Zener in his well-known equation:<sup>10</sup>

$$R = \frac{4r}{3f} \quad (2)$$

where:

$R$  = radius of the matrix grains

$r$  = radius of the precipitates (pinning particles)

$f$  = volume fraction of the precipitates (pinning particles).

The Zener equation includes the major features of grain-growth inhibition by second-phase particles. A finer grain size can be stabilised by an increased volume fraction of particles for a given particle size and finer particles are capable of stabilising a finer grain size for a given volume fraction of particles.<sup>3,10</sup>

One further important phenomenon that can affect the particle size is known as Ostwald ripening.<sup>2,3,10</sup> It relates to the increase in particle size that occurs at a constant volume fraction of precipitate, and can result in a significant loss of the particles' performance. A definition of Ostwald ripening can be given as the selective growth of some second-phase particles, usually the larger particles, at the expense of other particles of the same phase, usually the smaller particles, the latter decreasing in size until they disappear completely. The equation, presented by Lifshitz, Slyozov and Wagner, describes the kinetics of particle coarsening with respect to both temperature and time:<sup>10</sup>

$$r_t^3 - r_0^3 = \frac{8\sigma D[M]V}{9RT} \cdot t \quad (3)$$

where:

$r_t$  = particle radius at time  $t$

$r_0$  = particle radius at time 0

$\sigma$  = surface energy of the particle-matrix interface

$D$  = diffusivity of relevant atom species

$[M]$  = concentration (solubility) of relevant atom species in the matrix

$V$  = particle molar volume

$R$  = gas constant

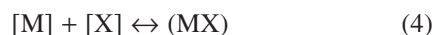
$T$  = temperature

A most important feature of this equation is the concentration of relevant atom species dissolved in the matrix [M]. The growth of the pinning particles will be minimised by a small [M] dissolved in the matrix. Because of its thermodynamic stability and low solubility at high temperature, TiN resists particle growth and is thus a most effective grain-boundary-pinning particle.

The concept of Ostwald ripening was originally developed for the coarsening of solid particles in a liquid matrix, but the mathematical solutions have been applied successfully to second-phase particles in a solid matrix.

### 3 SOLUBILITY OF CARBIDES AND NITRIDES

With the aim to understand the influence of micro-alloying elements on the mechanical properties and the hot-working process it is necessary to know the processes and reactions in steel involving these elements and their compounds with nitrogen and carbon which form precipitates. The reaction of a micro-alloying element [M] with an interstitial [X], both dissolved in the austenite, gives a compound [MX] at a temperature  $T$ :<sup>3</sup>



$$k_s = [M][X] \quad (5)$$

The definition of the solubility product is:

$$\lg k_s = A - B/T \quad (6)$$

where  $A$  and  $B$  are constants for a given system and  $T$  is the temperature in K.

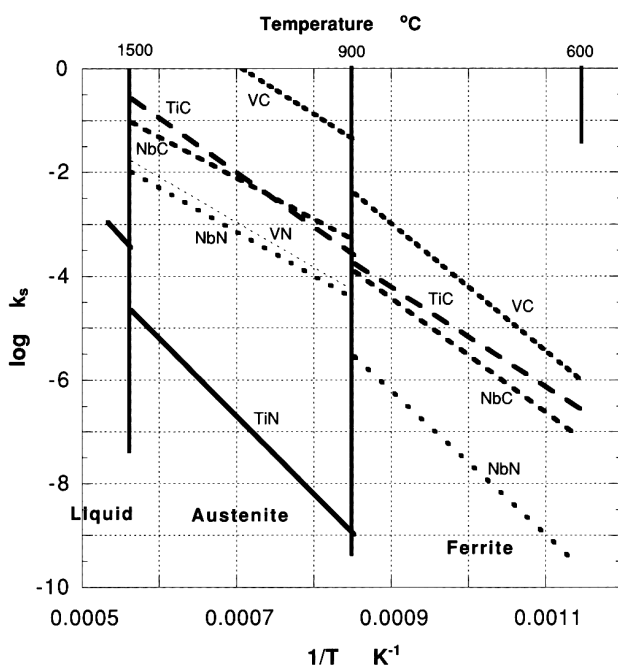


**Figure 3:** Comparison of the solubility products of carbides and nitrides<sup>3</sup>

**Slika 3:** Primerjava topnostnih produktov za karbide in nitride<sup>3</sup>

The solubility products of the micro-alloy carbides and nitrides are compared in **Figure 3**. The general conclusions drawn from this data are:<sup>3</sup>

- In austenite, nitrides are more stable than carbides. Large differences are between vanadium carbide and vanadium nitride and between titanium carbide and titanium nitride, whilst the difference between niobium carbide and niobium nitride is much less.
- Many of the micro-alloy carbides and nitrides have similar levels of solubility in austenite, with two notable exceptions. Titanium nitride is markedly more stable than other carbides and nitrides. On the other hand, vanadium carbide is far more soluble than other carbides and nitrides.
- The solubilities of niobium carbide and niobium nitride in ferrite suggest that the solubilities of these compounds are about an order of magnitude less in ferrite than the corresponding solubilities in austenite at the same temperature.

The effects of a steel's chemical composition and thermomechanical processing on the solubility and precipitation reactions of these precipitates are essential for obtaining the properties that are the basis for the successful application of micro-alloyed steels. Otherwise, the benefit of micro-alloying could be lost, as shown in following examples.

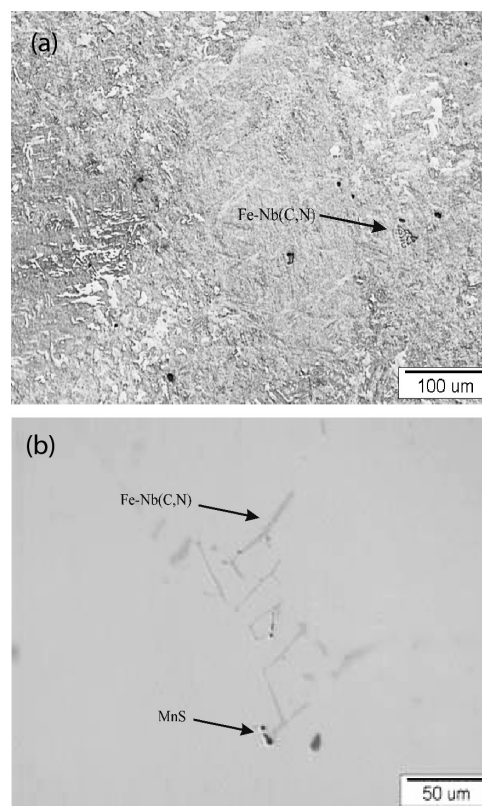


**Figure 4:** Form of eutectic niobium carbonitride particle in cast slab; a) etched with nital; b) non-etched surface

**Slika 4:** Oblika eutektičnega niobijevega karbonitrida v litem slabu; a) jedkano z nitalom; b) nejedkana površina

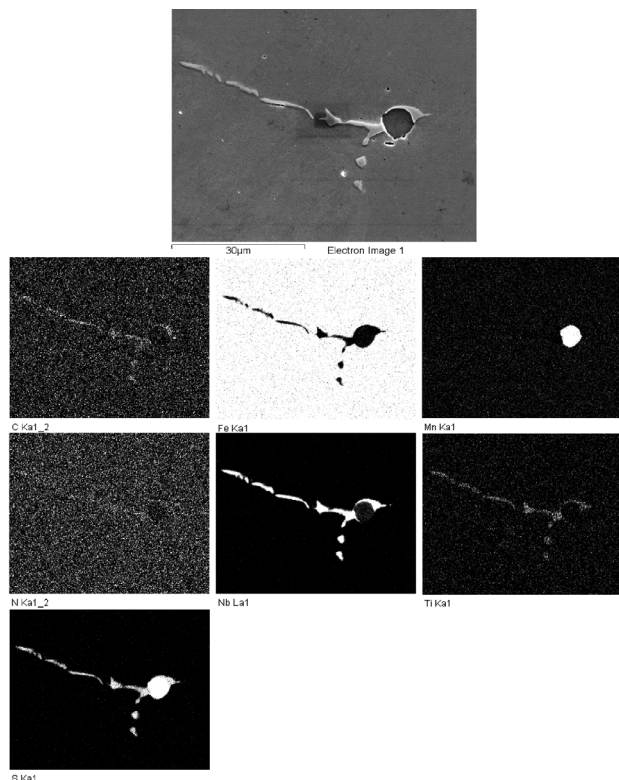


**Figure 5:** SE image and X-ray maps of niobium carbonitride precipitates bound to MnS

**Slika 5:** SEM-posnetek niza karbonitridnih vključkov, vezanega na MnS, in prikaz površinske porazdelitve elementov

The examinations of the plates of micro-alloying steel (Micral S690QL) showed lower ductility than was prescribed. To investigate the reason for such low ductility, samples for optical and scanning electron microscopy were taken from a cast slab. **Figure 4** shows optical micrographs with niobium carbonitrides. **Figure 5** shows a SE image and mapping micrographs of niobium-containing particles (Nb,Ti)(C,N)<sup>13-17</sup> bound on a small manganese sulphide inclusion. The analysis of the chemical composition of the carbonitride particles has turned out to be very complicated. The problem arises from the proper determination of the concentration of nitrogen and titanium, also reported by other authors.<sup>18-20</sup> The nitrogen concentration is, according to literature sources,<sup>21-23</sup> responsible for the thermodynamic stability of carbonitride. A precise measurement of the nitrogen concentration would enable a determination of the limit nitrogen concentration in carbonitride, which considerably decreases the ductility of the steel.

The solubility product for niobium carbonitride is given by the equation:<sup>3</sup>

$$\lg k_s = -6770/T + 2.26 \quad (7)$$

There are variations in the stoichiometry, some authors consider niobium carbonitride given by the formula NbC<sub>0.8</sub>, others as NbC or Nb(C,N).<sup>3</sup>

The next example of an inadequate precipitation of micro-alloying elements is shown in **Figure 6**. In this

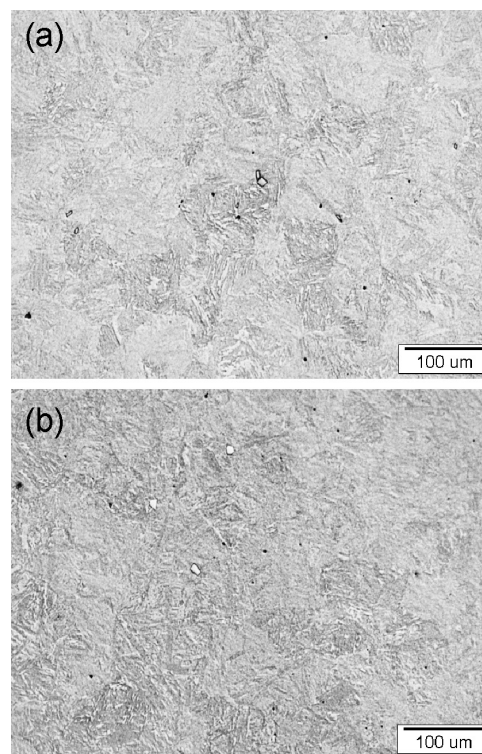


**Figure 6:** Steel, micro-alloyed with a) titanium and b) zirconium with large precipitates of these elements<sup>13</sup>

**Slika 6:** Jeklo, mikrolegirano s a) titanom in b) cirkonijem z velikimi precipitati teh elementov<sup>13</sup>

case the micro-alloying elements titanium and zirconium have been precipitated as large particles (up to 10 μm), which are typically coloured after etching. The improved mechanical properties can be obtained only by finely distributed Nb, Ti or Zr precipitates on a nanometre scale size; and therefore it is not surprising that in this case an improvement of mechanical properties was not obtained.

#### 4 STEEL PROCESSING

The desirable properties of HSLA steels are achieved basically through ferrite grain refinement and by the precipitation of micro-alloy carbonitride particles. For economic production it is necessary to maximize these effects with various types of thermomechanically controlled processing (TMCP). The prevailing share of steel products is manufactured by rolling. For micro-alloyed steels two main types of rolling processes are used:<sup>3, 4, 24</sup>

- a) Thermo-mechanical rolling or recrystallisation controlled rolling (RCR) is used for steels with martensitic and bainitic structures. This rolling consists of rolling in the MX phases' precipitation temperature range, with pauses between the consecutive rolling passes, enabling a complete austenite recrystallisation as well as the isothermal holding of a properly selected temperature of the end of the hot working by time  $t_{0.5}$  – needed for the development of 50 % fraction of recrystallised austenite and direct cooling with

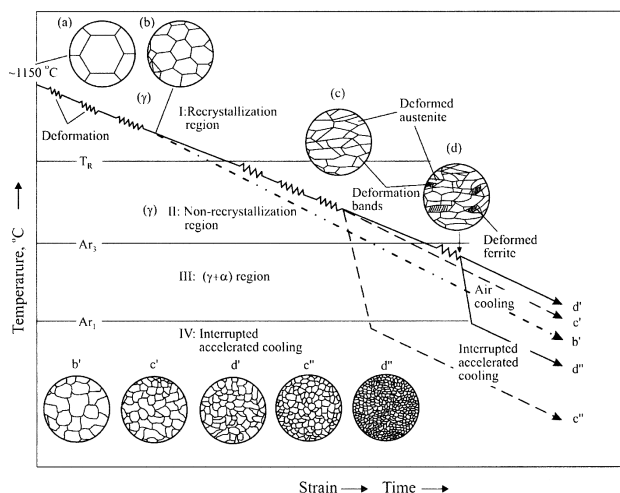


**Figure 7:** Schematic diagram of the influence of accelerated cooling on the microstructure of low-carbon micro-alloyed steel products during controlled rolling<sup>4</sup>

**Slika 7:** Shematski prikaz vpliva pospešenega ohlajanja na mikrostrukturo maloogljiknih malolegiranih jekel med kontroliranim valjanjem<sup>4</sup>

the appropriate cooling rate. Isothermal holding of products at the temperature of the end of rolling for the time  $t_{0.5}$  is necessary, as the high dislocation density in the plastically deformed austenite increases the critical cooling rate. Products manufactured with this method are subjected only to the appropriate temperature tempering or ageing.

- b) Conventional controlled rolling (CCR) is normally used for steels with a ferrite and ferrite-pearlite microstructure. This rolling consists of roughing the feedstock in the upper part of the plastic working temperature range and of finish rolling in the lower part of the temperature range for this process, corresponding to the precipitation of the MX phases, limiting the grain growth of recrystallised austenite in passes between the consecutive passes. Finish rolling usually ends at a temperature slightly lower than the austenite recrystallisation temperature  $T_R$  and a little bit higher than  $A_{r3}$  or  $A_{r1}$  for the steel with subsequent air cooling of the products (**Figure 7**). The presence of slip bands and deformation bands in non-recrystallised austenite causes an increase of the population of locations convenient for nucleation in the  $\gamma \rightarrow \alpha$  transformation and leads to the development of a more fine-grained structure of the steel products.
- c) Two-phase rolling technology is a modification of the CCR technology. The main difference is that finish rolling is performed partially in the two-phase region. After cooling, austenite grains will transform into small ferrite grains, while deformed ferrite grains will recrystallise and become finer. This technology is normally used for the rolling of thin strips, due to their high resistance to deformation.

- d) Dynamic recrystallisation controlled rolling (DRCR) is a modification of the CCR technology. The overall strain in finish rolling is higher than in CCR and the accumulation of deformation from pass to pass should lead to exceeding the critical strain for dynamic recrystallisation. In this case the effect of grain refinement is the strongest. This technology is not yet commercialized, due to the lack of reliable data.
- e) Conventional controlled rolling + accelerated cooling (CCR+AC) with accelerated cooling after the CCR or two-phase region rolling up to  $A_{r1}$  temperature that provides a certain amount of ferrite transformation, enriching the rest of the matrix with carbon and lowers the austenite transformation temperature. With further cooling the austenite transforms to bainite and/or martensite. This technology provides a two-phase microstructure consisting of very fine ferrite grains and bainite and/or martensite.

## 5 MECHANICAL PROPERTIES

There are three major property requirements for HSLA steels: a high yield strength, a low impact transition temperature and good weldability.<sup>2</sup> The high yield strength and low impact transition temperature are achieved through ferrite grain refinement, where nitrogen is partially useful. However, nitrogen dissolved in ferrite also influences the strength and toughness. This solid solution strengthening is very small, especially as the solid solubility of nitrogen in ferrite is very limited, but the embrittlement propensity may be increased, also. Thus nitrogen dissolved in ferrite must be minimised, which is done in micro-alloyed steels with additions of Al, V, Nb or Ti, all of which form stable nitrides. These nitrides have the ability to refine austenite grains and thereby ferrite grains, also.<sup>2</sup>

## 6 CONCLUSIONS

The paper gives a short review on the development and basic characteristics of micro-alloyed steels. The general conclusions are that in modern, control-rolled, micro-alloyed steels at least three strengthening mechanisms contribute to the final achieved strength. The relative contribution of each is determined by the steel's composition as well as by the steel's thermomechanical treatment. The effect of the finishing temperature for the rolling is important in determining the grain size and, therefore, the strength level reached for a particular steel.

## 7 REFERENCES

- <sup>1</sup> J. R. Paules: Practical considerations in microalloying with vanadium, niobium, or titanium, Proc. of the Inter. Symp. on Microalloyed Vanadium Steels, Cracow, (1990), 19–32
- <sup>2</sup> H. K. D. H. Bhadeshia, R. Honeycomb, Steels Microstructure and Properties, 3<sup>rd</sup> ed., Elsevier, 2006

- <sup>3</sup> T. Gladman: The physical metallurgy of microalloyed steels, 1<sup>st</sup> ed., The University Press, Cambridge 1997
- <sup>4</sup> J. Adamczyk, Journal of Achievements in Materials and Manufacturing Engineering, 14 (2006), 9–20
- <sup>5</sup> <http://www.keymetals.com>
- <sup>6</sup> Z. K. Liu, Scripta Mater., 50 (2004), 601–606
- <sup>7</sup> H. Najafi, J. Rassizadehghani, A. Asgari, Mater. Sci. Eng. A, 486, (2008), 1–7
- <sup>8</sup> D. L. Albright, S. Bechet, K. Rohrig, Proceedings of International Conference on Technology and applications of HSLA steels, ASM, Philadelphia, PA, USA, (1984), 1137–1153
- <sup>9</sup> F. B. Pickering: Physical Metallurgy and the Design of Steels, 1<sup>st</sup> ed., Applied Science Publishers LTD, London 1978
- <sup>10</sup> F. B. Pickering: Titanium nitride technology, Proc. of the Inter. Symp. on Microalloyed Vanadium Steels, Cracow, (1990), 79–104
- <sup>11</sup> E. O. Hall: Proc. Roy. Soc., 64B, (1951), 747
- <sup>12</sup> N. J. Petch: Journ. Iron Steel Inst., 174, (1953), 28
- <sup>13</sup> D. A. Skobir, M. Godec, A. Nagode, M. Jenko, Surface and Interface Analysis, 42 (2010), 717–721
- <sup>14</sup> J. Bernetic, B. Bradaskja, G. Kosec, B. Kosec, E. Bricelj, Materiali in Tehnologije 42 (2008), 291–294
- <sup>15</sup> F. Vodopivec, Kovine zlitine tehnologije, 26 (1992), 319–328
- <sup>16</sup> F. Vodopivec, D. Kmetec, F. Tehovnik, J. Vojvodič - Tuma, Materiali in Tehnologije, 41 (2007), 111–117
- <sup>17</sup> F. Vodopivec, M. Gabrovšek, B. Ralić, Metal science, 9 (1975), 324–326
- <sup>18</sup> P. Panjan, B. Navinsek, A. Zabkar, D. Mandrino, M. Godec, M. Kozelj, Z. Krivokapic, A. Zalar, Thin Solid Films, 181 (1989), 35–41
- <sup>19</sup> P. Panjan, A. Zabkar, B. Navinsek, V. Krasevec, V. Marinkovic, D. Mandrino, M. Godec, M. Macek, A. Zalar, Vacuum, 41 (1990), 1272–1274
- <sup>20</sup> P. Panjan, B. Navinsek, A. Zabkar, V. Marinkovic, D. Mandrino, J. Fiser, Thin Solid Films, 228 (1993), 233–237
- <sup>21</sup> R. Staško, H. Adrian, A. Adrian, Materials Characterization, 56 (2006), 340–347
- <sup>22</sup> J. Fernández, S. Illescas, J. M. Guilemany, Materials Letters, 61 (2007), 2389–2392
- <sup>23</sup> X. Zhuo, X. Wang, W. Wang, H. G. Lee, Journal of University of Science and Technology Beijing, 14 (2007), 112–117
- <sup>24</sup> S. Zajac, T. Siwecki, B. Hutchinson and M. Attlegard: Recrystallization controlled rolling and accelerated cooling for high strength and toughness in V-Ti-N steels, Proc. of the Inter. Symp. on Microalloyed Vanadium Steels, Cracow, (1990), 149–170



## TEM INVESTIGATION OF METALLIC MATERIALS – AN ADVANCED TECHNIQUE IN MATERIALS SCIENCE AND METALLURGY

### PREISKAVE KOVINSKIH MATERIALOV S PRESEVNO ELEKTRONSKO MIKROSKOPIJO - MODERNA TEHNIKA V ZNANOSTI O MATERIALIH IN METALURGIJI

**Darja Jenko**

Institute of Metals and Technology, Lepi pot 11, p. p. 431, SI-1000 Ljubljana, Slovenia  
darja.jenko@imt.si

*Prejem rokopisa – received: 2011-04-21; sprejem za objavo – accepted for publication: 2011-07-07*

The investigation of different metallic materials using high-resolution transmission electron microscopy (HRTEM) is presented. After thinning using argon ion-slicing thin foil specimens were prepared and further analyzed by various TEM analysing techniques at 200 kV, that make a powerful combination to resolve a large number of problems encountered in materials science and metallurgy. Some case studies of such problems are presented: influence of foaming agents in manufacturing processes of aluminium metal foams, removal of remaining oxides from the surface of duplex stainless steel (DSS), effect of low temperature ageing on properties of DSS, effect of heat treatment on the microstructure and properties of precipitate containing aluminium alloys.

Key words: transmission electron microscopy, Ar ion slicing, silicon, duplex stainless steel, aluminium alloy

V prispevku so opisane preiskave različnih kovinskih materialov z visokoločljivostno presevno elektronsko mikroskopijo. Vzorce tankih folij smo po tanjšanju z rezanjem z ioni argona nadalje preiskovali pri 200 kV z različnimi analznimi tehnikami presevne elektronske mikroskopije, ki so močna kombinacija pri reševanju velikega števila problemov, s katerimi se srečujemo v znanosti o materialih in metalurgiji. Predstavljenih je nekaj primerov takšnih problemov: vpliv penilnih sredstev v proizvodnji kovinskih aluminijevih pen, odstranitev preostalih oksidov s površine dupleksnega nerjavnega jekla (DSS), vpliv nizkotemperaturnega staranja na lastnosti DSS, vpliv toplotne obdelave na mikrostrukturo in lastnosti aluminijevih zlitin z vključki.

Gljučne besede: presevna elektronska mikroskopija, rezanje z ioni Ar, silicij, dupleksno nerjavno jeklo, aluminijeva zlitina

## 1 INTRODUCTION

Today electron microscopy, more specifically transmission electron microscopy (TEM) is indispensable for the characterization of various materials mainly on nanometer (atomic) scale. Nanotechnology is the understanding and control of matter at dimensions between approximately 1 nm and 100 nm, where unique phenomena enable novel applications.<sup>1</sup> The encompassing nanoscale science, engineering, and technology, nanotechnology involves imaging, measuring, modeling, and manipulating matter at this size scale. 'Imaging, measuring, modeling, and manipulating matter' can be accomplished using TEM. By means of TEM measurements information is obtained on crystal lattice, cell parameters, different phases, grain size, morphology, density of defects (dislocations, stacking faults, twins) etc.

The word microscope is derived from Greek mikros (small) and skopein (to look, to see). From the dawn of science there has been an interest in being able to look ever smaller details of the world around us. Materials scientists wanted to see inhomogeneities and imperfections in ceramics<sup>2</sup>, glasses, polymers, semiconductors, crystals (single, liquid)<sup>3</sup>, metals, alloys, steels<sup>4,5</sup>, com-

posite mixtures of these materials, and different powder mixtures<sup>6</sup>, with sporadic observations of wood, textiles, and concrete. Biologist wanted to examine the structure of cells, bacteria, viruses, and colloidal particles. In geology, the detailed study of rocks, minerals, and fossils on a microscopic scale provides insight into the origins of our planet and its valuable mineral resources. Because of today's better analysing techniques, including TEM, it is possible to investigate all these materials from different fields of science in more exact and detailed manner using TEM or using other analytical techniques in combination with TEM. In the research program of the institute several research works for instance on surface reactions and processes<sup>7-22</sup>, creep resistant steels properties and microstructure<sup>23</sup>, effect of low temperature ageing on properties of Fe-NiCrMo alloys<sup>24,25</sup> were included in a number of reports prepared and of work published would certain be of better quality if TEM was used also and the examination or conclusion strengthened by TEM analyses.

Given sufficient light, the unaided healthy human eye can distinguish two points 0.1–0.2 mm apart.<sup>26</sup> If the points are closer together, they will appear as a single point. This distance is called the resolving power or

resolution of the eye. A lense or an assembly of lenses (a microscope) can be used to magnify this distance and enable the eye to see points even closer together than 0.1 mm.

Most microscopes can be classified as one of three basic types: 1. optical or light, which use visible light and transparent lenses to see objects as small as about 1  $\mu\text{m}$ , 2. charged particles (electron and ion), which use a beam of charged particles instead of light and electromagnetic or electrostatic lenses to see the particles, or 3. scanning probe, which use a physical probe (a very small, very sharp needle) that scans over the specimen in contact or near-contact with the surface.<sup>26,27</sup> Both latter types of microscopes, charged particles and scanning probe are capable of atomic scale resolution.

In the 1920s, it was discovered that accelerated electrons behave much like light in vacuum.<sup>26</sup> They travel in straight lines and have wave-like properties, with a wavelength that is about 100 000-times shorter than that of visible light. E. Ruska at the Technical College in Berlin, under the tutelage of M. Knoll, combined these characteristics and built the first transmission electron microscope (TEM) in the early 1930s. This first TEM used two magnetic lenses, and three years later he added a third lens and demonstrated a resolution of 100 nm, twice as good as that of the light microscope (a modern visible-light microscope has a magnification of about 1 000-times and enables the eye to resolve objects separated by 200 nm).

L. de Broglie's famous equation<sup>26</sup> shows that the wavelength  $\lambda$  in nm of electrons is related to their energy  $E/eV$  and, if we ignore relativistic effects, we can show approximately that (ignoring the inconsistency in units)

$$\lambda = 1.22/(E^{1/2}) \quad (1)$$

We can calculate from equation (1) that by 100 keV electron,  $\lambda$  is  $\approx 4$  pm (0.004 nm), which is much smaller than the diameter of an atom.

The resolving power of a TEM is determined by a combination of beam voltage, aperture size and lense aberrations.<sup>26</sup> Today, TEMs have reached resolutions better than 0.05 nm, more than  $4 \cdot 10^3$ -times better than a typical visible-light microscope and  $4 \cdot 10^6$ -times better than the unaided eye.

Despite the advantages of the TEM there are some drawbacks.<sup>26</sup> First of all, the price to pay for high-resolution imaging technique is that at one time we only look at small part of our specimen. So we have an instrument that is not a good sampling tool. Another problem is that the TEM presents us with 2D images of 3D specimens, viewed in transmission. So we have to be aware of the artifacts which abound in TEM images and be cautious in their interpretation. Also a detrimental effect of ionization is that it can damage our specimen. And there is always a possible danger of exposing oneself to ionizing radiation although modern TEMs are remarkably well engineered and designed with safety as a primary concern. A major limitation of the TEM is we need thin

(electron transparent) specimens. Generally, specimens  $<100$  nm should be used wherever possible. For high-resolution (HR) TEM imaging or electron spectrometry, specimen thicknesses  $<50$  nm (even  $<10$  nm) are essential. This requirement is a function of the electron energy and the average atomic number ( $Z$ ) of our specimen. The thinning processes that we use do affect the specimens, changing both their structure and chemistry. So we need to be aware of the drawbacks of specimen preparation and learn to recognize the artifacts introduced by standard preparation methods.<sup>26,28,29</sup>

In the Institute of Metals and Technology (IMT) in Ljubljana, Slovenia, the JEOL JEM-2100 TEM (**Figure 1**) started to operate in December 2008 and it was finally installed in March 2009. It is a high-resolution (HR) and analytical electron microscope (AEM) that not only offers TEM images and diffraction patterns, but also incorporates a computer control system which integrates a scanning transmission electron microscope (STEM) image observation device with bright-field (BF) and dark-field (DF) detectors, as well as an energy dispersive X-ray spectrometer (EDXS) JED-2300T. The microscope operates at magnification ranges from 50-times to  $1.5 \cdot 10^6$ -times in TEM mode. High stability of the high



**Figure 1:** JEOL JEM-2100 high-resolution and an analytical electron microscope equipped with STEM unit (bright- and dark-field detectors) and EDXS detector

**Slika 1:** JEOL JEM-2100, visokoločljivostni in analitski elektronski mikroskop, opremljen z enoto STEM (z detektorjem za opazovanje v svetlem in temnem polju) in detektorjem EDXS

voltage and beam current achieves a high resolution of 0.23 nm (point resolution) and 0.14 nm (lattice resolution) at 200 kV (with a high brightness LaB<sub>6</sub> electron source). The accelerating voltage in the range of 80 kV and 200 kV can be changed easily. An optimum accelerated voltage can be selected quickly to observe beam-sensitive materials such as biological materials, polymers or carbon nanotubes. For imaging Gatan ORIUS CCD camera with Gatan Digital Micrograph software is used. It is also possible to heat the specimens up to 1000 °C (maximum to 1100 °C for 48 h).

In this article our experience in use of JEOL JEM-2100 electron microscope is presented as multi-disciplinary instrument providing services for investigations in the microfield and nanofield encompassing wide variety of topics. Performance of the microscope is demonstrated with some results showing its contribution to our studies of nano-materials.

## 2 EXPERIMENTAL WORK

All the specimens of thin foils, except gold particles, used for TEM investigations were prepared using argon ion-slicing with JEOL EM-09100IS Ion Slicer. The Ion Slicer partly thins the specimen. It is possible to prepare cross-section or plan-view thin foil specimens. The instrument irradiates an argon ion beam on the specimen, which is partially masked with a shield belt. The instrument consists of a specimen chamber, which is evacuated with a turbo-molecular pump, ion source tilt mechanism, mask-belt retainer, specimen stage mechanism, camera and other parts. Preparation of thin foils by means of argon ion slicing using Ion Slicer is a novel method that enables a quick preparation of high quality specimens for TEM. It is suitable for the preparation of different speci-

mens for TEM, not only metals, and therefore useful in different fields of science and industry.

Specimens for TEM, thicknesses of around 500 µm, were cut out of a bulk material in rectangular area of 0.5–1.0 mm × 2.8 mm (bulk cross-section preparation). They were thinned to less than 100 µm with JEOL Handy Lap (in many cases with grinding paper SiC 800 only, with the grain size around 22 µm), mounted on an Ion Slicer specimen holder, partially masked with a shield belt (bulk cross-section preparation) and further thinned with an argon ion beam. The parameters of thinning depended on the type of the specimen. The slicing process started at the pressure of 10<sup>-5</sup> Pa or 10<sup>-4</sup> Pa and alternated between the front and the backside of the specimens while they were rotating. The beam was tilted between 1.0° to 2.5°. Accelerating voltage between 4.0 kV and 6 kV, argon gas flow rate between 7.1 and 7.5 (arbitrary units) and side change interval of 30 s or 60 s were chosen. After a large thin area of the specimens up to 300–500 µm × 700 µm was obtained, a small hole was generated in the thinnest region of the specimens. Polishing was used with a tilt angle of 0.5°, at the accelerating voltage of 2 kV and side change interval of 15 s or 40 s for 7 min, 10 min or 15 min. As an example, the total time of slicing was 3 h and 48 min for Si, 6 h and 43 min for AA7075 aluminium alloy and up to 9 h and 40 min for duplex stainless steels (DSS).

Optical microscope image as an example of thin section specimen of silicon after using argon ion-slicing is shown in **Figure 2**. We can see that large thin electron transparent areas are still surrounded by thick specimen parts which enhance the stability of the specimens. After argon ion-slicing the specimens were examined with TEM at 200 kV using conventional TEM (CTEM), HRTEM, electron diffraction, EDXS, and STEM (in this article the results of STEM using BF detector, EDXS mapping, and line profile are presented).

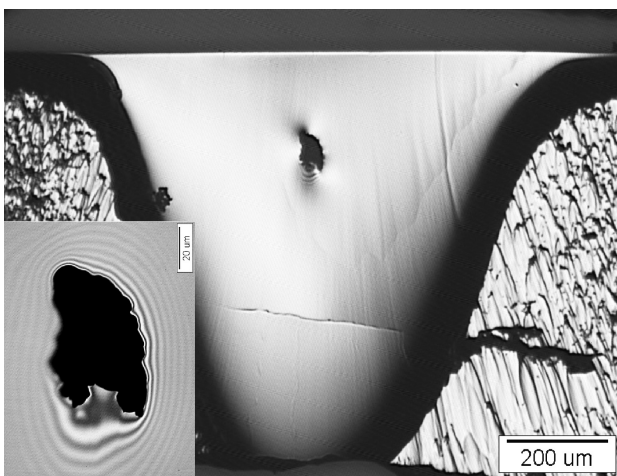


**Figure 2:** Optical microscope image of thin section specimen of silicon for TEM prepared by argon ion-slicing. Thin electron transparent areas are surrounded by thick sample parts

**Slika 2:** Posnetek z optičnim mikroskopom vzorca tanke folije silicija po rezanju z ioni argona. Tanka področja, presevana za elektrone, so obdana z debeljšimi deli vzorca

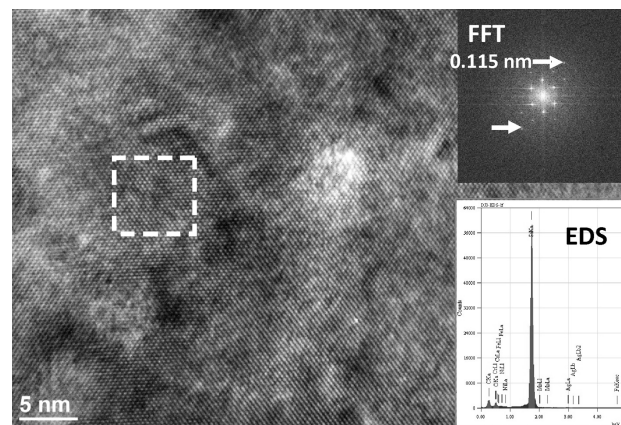


**Figure 3:** High-resolution (HR) TEM image of silicon specimen. The insets are fast Fourier transform (FFT) of the image part marked by the white dash-lined square, and chemical composition analysis (EDXS)

**Slika 3:** Visokoločljivostna slika TEM vzorca silicija. Vstavljena sliki prikazujeta hitro Fourierjevo transformacijo (FFT) dela slike, ki je označena z belim črtkanim kvadratom, in kemijsko sestavo (EDXS)

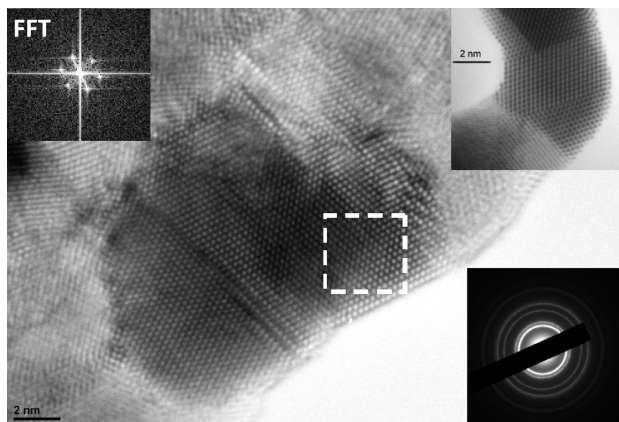


**Figure 4:** High-resolution (HR) TEM image of gold particles. The insets are detailed HRTEM image at magnification of  $1.2 \cdot 10^6$  (1.2 M), fast Fourier transform (FFT) of the image part marked by the white dash-lined square, and diffraction pattern

**Slika 4:** Visokoločljivostna slika TEM zlatih delcev. Vstavljene slike prikazujejo posnetek HRTEM pri povečavi  $1,2 \cdot 10^6$  (1,2 M), hitro Fourierjevo transformacijo (FFT) dela slike, ki je označena z belim črtkanim kvadratom, in uklonski posnetek

### 3 RESULTS AND DISCUSSION

In the frame of this article it is difficult to refer to the great variety of routine investigations performed at IMT. Instead, some case studies of different applications are presented.

#### 3.1 Verification of performance of TEM/HRTEM/EDXS

**Figure 3** shows a HRTEM image of silicon thin foil. The insets are fast Fourier transform (FFT) and chemical composition analysis (EDXS). This was the first specimen prepared to test the performance of JEOL JEM-2100 at IMT. As we could observe in **Figure 2**, the specimen was excellently prepared by thinning with argon ion-slicing. There were many observation areas which were electron transparent, as a matter of fact, the whole foil around the hole was suitable for TEM investigation. Usually, the specimens are covered by a (partly) amorphous surface layer due to preparation damage, which should be kept as thin as possible, as amorphous material decreases the signal-to-noise ratio of the image. In this case, as well in majority of other thin foil specimens, there was no amorphous layer present or it was very thin, a few nm thick.

As follows from the FFT, the lattice fringes with spacing as fine as 0.115 nm could be observed. Such lattice resolution achieved with our instrument appears to be even better than that specified in the official table of the key-features published for JEM-2100 (LaB<sub>6</sub>) microscope (lattice resolution 0.14 nm).

Another example is related to HRTEM imaging of gold particles (**Figure 4**). The insets are detailed

HRTEM image at magnification of  $1.2 \cdot 10^6$  (1.2 M), FFT and diffraction pattern. Although the microscope is not installed on the ground floor but on the second floor, the performance is excellent.

#### 3.2 Verification of performance of CTEM/HRTEM/STEM/EDXS

**Figure 5** and **Figure 6** present, beside CTEM and HRTEM imaging with diffraction pattern of thin foils of aluminium metal foam with closed-cell structure and oxide layers on the surface of duplex stainless steel (DSS), the performance of the microscope in STEM mode which we usually employ with EDXS line scan (**Figure 5**) or elemental mapping (**Figure 6**) to provide information on the chemical composition of very small volumes of material.

##### 3.2.1 Characterization of aluminium metal foam with closed-cell structure

Metal foams are uniform dispersion of a gaseous phase in the solid metal with low densities and novel physical and mechanical properties. Aluminium metal foams with closed-cell structure are manufactured with different foaming agents that are gas releasing substances.<sup>30–32</sup> Closed-cell structure has high impact energy absorption that is very important mechanical property in several industries. An example of TEM investigation of closed-cell aluminium metal foam thin foil specimen is shown in **Figure 5**. The study was

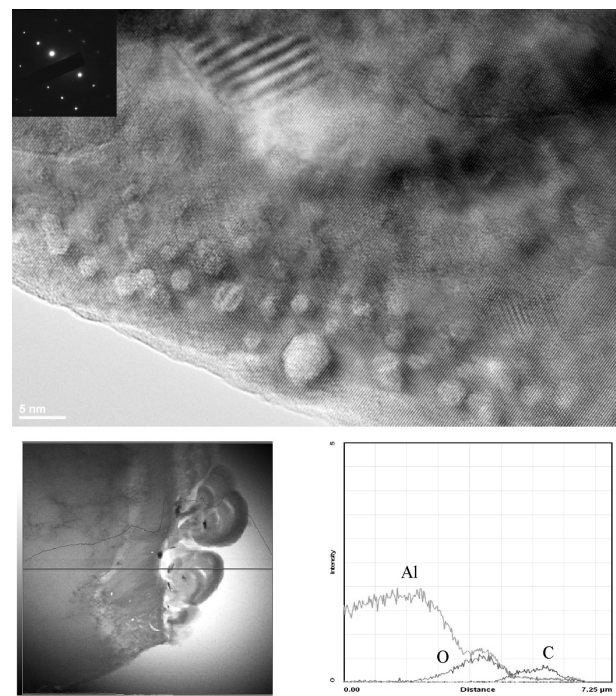


**Figure 5:** High-resolution (HR)TEM image with diffraction pattern of the aluminium metal foam with closed-cell structure. STEM line profile is also shown

**Slika 5:** Posnetek HRTEM z uklonsko sliko vzorca kovinske aluminjske pene z zaprto poroznostjo. Prikazan je tudi linijski profil STEM

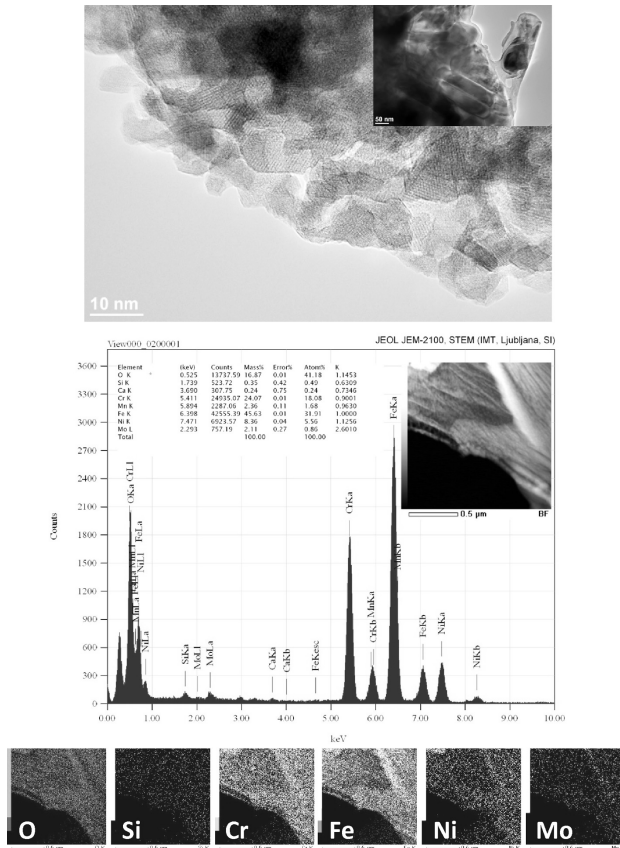


**Figure 6:** Upper image is high-resolution (HR) TEM image of oxide layer on the surface of duplex stainless steel (DSS, 2205 alloy) specimen. The inset is conventional transmission electron microscopy (CTEM) image. Lower image is chemical analysis (STEM-EDXS) with the inset of bright-field (BF) image and EDXS elemental mapping of DSS specimen

**Slika 6:** Zgornja slika prikazuje visokoločljivostno sliko TEM oksidne plasti na površini vzorca dupleksnega nerjavnega jekla (DSS, zlitina 2205). Vstavljena slika je posnetek konvencionalne presevalne elektronske mikroskopije (CTEM). Spodnja slika prikazuje kemijsko analizo z rentgensko spektroskopijo (STEM-EDXS) oksidne plasti vzorca DSS z vstavljeno sliko v svetlem polju in ploskovno analizo EDXS

focused on the analysis of cell walls. Detailed characterization of the microstructure was performed on thin section specimens, as for example HRTEM, electron diffraction and STEM. Electron diffraction method was used to carry out the microstructure–crystallographic analysis of phases, STEM BF imaging and EDXS line profiling to determine elemental distribution. At least two oxide layers with different ratios of aluminium and oxygen appeared at the interface aluminium-pore. The ongoing research will clarify the course of reactions. The results of this study may contribute to the development of cheaper manufacturing processes of aluminium foams, and of a wide range of products with core-based aluminium foams as well.

### 3.2.2 Examination of oxide layers on the surface of duplex stainless steel (DSS, 2205 alloy)

Some of the undesired properties of steel are also degradation and corrosion of stainless steel as result of

not properly cleaned surfaces at the production end. Steel sheet DSS (2205 alloy), thickness of 12 mm, was produced by standard method for thick steel sheets with continuous casting, hot rolling, recrystallization and sandblasting.<sup>33–35</sup> Scale on the surface may aggravate the properties of stainless steels and disturb the processing of material. Unfortunately, the scale on the surface of sheets is not completely removed with sandblasting. The remainder of oxides was studied by TEM (**Figure 6**). Some high-resolution images of oxides were taken in the thinnest places of the sample and some TEM/EDXS analyses were made in those places. Oxides that form on the surface are mainly  $\text{Cr}_x\text{O}_y$  type. The most common oxide is  $\text{Cr}_2\text{O}_3$ . Because of heat treatment of the material, some elements like Mn, Fe, Mo, segregated on the surface of steel where oxides are formed. TEM/EDXS analyses and STEM (BF) with EDXS elemental mapping confirmed formation of Cr-, Fe- and Mn-oxides (the latter not shown in STEM-EDXS elemental mapping). Those oxides were also confirmed with X-ray photoelectron spectroscopy (XPS). Results of high-temperature oxide layers on the surface of DSS enabled us to determine the mechanism and kinetics of formation of these oxide layers, which grow at annealing. Furthermore, they enabled us to understand how to optimally and environmentally friendly remove refractory oxide layers from the surface, which is of great importance for the steel producers.

### 3.2.3 Investigation of isothermal annealing (ageing) of duplex stainless steel (DSS, 258 alloy type)

Thin foils for investigations of DSS (258 alloy type), non-aged and aged (annealed at 300 °C and 350 °C for 10 000 h and 30 000 h), were studied by means of TEM

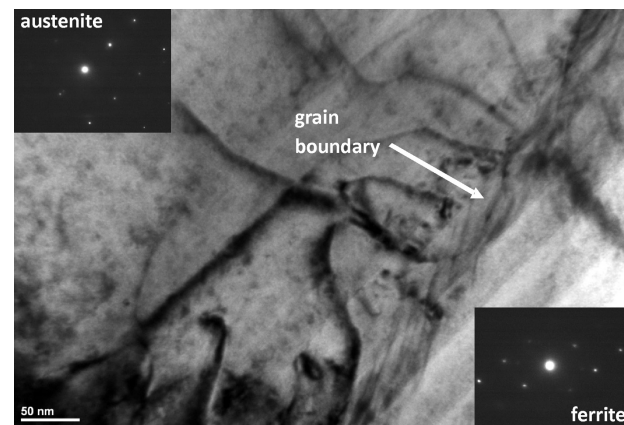


**Figure 7:** TEM image of accumulation of dislocations at the grain boundary between ferrite and austenite in duplex stainless steel (DSS, 258 type) aged specimen (annealed at 350 °C for 30 000 h). The insets are diffraction patterns of ferrite (bcc – body-centered cubic structure) and austenite (fcc – face-centered cubic structure)

**Slika 7:** Posnetek TEM kopičenja dislokacij na meji zrn med feritom in avstenitom v staranem (350 °C, 30 000 h) dupleksnem nerjavnem jeklu (DSS, tip 258). Vstavljene slike prikazujeta uklonska posnetka ferita (bcc – telesno centrirana kubična struktura) in avstenita (fcc – ploskovno centrirana kubična struktura)

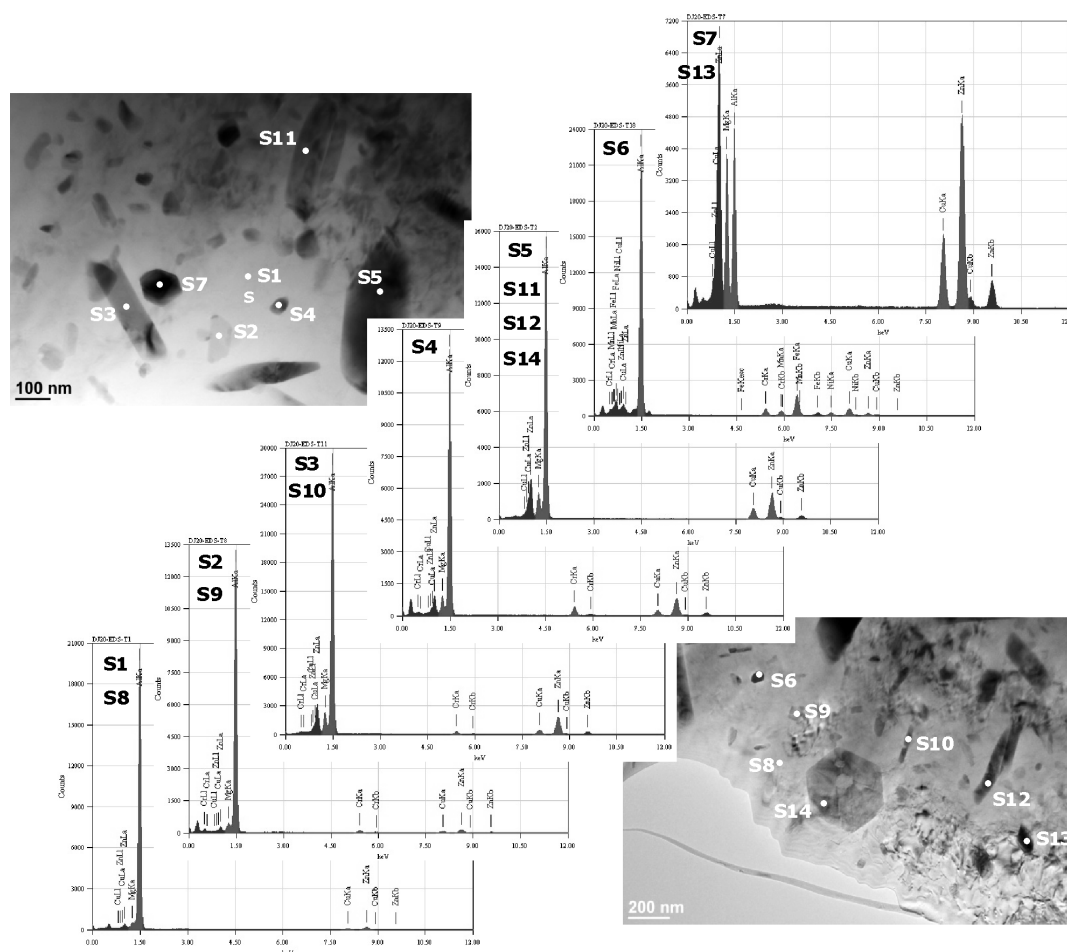


**Figure 8:** TEM images and chemical composition analyses (EDXS) of precipitates in AA7075 aluminium alloy  
**Slika 8:** Posnetka TEM in analize kemijske sestave (EDXS) vključkov v aluminijevi zlitini AA7075

to define ferrite and austenite grains and to observe dislocations (what kind of dislocations they are and where are they located in the specimens). An example of accumulation of dislocations at the grain boundary between ferrite and austenite in DSS aged specimen (annealed at 350 °C for 30 000 h) is shown in **Figure 7**. Spinodal decomposition is expected to occur during thermal ageing of this type of material. The characteristic is formation of nano-cellular microstructure of ferrite domains with regions enriched with Cr and other alphasene alloying elements as well as regions enriched with Co, N and other gammagene alloying elements. Because of difference in local chemical composition, lattice parameters are changed and their accommodation creates elastic stresses that increase the hardness and change mechanical properties (tensile strength increase, while ductility and toughness decrease). The change of mechanical properties may be related also to changes of material's internal structure (stacking faults, morphology and density of dislocations). It has been established that density of dislocations increased after ageing at 300 °C and that they appeared in different configurations with many of them being substantially mobile (numerous

side-trails and traces of dislocations escape to the foil surface). The dislocation configurations changed and many of dislocations became immobilized (or at least slowed down in their movements) after ageing at 350 °C when the transformation of the matrix occurred and achieved a virtually equilibrium state according to the effect of ageing temperature on the change of Charpy notch sharpness. Further investigations (TEM/EDXS) will enable to better understand the characteristics of spinodal decomposition, the influence of ferrite presence in DSS and thus help to increase the life-time of components of thermal power plants including elements of DSS. They will enable to explain the real rearrangement of alloying elements and formation of eventual new phases during spinodal decomposition as well.

### 3.2.4 Investigation of precipitates in AA7075 aluminium alloy

AA7075 aluminium alloy is used for automotive components such as pistons, rocker arms, brake callipers and wheels, as well as application in various fields of sport, electronic and aerospace industry. The properties of this alloy are strongly affected by heat treatments,

which change the microstructure of the alloy to achieve optimum mechanical properties.<sup>36</sup> Within this alloy the large population of intermetallic particles cause a problem of severe localised corrosion due to strong galvanic coupling within the matrix. The intermetallics are formed by the interaction between alloying elements and impurities present in the alloy and may be phases largely based upon the principal alloying elements (Zn and Mg) and can undergo phase transformation and change of morphology during homogenization of alloys, but they are insoluble during solution heat treatment at lower temperature and subsequent ageing.

Specimens of AA7075 aluminium alloy were homogenized at 460 °C for 6 h and air quenched. The TEM was used to assess the shape and size of different precipitates (**Figure 8**) and to determine their chemical composition. Areas of thin foils rich in precipitates were analyzed by means of EDXS. Precipitates differed by morphology, size and contrast. The matrix consisted of bigger rods of about 10<sup>3</sup> nm long and up to 100 nm thick, and of smaller rods also, that differed in composition from the bigger rods. A large number of smaller precipitates of polygonal shapes were present, too. By means of EDXS it was determined that bigger rods consisted of magnesium, aluminium, copper and zinc, while smaller rods contained, apart these elements, also chromium. Polygonal shaped precipitates differed mutually also by contrast. Some contained magnesium, aluminium, copper and zinc but in different ratios as in bigger rods. Other contained aluminium, chromium, copper, zinc, nickel, iron and manganese. The detailed results of this study will be the object of a new article.

#### 4 CONCLUSIONS

The capabilities of high-resolution transmission electron microscope JEOL JEM-2100 with a conventional high brightness LaB<sub>6</sub> electron source allow it effective use in most of routine structure studies of nano-materials. Nanoparticles as small as 5–10 nm can be easily and unambiguously identified by Fourier analysis of high-resolution images combined with elemental X-ray microanalysis or STEM image observation device, coupled with elemental mapping or line profiling techniques. This is demonstrated through several examples of investigations that were carried out at the Institute of Metals and Technology in Ljubljana.

#### Acknowledgments

This work has been supported by the research program "Surface physics and chemistry of metallic materials" P2-0132 and by the "Physics and chemistry of porous aluminium for Al panels capable of highly efficiently energy absorption" project L2-2410 (D), funded by the Slovenian Research Agency. The author wishes to thank M. Jenko, B. Šuštaršič, B. Marini

(CEA), M. Godec, Č. Donik, P. Cvahte (Impol), and I. Paulin for their cooperation and for providing the specimens. Thanks also to M. Pečar, S. Žižek (Scan), R. Ravelle - Chapuis (JEOL Europe SAS) and S. Asahina (JEOL Europe SAS) for valuable advice with TEM operations and thin foil specimen preparations.

#### 5 REFERENCES

- <sup>1</sup> Available from World Wide Web: <http://www.nano.gov/html/facts/whatIsNano.html>
- <sup>2</sup> D. Jenko, A. Benčan, B. Malič, J. Holc, M. Kosec, *Microsc. Microanal.*, 11 (2005) 6, 572–580
- <sup>3</sup> A. Benčan, E. Tchernychova, M. Godec, J. G. Fisher, M. Kosec, *Microsc. Microanal.*, 15 (2009) 5, 435–440
- <sup>4</sup> D. A. Skobir, M. Godec, M. Jenko, B. Markoli, *Surface and Interface Analysis*, 40 (2008) 3/4, 513–517
- <sup>5</sup> D. A. Skobir, F. Vodopivec, S. Spaic, B. Markoli, *Zeitschrift Fur Metallkunde*, 95 (2004) 11, 1020–1024
- <sup>6</sup> M. Remskar, A. Mrzel, M. Virsek, M. Godec, M. Krause, A. Kolitsch, A. Singh, A. Seabaugh, *Nanoscale research letters*, 6 (2011), article number 26, doi: 10.1007/s11671-010-975-0
- <sup>7</sup> D. Mandrino, M. Godec, M. Torkar, M. Jenko, *Surface and Interface Analysis*, 40 (2008), 3/4, 285–289
- <sup>8</sup> M. Torkar, M. Godec, M. Lamut, *Engineering Failure Analysis*, 14 (2007) 7, 1218–1223
- <sup>9</sup> M. Godec, D. Nolan, M. Jenko, *Materials science & engineering B, Solid-state materials for advanced technology*, B 129 (2006) 1, 31–38
- <sup>10</sup> M. Godec, D. Mandrino, M. Jenko, *Engineering Failure Analysis*, 16 (2009) 4, 1252–1261
- <sup>11</sup> M. Godec, A. Kocijan, D. Dolinar, D. Mandrino, M. Jenko, V. Antolič, *Biomedical Materials*, 5 (2010) 4, doi: 10.1088/1748-6041/5/4/045012
- <sup>12</sup> M. Jenko, F. Vodopivec, H. J. Grabke, H. Viehhaus, B. Praček, M. Lucas, M. Godec, *Steel Research*, 65 (1994) 11, 500–504
- <sup>13</sup> M. Jenko, F. Vodopivec, B. Praček, M. Godec, D. Steiner, *Journal of Magnetism and Magnetic Materials*, 133 (1994) 1–3, 229–232
- <sup>14</sup> M. Jenko, B. Korousic, D. Mandrino, V. Presern, *Vacuum*, 57 (2000) 3, 295–305
- <sup>15</sup> D. Mandrino, D. Vrbanic, M. Jenko, D. Mihailovic, S. Pejovnik, *Surface and Interface Analysis*, 40 (2008) 9, 1289–1293
- <sup>16</sup> D. Mandrino, M. Godec, M. Torkar, M. Jenko, *Surface and Interface Analysis*, 40 (2008) 3–4, 285–289
- <sup>17</sup> B. S. Batic, M. Jenko, *Journal of Vacuum Science & Technology A, Vac. surf. films*, 28 (2010) 4, 741–744
- <sup>18</sup> B. S. Batic, M. Jenko, *Surface and Interface Analysis*, 42 (2010) 6–7, 703–706
- <sup>19</sup> A. Minovič, I. Milošev, V. Pišot, A. Cör, V. Antolič, *J. bone jt. surg.*, 83-B (2001) 8, 1182–1190
- <sup>20</sup> A. Kocijan, M. Conradi, *Mater. Tehnol.*, 44 (2010), 1, 21–24
- <sup>21</sup> A. Kocijan, D. K. Merl, M. Jenko, *Corrosion Science*, 53 (2011) 2, 776–783
- <sup>22</sup> V. Leskovšek, B. Podgornik, M. Jenko, *Wear*, 266 (2009) 3/4, 453–460
- <sup>23</sup> D. A. Skobir, M. Jenko, D. Mandrino, *Surface and Interface Analysis*, 36 (2004) 8, 941–944
- <sup>24</sup> J. Vojvodič-Tuma, B. Šuštaršič, R. Celin, F. Vodopivec, *Mater. Tehnol.*, 43 (2009) 4, 179–187
- <sup>25</sup> J. Vojvodič-Tuma, B. Šuštaršič, F. Vodopivec, *Nucl. Eng. Des.*, 238 (2008) 7, 1511–1517
- <sup>26</sup> D. B. Williams, C. B. Carter, *Transmission Electron Microscopy: A Textbook for Materials Science*, 2<sup>nd</sup> ed., Springer, New York 2009, pp. 832

- <sup>27</sup> J. Ayache, L. Beaunier, J. Boumendil, G. Ehret, D. Laub, *Sample Preparation Handbook for Transmission Electron Microscopy: Methodology*, Springer, New York 2010, pp. 250
- <sup>28</sup> J. Ayache, L. Beaunier, J. Boumendil, G. Ehret, D. Laub, *Sample Preparation Handbook for Transmission Electron Microscopy: Techniques*, Springer, New York 2010, pp. 338
- <sup>29</sup> R. M. Anderson, S. D. Walck, *Specimen Preparation for Transmission Electron Microscopy of Materials IV*, Materials Research Society Symposium Proceedings Volume 480, San Francisco, **1997**, 295
- <sup>30</sup> I. Paulin, B. Sustarsic, V. Kevorkijan, S. D. Skapin, M. Jenko, *Mater. Tehnol.*, **45** (2011) 1, 13–19
- <sup>31</sup> I. Paulin, D. Mandrino, C. Donik, M. Jenko, *Mater. Tehnol.*, **44** (2010) 2, 73–76
- <sup>32</sup> V. Kevorkijan, S. D. Skapin, I. Paulin, B. Sustarsic, M. Jenko, *Mater. Tehnol.*, **44** (2010) 6, 363–371
- <sup>33</sup> C. Donik, A. Kocijan, D. Mandrino, I. Paulin, M. Jenko, B. Pihlar, *Applied Surface Science*, **255** (2009) 15, 7056–7061
- <sup>34</sup> C. Donik, A. Kocijan, J. T. Grant, M. Jenko, A. Drenik, B. Pihlar, *Corrosion Science*, **51**(2009) 4, 827–832
- <sup>35</sup> C. Donik, D. Mandrino, M. Jenko, *Vacuum*, **84** (2010) 11, 1266–1269
- <sup>36</sup> F. Andreatta, H. Terryn, J. H. W. de Wit, *Electrochimica Acta*, **49** (2004), 2851–2862

## MODELLING OF HOT TEARS IN CONTINUOUSLY CAST STEEL

### MODELIRANJE VROČIH RAZPOK V KONTINUIRNO LITEM JEKLU

Vladimir Grozdanić

University of Zagreb, Metallurgical faculty, Aleja narodnih heroja 3, 44103 Sisak, Croatia  
grozdan@simet.hr

Prejem rokopisa – received: 2011-03-15; sprejem za objavo – accepted for publication: 2011-04-21

A problem that appears in continuously cast strands, during the solidification process, is the so-called hot tears. Here, these phenomena are formulated and investigated. The criteria for the beginning of hot tears in Al-alloys are derived in the literature and applied for continuously cast steel. The influence of the carbon content in the systems Fe-C-P and Fe-C-S with respect to the sensitivity of the alloy to hot tears is investigated. Finally, when implemented in a FEM model of continuously cast steel and using the CALCSOFT package, these criteria may predict cracks in the strand centre of continuously cast steel.

Key words: continuous casting of steel, hot tears, modelling, RDG criteria.

Raziskan je bil nastanek in izvršeno modeliranje nastanka vročih razpok pri strjevanju kontinuirno lite gredice. Kriteriji za nastanek vročih razpok v Al-zlitinah so povzeti po literaturi in uporabljeni pri kontinuirno litem jeklu. Raziskan je bil vpliv ogljika v sistemih Fe-C-P in Fe-C-S s stališča občutljivosti za nastanek vročih razpok. Z FEM-modelom kontinuirno litega jekla in z uporabo paketa CALCSOFT se lahko po teh kriterijih napove nastanek razpok v sredini žile kontinuirno litega jekla.

Ključne besede: kontinuirno litje jekla, vroče razpoke, modeliranje, RDG-kriteriji

## 1 INTRODUCTION

Hot tears are a surface discontinuity or cracking caused either by external loads or internal stresses, or a combination of both acting on the casting during solidification, and subsequent contraction at temperatures near the solidus<sup>1</sup>. Hot tears in steel castings are well documented in the literature.<sup>2,3</sup> In ref.<sup>4</sup> they develop a mathematical model for determining the critical time for the  $\gamma \rightarrow \alpha$  transformation, which may generate internal stresses and cracks, based on the temperature distribution in the strand of the continuously cast steel in the zone of secondary cooling. The tearing mechanism also depends on the composition of the interdendrite liquid films in the critical temperature interval above the solidus temperature. This temperature may be considerably below the solidus temperature for most alloys, as these films are enriched with impurity elements. In ref.<sup>5</sup> it is assumed that for steel the critical value of the fracture deformation is something below 0.2 %. The scheme of continuous casting is given in **Figure 1**.

Vertical, continuous casters are used for almost all families of metal alloys, while horizontal casters are completely employed for metal melts up 1100 °C. In vertical, continuous casters (**Figure 2**) a number of phenomena are important for the process control, in particular the gap and its ramifications, the shell thickness ( $s$ ) and the sump length ( $l$ ). The problems of control of the casting (i.e., solidification or withdrawal) speed ( $v$ ), gap lubrication, chill (oscillatory) movement, the forming of surface striations on the strand, crack formation due to

the interaction of the soft shell with transport rolls, microstructure formation and segregation phenomena.<sup>7</sup>

For numerical modelling an FEM-based algorithm is normally applied. The cooling and solidification of the strand are described with the energy equation. The thermal calculations serve as an input for the thermo-mechanical simulation of the development of stress and strain fields in the strand during the solidification. In this way, stresses and strains within the critical temperature range are calculated and related to the critical fracture

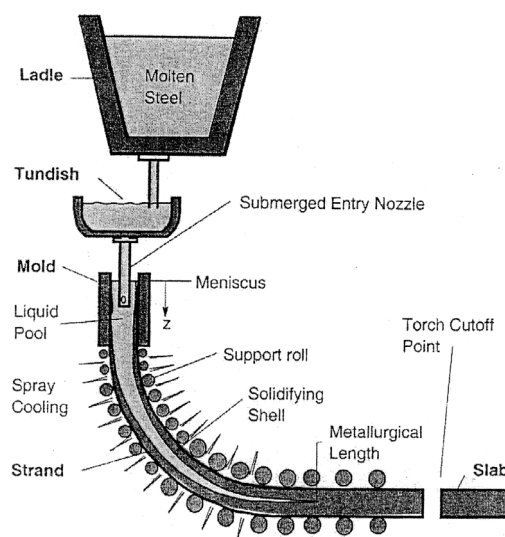
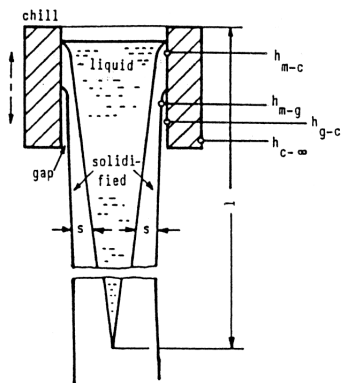


Figure 1: Scheme of the continuous casting process.<sup>6</sup>

Slika 1: Shema procesa kontinuirnega litja



**Figure 2:** Scheme of a vertical, continuously cast strand<sup>7</sup>  
**Slika 2:** Shema pokončno lite kontinuirne žile<sup>7</sup>

level to simulate whether cracking will occur. The modelling of the process parameters in continuous casting, i.e., primary cooling, (secondary) water-spray cooling, withdrawal rate, pouring temperature, etc. with respect hot-cracking susceptibility has, among other things, turned out to be essential for process optimization. The hot-cracking problem provides an interesting bridge between two disciplines: the thermal (temperature fields) and the mechanical (stress fields). It was proposed<sup>7</sup> to use both the FDM and FEM enmeshment techniques to calculate the thermal conditions, utilizing the former and to compute the mechanical stresses and strains using the latter. The superimposition of two (or more) types of algorithms for treating interactively different simulation tasks will become more and more important in the future.

In this work, criteria for the formation of hot tears are derived for steel, developed in<sup>8</sup> and called the RDG criteria. By applying the microstructural approach<sup>9</sup> to the model of the solidification of alloys in the system Fe-C-P and Fe-C-S, it is estimated that the influence of the concentration of carbon, phosphorus and sulphur on the formation of hot tears and compared with usual practise. Finally, preliminary results obtained by the implementation of hot tearing in the FEM package CALCOSOFT, applied to continuous casting, are shown.

## 2 APPLICATION OF THE RDG CRITERIA TO HOT TEARS IN STEEL

A detailed description of the RDG model applied to Al-alloys can be found in ref.,<sup>10</sup> and here the derivation of the model for steels is shown. A schematic presentation of the dendrite growth of steel is shown in **Figure 3**.

It is assumed that the dendrites grow in the direction of the temperature gradient ( $G$ ) with the velocity ( $v_T$ ). Above a certain fraction of solid volume, the total flux of mass cannot compensate for the contraction, as the specific mass of the solid is greater than that of liquid. So, the liquid must flow across interdendritic spaces. If the dendrite net is subjected to tensile deformation ( $\epsilon$ )

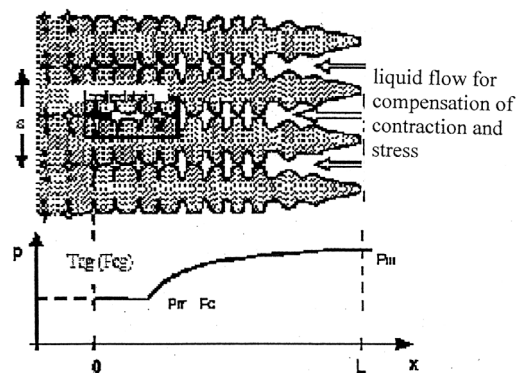


**Figure 3:** Schematic presentation of the hot tears forming between grains as a result of the local stress of the solid. The decrease of the pressure in the interdendritic liquid is also shown.

**Slika 3:** Shematičen prikaz vročih razpok med kristalnimi zrnji, nastalimi zaradi lokalnih napetosti v trdnem. Prikazan je tudi zmanjšanje pritiska v talini med dendriti.

perpendicular to the temperature gradient, then deformation is necessary for the compensation, otherwise hot tears will form. The pressure in the interdendritic liquid (**Figure 3**) will decrease from the metallostatic pressure ( $p_m$ ), on the dendrite tips, to the lower value in the mushy zone. Above the temperature of mass feeding ( $T_{mf}$ ) the grains are not joined and the liquid may move freely. On the other hand, below the temperature at which the grains are joined ( $T_{cg}$ ), all the dendrites make a coherent mesh, which may support the thermal stress caused by the cooling. The temperatures at which the grains are joined depend on their disorientation and so they are not unique. Between  $T_{mf}$  and  $T_{cg}$ , the liquid emulsion may resist the cavitation pressure at which the hole is nucleated, and it may form hot tears. Eventually, the gap of the continuous interdendritic emulsion, between grains, may not be enough to compensate for the feeding from the upper mesh zone because of the great fraction of solid, i.e., the low permeability. The RDG criteria are based on the derivation of two pressure drops, connected with the deformation and the contraction. With that aim, a mass balance is derived for small volume elements of the mushy zone in the referent frame connected with the isotherms<sup>8</sup>.

The case of steel is more complex because during the progress of solidification two phases are formed:  $\delta$  (ferrite) at a lower carbon content, and  $\gamma$  (austenite) at a higher concentration of carbon. Assuming that cavities are not formed, the sum of volume fraction of different phases (liquid, ferrite, austenite) is given by equation (1):

$$1 = f_l + f_s = f_l + f_\delta + f_\gamma \quad (1)$$

Assuming that the specific masses of all the phases ( $\rho_\delta, \rho_\gamma, \rho_l$ ) are constant, two factors of solidification contraction are defined:

$$\beta_\gamma = \frac{\rho_\gamma - \rho_l}{\rho_l} \text{ and } \beta_\delta = \frac{\rho_\delta - \rho_l}{\rho_l} \quad (2)$$

For steel,  $\beta_\gamma$  and  $\beta_\delta$  are 5.1 % and 3.6 %<sup>11</sup>, respectively. The liquid speed is connected with the pressure gradient in the liquid with the Darcy equation. The permeability of the mushy zone is calculated with the Carman-Kozeny approximation:<sup>8</sup>

$$K = \frac{\lambda^2(1-f_s)^3}{180f_s^2} \quad (3)$$

where  $\lambda$  is the distance that characterizes the curve of the mushy media. If the liquid flows only in the direction of the temperature gradient and two solid phases ( $\delta$  and  $\gamma$ ) are deformed identically in the transversal direction, the pressure of the mush is:

$$p = p_a + \rho gh - \Delta p_{sh} - \Delta p_{mec} \quad (4)$$

where  $p_a$  is the atmospheric pressure,  $\rho gh$  is the metallostatic contribution,  $\Delta p_{sh}$  and  $\Delta p_{mec}$  is the contribution of the pressure drop in the mushy zone because of the contraction during solidification and deformation. In stable conditions and assuming an equalized temperature gradient ( $G$ ) in the mush, the contribution of the contraction is calculated in the following way:

$$\Delta p_{sh} = \frac{180\mu v_T}{\lambda^2 G} (\beta_\gamma A_\gamma + \beta_\delta A_\delta) = A \frac{180\mu v_T}{\lambda^2 G} \quad (5)$$

where

$$A_T = \int_{T_{cg}}^{T_{liq}} \frac{(f_i^0 - f) f_s^2}{(1-f_s)^3} dT, i = \delta \text{ or } \gamma \quad (6)$$

where  $\mu$  is the viscosity of the liquid phase, and  $f_i^0$  is the volume fraction of ferrite ( $i = \delta$ ) or austenite ( $i = \gamma$ ) at the end of the solidification, and their sum is 1.

Assuming an equalized mechanical deformation of the whole mush ( $\epsilon$ ), the mechanical contribution is:

$$\Delta p_{mec} = \frac{180\mu\epsilon}{\lambda^2 G^2} [(1+\beta_\delta)B_\delta + (1+\beta_\gamma)B_\gamma] = B \frac{180\mu\epsilon}{\lambda^2 G^2} \quad (7)$$

with

$$\beta_i = \int_{T_{cg}}^{T_{liq}} \frac{f_s^2 |f_i dT|}{(1-f_s)^3} dT, i = \delta \text{ or } \gamma \quad (8)$$

The fusion temperature ( $T_{cg}$ ) corresponding to the solid fraction of 99 % between two grains is lower (approximately 95 %) for two dendrites of the some grain<sup>11</sup>.

Equation (5) shows the contribution of the contraction, which is proportional to the contraction factors and the velocity isotherms, while the mechanical contribution (eq. 7) is proportional to the stress. The two contributions are inversely proportional to the square of the secondary spacing of the dendrite sleeve ( $\lambda$ ). The parameters  $A_i$  and  $B_i$  depend on the steel composition and the solidification flow, i.e., on the relation between  $f_s$ ,  $f_\delta$ ,  $f_\gamma$  and  $T$ . They can be calculated using the back-diffusion model<sup>9</sup> or any of the complex numerical micro-segregation models.

Finally, if the pressure ( $p$ ), obtained with eq. 4, drops below the cavitation pressure ( $p_c$ ), hot tears are formed. These criteria make it possible to calculate the maximum stress that the mushy zone can support ( $\epsilon^{\max}$ ) and the susceptibility to hot cracking (HCS) may be defined as:

$$HCS = \frac{1}{\epsilon^{\max}} \quad (9)$$

If  $HCS$  is greater than 1, the alloy and solidification conditions are more susceptible to tearing.

### 3 INFLUENCE OF THE C, P AND S CONTENTS ON THE FORMATION OF HOT TEARS

Carbon diffuses relatively well in ferrite and austenite, whereas phosphorus and sulphur diffuse slowly. These elements formed interdendritic segregates with a low fusion point. The integrals  $A_i$  and  $B_i$  in equations (6) and (8) are calculated using the Clyne and Kurz segregational approach for steels.<sup>9</sup> **Figure 4** shows the distribution of the liquid, solid,  $\delta$  and  $\gamma$  phases during the solidification process of Fe-0.15 % C-0.03 % P. In this case it is assumed that no residual ferrite is present after

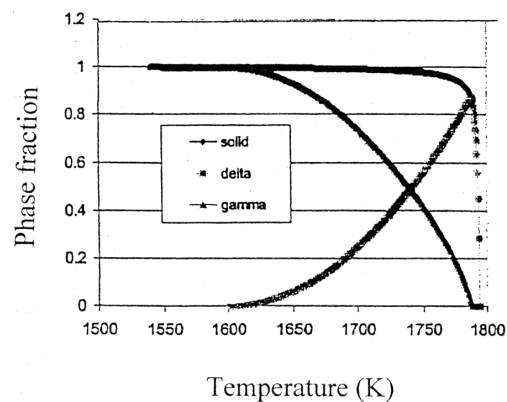


**Figure 4:** Solidification of the alloy Fe-0.15 % C-0.03 % P  
**Slika 4:** Strjevanje zlitine Fe-0.15 % C-0.03 % P

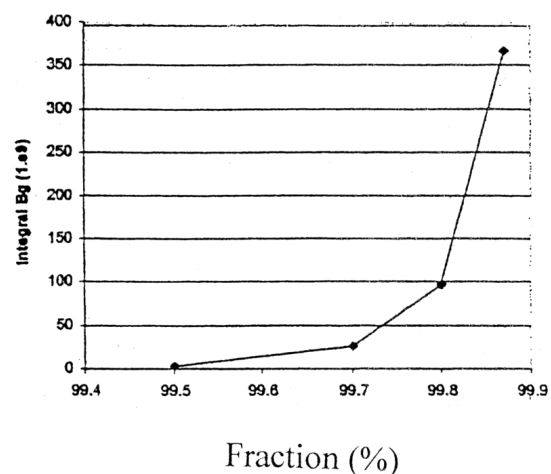


**Figure 5:** Influence of  $F_{cg}$  on  $B_\gamma$  for alloy Fe-0.15 % C-0.03 % P  
**Slika 5:** Vpliv  $F_{cg}$  na  $B_\gamma$  za zlitino Fe-0.15 % C-0.03 % P

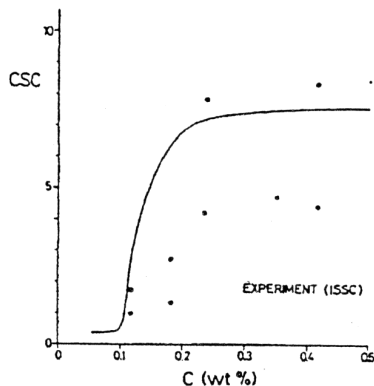


Figure 6: ISSC as a function of carbon content  
Slika 6: ISSC kot funkcija vsebnosti ogljika

the end of the solidification. The integrals  $A_i$  and  $B_i$  can be calculated using the curves shown in Figure 4. The lower integral boundary ( $T_{cg}$ ), or solid fraction ( $F_{cg}$ ), have a great influence on the value of the integral, as is shown in Figure 5 for  $B_\gamma$ . All the integrals tend to infinity when  $F_{cg}$  tends to 1.  $F_{cg}$  depends on the P and S content in the residual interdendritic liquid emulsion.

On the basis of integrals  $A_i$  and  $B_i$  it is possible to classify the alloys with regard to hot-tearing susceptibility. The increase of the integrals leads to an increase of the pressure drop obtained with eq. (4), for defined thermo-mechanical conditions. Figures 6 and 7 compare the results obtained with the model for hot tears (integral  $B_\gamma$ ) with a change in the index of cracking below the surface (ISSC). For a carbon content below of 0.1 % the alloy solidifies only in the  $\delta$  structure, and with an increase of the carbon content the solidification ends in the  $\gamma$  structure.

Figure 8 shows the dependence of the integral  $B_\gamma$  on the phosphorus content for two values of  $F_{cg}$ .

Figure 8 shows that a slight increase in the phosphorus content increases the susceptibility to hot tearing. Figure 9 shows the calculated distribution of the liquid, solid,  $\delta$  ferrite and  $\gamma$  austenite phases during the solidification of Fe-0.14 % C-0.01 % S when approximately

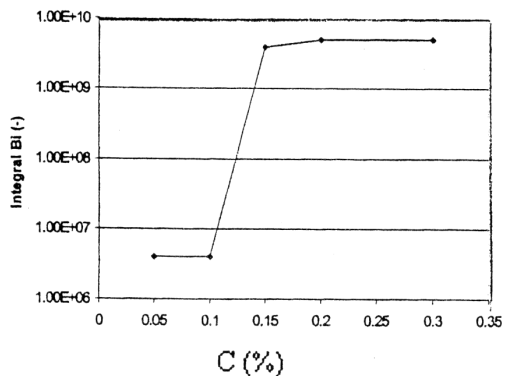


Figure 7: Integral  $B_\gamma$  as a function of carbon content  
Slika 7: Integral  $B_\gamma$  kot funkcija vsebnosti ogljika

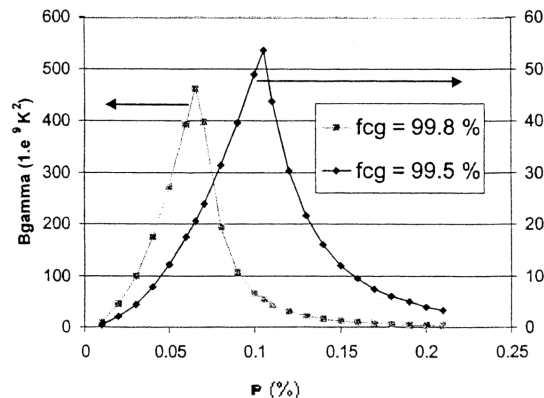


Figure 8: Integral  $B_\gamma$  as a function of the phosphorus content for two values of  $F_{cg}$

Slika 8: Integral  $B_\gamma$  kot funkcija vsebnosti fosforja za dve vrednosti  $F_{cg}$

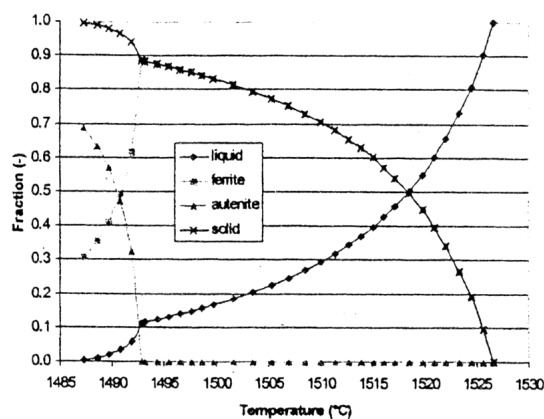


Figure 9: Calculated process of solidification for the alloy Fe-0.14 % C-0.01 % S

Slika 9: Izračunan način strjevanja zlitine Fe-0.14 % C-0.01 % S

30 % of residual ferrite is present after the end of the solidification.

The integrals  $A$  and  $B$  are calculated for a solid fraction  $F_{cg}$  of 99 %. The results are shown in Figure 10 for a sulphur content of 0.01 %, and without sulphur.

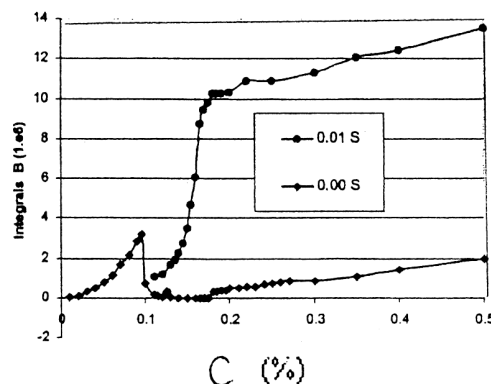


Figure 10: Influence of carbon content on the integral  $B$  for two sulphur contents

Slika 10: Vpliv vsebnosti ogljika na integral  $B$  za dve vsebnosti ogljika

Parameter  $B$  quickly increases at approximately 0.15 % C, and then continue to increase, but slightly slower for larger carbon contents.

#### 4 APPLICATION OF THE MODEL TO CONTINUOUSLY CAST STEEL

The results obtained using the RDG approach on a FEM thermal model of continuous casting implemented in CALCOSOFT<sup>12</sup> are shown in **Figure 11 and 12**. **Figure 11** shows a 3-D temperature field obtained in



**Figure 11:** 3-D temperature field of continuously cast steel (half of strand)

**Slika 11:** 3-D temperaturno polje in polje deleža trdnega pri kontinuirnem litju jekla (polovica žile)

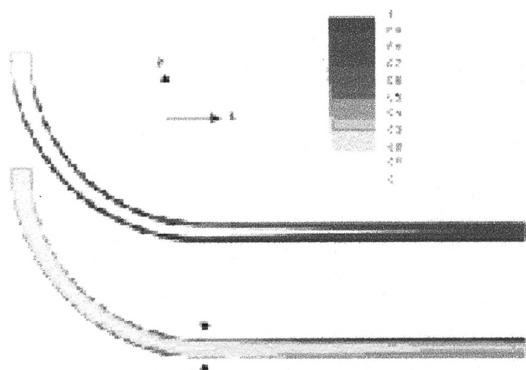


**Figure 12:** 2-D temperature field and solid-fraction field during continuously cast steel (central plane)

**Slika 12:** 2-D temperaturno polje in polje deleža trdnega pri kontinuirnem litju jekla (centralna ravnina)

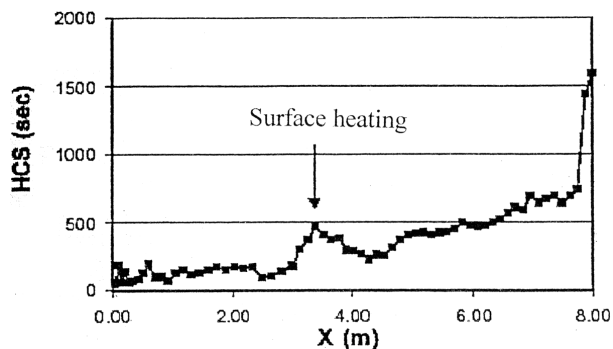


**Figure 13:** Susceptibility to hot tears ( $HCS$ ) as a function of the casting length ( $x$ )

**Slika 13:** Občutljivost za vroče razpoke ( $HCS$ ) v odvisnosti od dolžine litja ( $x$ )

stable conditions with a space-dependent velocity of flow. The temperature fields and the solid-fraction fields are shown in **Figure 12** for the central surface of the strand.

Equation (9), implemented in thermal model and the distribution of sensibility to hot tears along the casting, is shown in **Figure 13**.

The susceptibility to hot tears ( $HCS$ ) increases with the progress of solidification inside the slab. The maximum is immediately after point of equalizing, and can occur with the appearance of cracks in the center.<sup>5</sup> The maximum value of susceptibility to hot tears ( $HCS$ ) is in the liquid phase, where two shells collide and solidification occurs.

#### 5 CONCLUSION

The Rappaz-Drezet-Gremaud (RDG) criteria for the formation of hot tears (the two-phase model in which the deformation of the solid and the flow of the interdendritic liquid are examined) are derived for steels. The influence of the C, P and S contents agree with the production data and confirms the very significant influence of sulphur on the susceptibility to hot tearing. One of pre-conditions for the application of this approach is a good knowledge of the path of alloy solidification, especially in cases with only a small amount of liquid, in conditions of solidification in practice. Using these criteria in the thermal model of continuously cast steel, cracks can be predicted in the centre. To analyse the effects of deformation to which slab was submitted, like the bulge between the rolls because of the ferrostatic pressure in the continuous caster, no levelling of the rolls and twisting of the strand, these criteria can be applied in thermo-mechanical models of continuous casting.

#### 6 LITERATURE

- <sup>1</sup> D. C. Gould, AFS Metalcasting Dictionary, AFS, Des Plaines, 1968
- <sup>2</sup> V. Grozdanić, V. Novosel - Radović, R. Dmitrović, AFS Transactions, 100 (1992), 265–272
- <sup>3</sup> V. Grozdanić, Metallurgy, 29 (1990) 4, 123–128
- <sup>4</sup> V. Grozdanić, A. Markotić, Materiali in tehnologije, 38 (2004) 6, 303–306
- <sup>5</sup> J. K. Brimacombe, K. Sorimachi, Metall. Trans., 8B (1977), 489
- <sup>6</sup> B. G. Thomas, Modeling of Continuous Casting, The Making, Shaping and Treating of Steel, 11th ed., Casting Volume, The AISE Steel Foundation, Pittsburg, 2003
- <sup>7</sup> P. R. Sahn, P. N. Hansen, Numerical Simulation and Modelling of Casting and Solidification Process for Foundry and Cast-House, CIATF, Zürich, 1984
- <sup>8</sup> M. Rappaz, J. M. Drezet, M. Gremaud, Metall. Trans., 30A (1999) 2, 449–455
- <sup>9</sup> T. W. Clyne, M. Wolf, W. Kurz, Metall. Trans., 13B (1982) 6, 259
- <sup>10</sup> J. M. Drezet, M. Rappaz, Light Metals, TMS, New Orleans, 2001, 887–893
- <sup>11</sup> W. Kurz, D. J. Fisher, Fundamentals of Solidification, Trans. Tech. Publ., Aedermannsdorf, 1989
- <sup>12</sup> Calcsoft user manual, Calcom SA, <http://www.calcom.ch>, CH-1015 Lausanne, Switzerland



# THERMODYNAMIC INVESTIGATION OF THE Al-Sb-Zn SYSTEM

## TERMODINAMSKA RAZISKAVA SISTEMA Al-Sb-Zn

**Grega Klančnik, Jožef Medved**

University of Ljubljana, Faculty of Natural Science and Engineering, Department of Materials and Metallurgy, Aškerčeva 12, SI-1000 Ljubljana, Slovenia  
grega.klančnik@omm.ntf.uni-lj.si

*Prejem rokopisa – received: 2011-01-26; sprejem za objavo – accepted for publication: 2011-02-22*

In this paper, thermodynamic calculations for the liquid alloys in the ternary Al-Sb-Zn system are presented. The general solution model (GSM) was used for the thermodynamic prediction of the liquid alloys in ternary Al-Sb-Zn at 1350 K. Oelsen's calorimetric method was used for the determination of the aluminium activity close to the Al-Zn sub-binary system. The Knudsen effusion method with a mass spectrometer (KEMS) was used for a determination of the zinc activity in the solid aluminium-rich corner.

Keywords: Al-Sb-Zn, thermodynamics, general solution model

V prispevku je predstavljen termodinamski izračun za taline v ternarnem sistemu Al-Sb-Zn. Za napoved termodinamskih lastnosti pri 1350 K smo uporabili splošen model raztopin (GSM). Uporabili smo Oelsenovo kalorimetrijo za določitev aktivnosti aluminija v bližini binarnega sistema Al-Zn. Ravno tako smo uporabili Knudsenovo efuzijsko metodo z masnim spektrometrom (KEMS). Tako smo določili aktivnost cinka v aluminijevem kotu.

Ključne besede: Al-Sb-Zn, termodinamika, splošni model raztopin

## 1 INTRODUCTION

The determination of the thermodynamic properties of the Al-Sb-Zn system is important. In order to investigate lead-free alloys for high temperature solders<sup>1</sup> or classical applications<sup>2</sup>, three different thermodynamic prediction methods were used: Chou, as the general solution method (GSM); asymmetric Toop; and the symmetric Muggianu method<sup>3</sup>. The experimental results were compared to the mentioned thermodynamic models in the ternary Al-Sb-Zn system, in the section with the molar ratio  $w(\text{Zn}) : w(\text{Sb}) = 9 : 1$  at 1000 K and 1350 K. No ternary interaction parameters were used in these calculations.

## 2 EXPERIMENTAL

Oelsen's calorimetry was used for the experimental determination of the thermodynamic properties in the ternary liquid system Al-Sb-Zn. Some of the experimental data in the Al-Zn binary system were determined with the Knudsen's effusion method. Mono-atomic zinc and oligomeric antimony are present further in the Al-Sb-Zn ternary system; the Knudsen cell was equipped with a mass spectrometer (KEMS). The measurements were made in the Al-rich corner only, at low temperatures since the volatility of the zinc and antimony was high.

### 2.1 The Knudsen effusion method

The Al-Zn binary system was investigated by applying Knudsen's effusions method. In the effusion method the vapour pressure  $P$  is calculated using the effusion velocity with the equation:

$$P = \sqrt{\frac{2\pi RT}{M}} \cdot \frac{1}{kA} \cdot \frac{G}{\tau} \cdot \left(1 + \frac{kA}{\alpha B}\right) \quad (1)$$

where  $A$  is the geometric area of the effusion orifice,  $kA$  is the effective area,  $K$  is the Clausing factor,  $B$  is the effective vaporization area,  $M$  is the molecular weight of the effusing molecule,  $R$  is the gas constant,  $G$  is the weight of the effused molecule and  $\tau$  is the time.

If we consider that the product  $\alpha B$  is much higher than  $kA$ , equation 1 is obtained as:

$$P \cdot kA = \sqrt{\frac{2\pi RT}{M}} \cdot \frac{G}{\tau} \quad (1.1)$$

And further:

$$\frac{p_i \cdot kA}{p_i^0 \cdot kA} = a_i \quad (1.2)$$

The measurements for the Al-Zn alloys were made at 833 K in vacuum. The system was evacuated to a pressure of  $10^{-3}$  mbar. About 0.3 g of charge material was placed in the  $\text{Al}_2\text{O}_3$  crucible. The purities of the metals were 99.99 % for the zinc as well as for the aluminium. To ensure the saturation of the vapour phase, the lid was extra sealed on the  $\text{Al}_2\text{O}_3$  crucible so the effused molecules could have effused only from a small

orifice. After each experiment a zinc ring appeared on the inside of the crucible as a result of the saturation of the zinc. The measurements for the Al-Zn-Sb ternary system were made in the temperature range 478–566 K to prevent instrumental errors as a result of the large evaporation of zinc and antimony.

In KEMS, the partial pressure is relative to any species at temperature  $T$  and is correlated to the ion intensity<sup>4,5</sup>:

$$p_j = \frac{kTI_{jk}^*}{\sigma_j \eta_k \gamma_k} \quad (2)$$

$\sigma_j$  – ionization cross-section of species,

$K$  – instrumental constant,

$I_{jk}^*$  – intensity of ion  $k$  formed from the molecular species  $j$ ,

$T$  – absolute temperature inside the Knudsen cell,

$\eta_k$  – isotope abundance,

$\gamma_k$  – multiplier efficiency for ion  $k$ .

The partial pressure ratio can be determined without knowledge of the values of the equation parameters just by measuring the ion intensity between two species relative to the temperature. In order to conduct the measurement, at least 300 mg of each species in a powdered state is necessary.

## 2.2 The Oelsen Calorimetry method

The Oelsen Calorimetry used in this paper is based on classic calorimetry as a classic thermodynamic method. Based on equation (3) a tangent construction for a determination of  $-R \ln a_{x,T}$  was made at 1000 K and 1350 K in the specific section (**Figure 1**)<sup>6</sup>.

$$-\frac{G_i^M}{T} = \int_{1/T_0}^{1/T} H_{x,T} d\left(\frac{1}{T}\right) = -R \ln a_i \quad (3)$$

where  $G_i^M$  is the partial molar Gibbs energy for the component  $i$ . The measurements were made in an interval from  $T_0$  to  $T$ . Each measurement gives a measured enthalpy value  $H_{x,T}$  for the composition  $x$  at temperature  $T$ . The activities for the component  $i$  were derived using a tangent construction for the determination of  $-R \ln a_{x,T}$ . Apart from the activities values, the activity coefficients and other thermodynamic properties were also determined.

A type-K thermocouple (Ni-NiCr) was used for the temperature measurements. To achieve the best sensitivity possible, relatively thin wires were used. The preparation of samples was made with metals of 99.99 % purity. The melting was made under an argon atmosphere in an Al<sub>2</sub>O<sub>3</sub> crucible. The measurements themselves were made in air. After each measurement the crucible with the sample was covered in order to prevent heat losses. The measurements were made with a calorimeter with a determined constant  $C_{\text{cal}} = 324.9 \text{ J K}^{-1}$ . The Al<sub>2</sub>O<sub>3</sub> crucible was taken into account while determining the  $C_{\text{cal}}$ .

## 2.3 Calculation of total excess Gibbs energy in the Al-Sb binary system at 1000 K

The calculation of the total excess Gibbs energy for the Al-Sb binary system at 1000 K was made on the basis of the following thermodynamic models: the unary phase model, the disordered solution phase model and the stoichiometric compound phase model.

The term for the unary phase is:

$${}^0G_i^\phi(T) = a + bT + cT^2 + dT^3 + eT^{-1} + fT^7 + hT^{-9} \quad (4)$$

where the  ${}^0G_i^\phi$  is the Gibbs energy for the pure element  $i$  with the structure  $\phi$  at 298.15 K. The liquid phase was calculated as a disordered solution phase and it is described with the following relation:

$$G^{\text{Liquid}} = x_i {}^0G_i^{\text{Liquid}} + x_j {}^0G_j^{\text{Liquid}} + RT(x_i \ln(x_i) + x_j \ln(x_j)) + {}^{\text{ex}}G^{\text{Liquid}} \quad (5)$$

where the excess Gibbs energy of the liquid phase is calculated through the Redlich-Kister polynomial relation, and  $x_i$  correspond to the mole fraction of component  $i$ :

$${}^{\text{xs}}G^{\text{Liquid}} = x_i x_j \sum_{n=0}^m ({}^nL_{i,j}^{\text{Liquid}} (x_i - x_j)^n) \quad (6)$$

and

$${}^nL_{i,j}^{\text{Liquid}} = a_n + b_n T \quad (7)$$

Only one stoichiometric phase appears in the Al-Sb binary system, and its Gibbs free energy is described with the following relation:

$$G^\phi = x_i {}^0G_i^{\phi 1} + x_j {}^0G_j^{\phi 2} + \Delta G_f \quad (8)$$

where  ${}^0G_{i,j}^{\phi 1,2}$  is the Gibbs free energy for the components  $i$  and  $j$  in standard states.  $\Delta G_f$  represents the Gibbs free energy of formation and is calculated from the parameters  $a$  and  $b$ :

$$\Delta G_f = a + bT \quad (9)$$

## 2.4 Prediction methods

Chou suggested the so-called general solution thermochemical model. The calculations were made using similarity coefficients determined through excess Gibbs energy data of the constituent binaries. In practise the GSM method gives good agreement with the experimental data. Two geometrical models were also used in this paper: the symmetric Toop and the asymmetric Muggianu model<sup>7,8,9</sup>.

### a) Chou model

The correlative term  $\eta_{i(ij,jk)}$  is calculated using the deviation square sum rule:

$$\eta_{i(ij,jk)} = \int_{x_i=0}^{x_i=1} (\Delta G_{ij}^{\text{xs}} - \Delta G_{ik}^{\text{xs}})^2 dx_i \quad (10)$$

**Table 1:** Thermodynamic parameters of the liquid Al-Sb-Zn system

**Tabela 1:** Termodinamski parametri taline v sistemu Al-Sb-Zn

System $ij$	$L_{ij}^0(T)$	$L_{ij}^1(T)$	$L_{ij}^2(T)$	$L_{ij}^3(T)$	$L_{ij}^4(T)$	Ref.
Al – Zn	$10466.6 - 3.39355T$					10
Al – Sb	$-13328 - 5.103T$	$10748 + 0.337T$				11
Sb – Zn	$-11740.942 - 0.1283T$	$-427.582 - 0.8090855T$	$34440.943 - 33.59286T$			12
Sb – Zn	$-43058.4 + 290.880T - 37.67392T \ln T$	$-11870.5 + 85.641T - 10.30928T \ln T$	$25102.1 - 14.005T$	$-9302.8 + 2.120T$	$-9191$	13

The similarity coefficients are calculated with the following relation:

$$\xi_{ij} = \eta_{i(ij,ik)} \cdot (\eta_{i(ij,ik)} + \eta_{j(ij,ik)})^{-1} \quad (11)$$

The ternary system can be expressed as:

$$x_{1(1,2)} = x_1 + x_3 \xi_{12} \quad (12)$$

$$x_{2(2,3)} = x_2 + x_1 \xi_{23} \quad (13)$$

$$x_{3(3,1)} = x_3 + x_2 \xi_{31} \quad (14)$$

The calculation was made on the basis of:

$$\begin{aligned} \Delta G^{xs} = & x_1 x_2 \left\{ (x_1 + \xi_{12} x_3)(x_2 + (1 - \xi_{12})x_3) \right\}^{-1} \Delta G_{12}^{xs} + \\ & + x_2 x_3 \left\{ (x_2 + \xi_{23} x_1)(x_3 + (1 - \xi_{23})x_1) \right\}^{-1} \Delta G_{23}^{xs} + \\ & + x_1 x_3 \left\{ (x_3 + \xi_{31} x_2)(x_1 + (1 - \xi_{31})x_2) \right\}^{-1} \Delta G_{31}^{xs} \end{aligned} \quad (15)$$

#### b) Toop model

$$\begin{aligned} \Delta G^{xs} = & \frac{x_2}{1-x_1} \Delta G_{12(x1)}^{xs} + \\ & + \frac{x_3}{1-x_1} \Delta G_{13(x1)}^{xs} + (x_2 + x_3) \Delta G_{23\left(\frac{x_2}{x_2+x_3}\right)}^{xs} \end{aligned} \quad (16)$$

#### c) Muggianu model

$$\begin{aligned} \Delta G^{xs} = & \frac{4x_1 x_2}{(1+x_1-x_2)(1+x_2-x_1)} \Delta G_{12\left(\frac{1+x_1-x_2}{2}\right)}^{xs} + \\ & + \frac{4x_2 x_3}{(1+x_2-x_3)(1+x_3-x_2)} \Delta G_{23\left(\frac{1+x_2-x_3}{2}\right)}^{xs} + \\ & + \frac{4x_3 x_1}{(1+x_3-x_1)(1+x_1-x_3)} \Delta G_{31\left(\frac{1+x_3-x_1}{2}\right)}^{xs} \end{aligned} \quad (17)$$

In each case, the partial thermodynamic quantities were calculated from:

$$G_i^{xs} = \Delta G^{xs} + (1-x_i) \left( \frac{\partial \Delta G^{xs}}{\partial x_i} \right) \quad (18)$$

The required binary parameters for the Al-Sb-Zn ternary system are presented in **Table 1**. The optimized

**Table 2:** The optimized parameters for the AlSb phase <sup>11</sup>
**Tabela 2:** Optimizirani parametri za fazo AlSb <sup>11</sup>

Phase	$a/(J/mol \text{ atom})$	$b/(J/mol \text{ atom K})$
AlSb	-40636	15.847

parameters for the stoichiometric Al-Sb phase are given in **Table 2**.

### 2.5 Liquidus surface construction

The effect of the AlSb phase on the shape of the liquidus surfaces was estimated by using the GSM prediction method from the calculated activities derived from the partial excess Gibbs energy in the ternary system and with projections of the liquidus lines from the sub-binaries, as already discussed before in this paper.

## 3 RESULTS AND DISCUSSION

### 3.1 Al-Zn binary system

The alumina crucible used had an inner diameter of 5 mm. The cover was also made from alumina with an orifice in the centre. About 200 mg to 300 mg of charge material was put inside the alumina crucible for each experiment. The zinc vapour was taken as monatomic. The measured thickness of the orifice was 0.23 mm. The effective area  $KA$  was calculated to be 0.277 mm<sup>2</sup>. The measurements were made at 833 K and the time for each measurement was less than 15 min. More details about the discussed method are available in ref. <sup>14</sup>. A type-S thermocouple was used for the temperature measurement. The measurements were made under a vacuum of 10<sup>-3</sup> mbar. The change in concentration during the experiment was taken into account. The measurement was made in the solid-liquid equilibrium in the aluminium-rich corner. The results are presented in **Table 3**.

**Table 3:** Experimental results from the Knudsen effusion method for the Al-Zn binary system at 833 K

**Tabela 3:** Eksperimentalni podatki, dobljeni s Knudsenovo efuzijsko metodo za sistem Al-Zn pri 833 K

Alloy	$P_{KA}/(\text{bar cm}^2)$	$P/\text{bar}$	$x_{Zn}$	$a_{Zn}$	$\gamma_{Zn}$	$G_{Zn}^{xs}/(J/mol)$
AZ1	$1.815 \cdot 10^{-6}$	$7.9497 \cdot 10^{-4}$	0.051	0.115	2.254	5628
AZ2	$5.226 \cdot 10^{-6}$	$2.2889 \cdot 10^{-3}$	0.199	0.331	1.663	3522
AZ3	$5.052 \cdot 10^{-6}$	$2.2177 \cdot 10^{-3}$	0.237	0.32	1.350	2078
AZ4	$5.803 \cdot 10^{-6}$	$2.5417 \cdot 10^{-3}$	0.305	0.365	1.196	1239
Zn	$1.59 \cdot 10^{-5}$	0.00698	1	1	/	0

3.2 Al-Sb-Zn ternary system

The calculated excess Gibbs energy for different ratios of aluminium, zinc and antimony are presented in **Figure 2**. All the calculations of the thermodynamic properties and the derivations in **Figure 2** were made using the GSM method at 1350 K.

The zinc activities are presented in **Figure 3** according to the three predicting models. All three thermodynamic models predicted negative deviations with respect to Raoult's law at the ratio  $w(\text{Al}) : w(\text{Sb}) = 1 : 4$ . The negativity is no longer present at the ratio 1 : 1 and this becomes more positive by approaching the sub-binary Al-Zn system. No significant differences exist between one and the other predicting methods.

The calculated activities of antimony at 1350 K throughout the entire concentration range show a

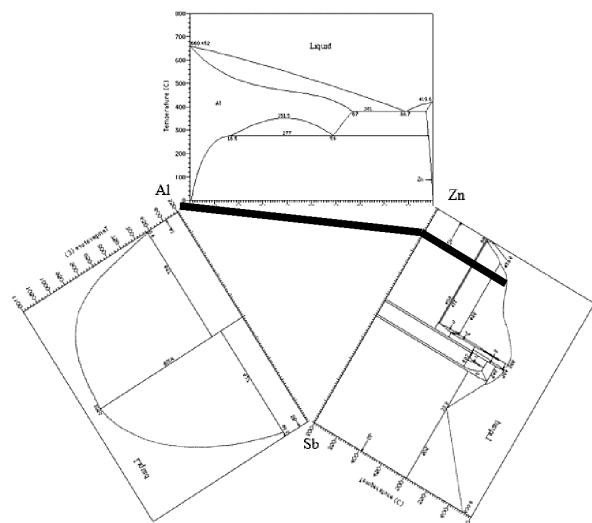


**Figure 1:** Experimental investigation of the section line with the ratio  $w(\text{Zn}) : w(\text{Sb}) = 9 : 1$

**Slika 1:** Eksperimentalna preiskava preseka z razmerjem  $w(\text{Zn}) : w(\text{Sb}) = 9 : 1$

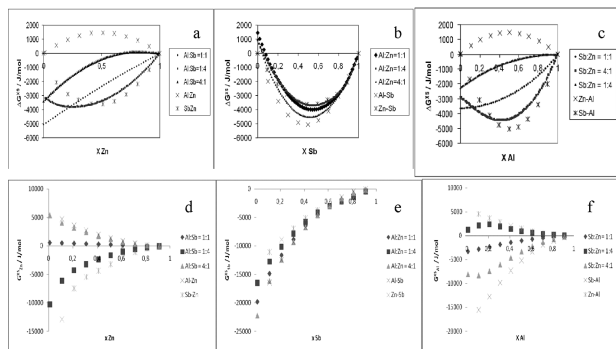


**Figure 2:** Excess Gibbs energy and partial excess Gibbs free energy of the liquid phase at 1350 K relative to: (a) zinc, (b) antimony and (c) aluminium. Partial excess Gibbs free energy relative to: (d) zinc, (e) antimony and (f) aluminium

**Slika 2:** Prebitne Gibbsove energije v posamezne Gibbsove proste energije tekoče faze pri 1350 K glede na: (a) cink, (b) antimony in (c) aluminij. Posamezne prebitne Gibbsove energije glede na: (d) cink, (e) antimon in (f) aluminij.

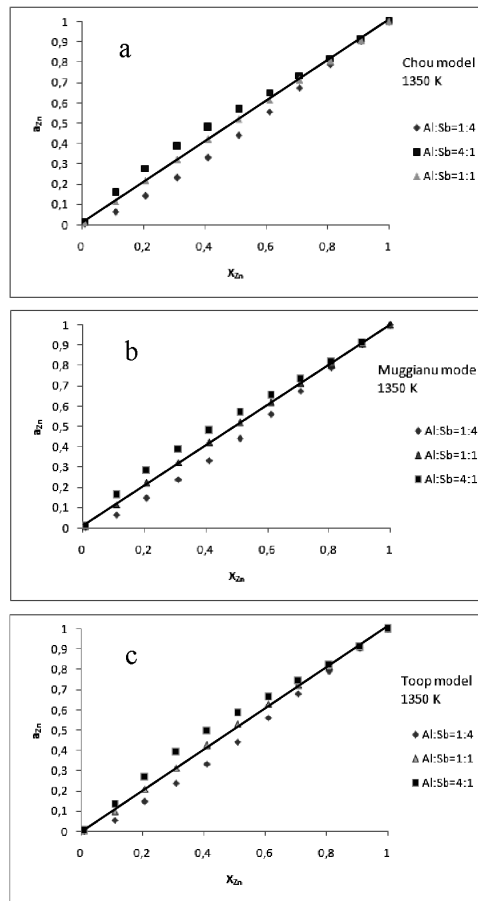


**Figure 3:** Zinc activities according to: (a) Chou, (b) Muggianu and (c) Toop model at 1350 K

**Slika 3:** Aktivnost cinka po: (a) Chou, (b) Muggianu in (c) Toop modelu za 1350 K

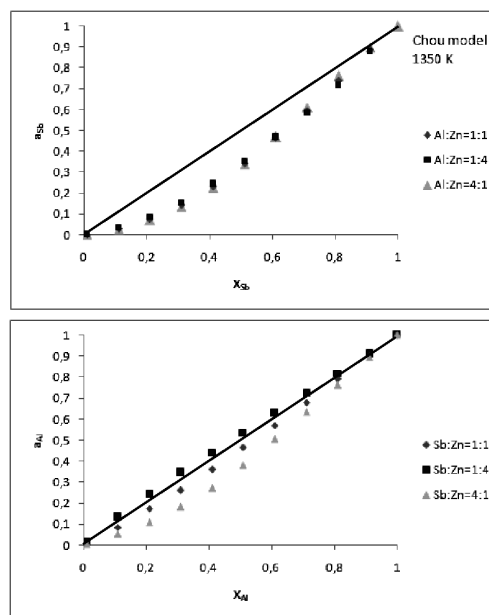


**Figure 4:** (a) Antimony and (b) aluminium activities according to Chou model at 1350 K

**Slika 4:** Aktivnost (a) antimona in (b) aluminija po modelu Chou za 1350 K

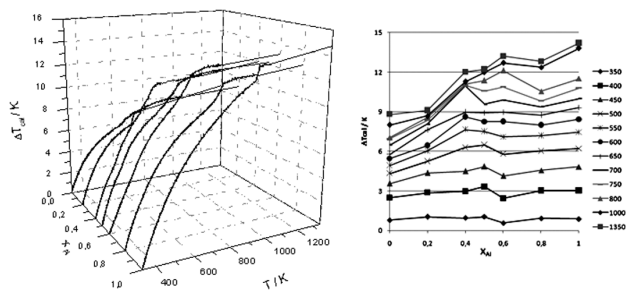


**Figure 5:** Enthalpy space diagram (a) and enthalpy isotherm diagram (b) for  $w(\text{Sb}) : w(\text{Zn}) = 1 : 9$  section inside the Al-Sb-Zn ternary system

**Slika 5:** Entalpijski prostorski diagram (a) in entalpijski izotermni diagram (b) v sistemu Al-Sb-Zn z razmerjem  $w(\text{Sb}) : w(\text{Zn}) = 1 : 9$

negative deviation from Raoult's law (**Figure 4a**). The difference of the activity values at different ratios is relatively small. The calculated aluminium activities are also negative, but already positive at the concentration ratio  $w(\text{Sb}) : w(\text{Zn}) = 1 : 4$  because of the influence of the positive excess Gibbs energy of the Al-Zn sub-binary system (**Figure 4b**).

The Oelsen calorimetric method was used for a determination of the activity of aluminium in the Al-Sb-Zn ternary system. The enthalpy space diagram and the corresponding enthalpy isotherm diagram are presented in **Figure 5**.

A positive integral mixing enthalpy is expected from the enthalpy isotherm diagram. However, a negative integral mixing enthalpy is present near the Zn-Sb binary system at higher temperatures as a result of a possible presence of an intermetallic compound. In this case the presence of the stoichiometric AlSb phase is expected.

A good agreement was achieved when comparing the calculated and the experimentally determined data (**Figure 6**). In both cases the activities of the aluminium are positive at both temperatures 1000 K and 1350 K. The data are presented in **Tables 4 and 5**.

**Table 4:** Results of Oelsen's thermodynamic analysis at 1350 K for  $w(\text{Zn}) : w(\text{Sb}) = 9 : 1$

**Tabela 4:** Rezultati Oelsenove termodinamske analize pri 1350 K za  $w(\text{Zn}) : w(\text{Sb}) = 9 : 1$

$x_{\text{Al}}$	$a_{\text{Al}}$	$\gamma_{\text{Al}}$	$G_{\text{Al}}^{\text{XS}}/(\text{J/mol})$	$G_{\text{Al}}^{\text{M}}/(\text{J/mol})$
0	/	/	/	/
0.2	0.246	1.23	2323	-15741
0.4	0.464	1.16	1666	-8619
0.5	0.561	1.12	1272	-6488
0.6	0.651	1.09	967	-4818
0.8	0.810	1.01	112	-2365
1	1	1	0	0

The calculation and the experimental determination of the concentration fluctuations in the long wavelength  $\text{Scc}(0)$  is an important tool for studying the segregation and/or presence of the chemical order. The calculation was made on the basis of the relation:

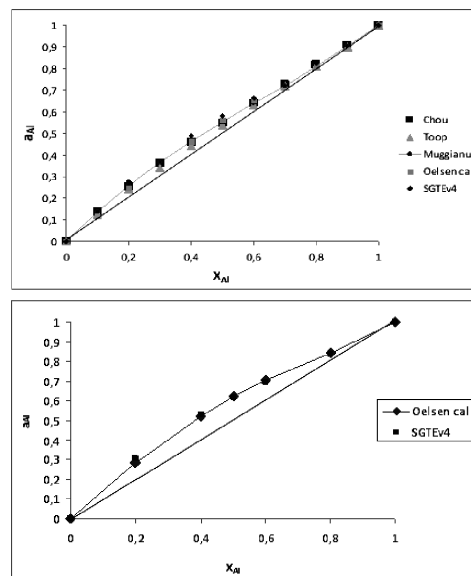


**Figure 6:** Activities obtained at: (a) 1350 K and (b) 1000 K for  $w(\text{Zn}) : w(\text{Sb}) = 9 : 1$

**Slika 6:** Določene aktivnosti za: (a) 1350 K in (b) 1000 K za  $w(\text{Zn}) : w(\text{Sb}) = 9 : 1$

**Table 5:** Results of Oelsen's thermodynamic analysis at 1000 K for  $w(\text{Zn}) : w(\text{Sb}) = 9 : 1$

**Tabela 5:** Rezultati Oelsenove termodinamske analize pri 1000 K za  $w(\text{Zn}) : w(\text{Sb}) = 9 : 1$

$x_{\text{Al}}$	$a_{\text{Al}}$	$\gamma_{\text{Al}}$	$G_{\text{Al}}^{\text{XS}}/(\text{J/mol})$	$G_{\text{Al}}^{\text{M}}/(\text{J/mol})$
0	/	/	/	/
0.2	0.285	1.43	2974	-10437
0.4	0.521	1.30	2181	-5421
0.5	0.62	1.24	1786	-3974
0.6	0.707	1.18	1376	-2883
0.8	0.842	1.05	406	-1430
1	1	1	0	0

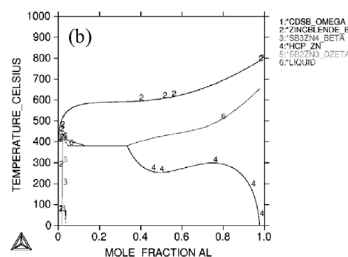
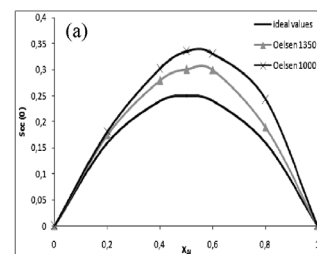


**Figure 7:** (a) Concentration fluctuations in the long wavelength  $\text{Scc}(0)$  at 1000 K and 1350 K for Al-ZnSb section and (b) the corresponding isopleth diagram

**Slika 7:** (a) Koncentracijska fluktuacija v dolgem redu dosega  $\text{Scc}(0)$  pri 1000 K in 1350 K za prerez Al-ZnSb in (b) pripadajoč izopletni diagram

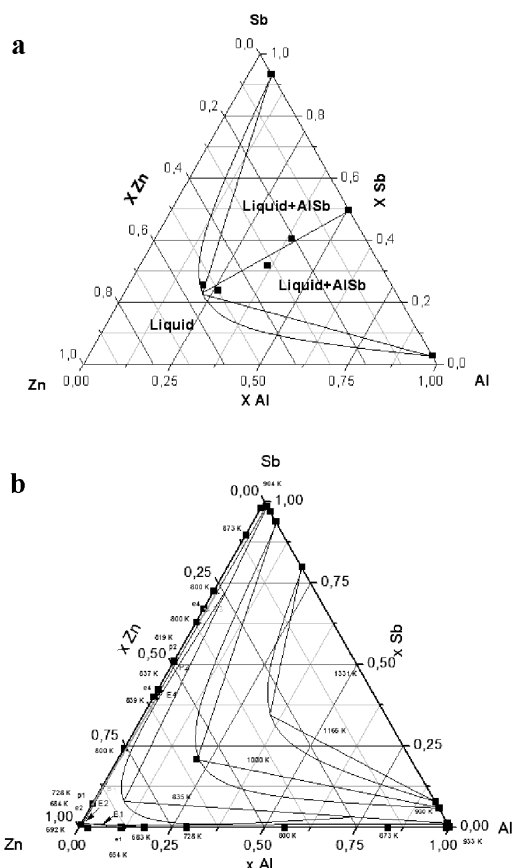


**Figure 8:** Thermodynamic prediction of the extension of two phase regions inside the ternary system at 1000 K using the GSM and projections of the sub-binaries with calculations.

**Slika 8:** Termodinamska napoved raztezanja dvofaznega območja v ternarnem sistemu pri 1000 K z uporabo GSM in binarnih projekcij

$$Scc(0) = \frac{(1-x_{Al})a_{Al}}{\partial a_{Al} / \partial x_{Al}} \quad (19)$$

The results of  $Scc(0)$  at 1000 K and 1350 K are presented in **Figure 7** and show a positive deviation from the ideal curve. This can be related to the presence of the miscibility gap in the solid and is also confirmed with the calculation of the isopleth phase diagram (**Figure**

**7b**). A tendency for decreasing the deviation from ideal values with an increasing temperature was also determined. It is worth mentioning that the calculated and experimentally determined  $Scc(0)$  are higher than the ideal in the zinc-rich corner at temperatures of 923 K in the Sb-Zn binary system, where the starting point of our measurements is located <sup>15</sup>. Nevertheless, the calculation was made using only aluminium activities.

The calculation in **Figure 8** shows that two phase region extend through the Zn-rich corner. No invariant reactions are expected at 1000 K inside the ternary Al-Sb-Zn system. From the literature we know that the liquid region is pushed to the Zn-rich corner in the sub-binary Al-Zn and Sb-Zn systems <sup>16</sup>.

The thermodynamic calculation using the SGTEv4 database predicts six invariant reactions in this system given in **Table 7**. The denotations for all the intermetallics in the Al-Sb-Zn system are given in **Table 8**.

**Table 7:** Predicted invariant reactions in the Al-Sb-Zn ternary system from the SGTEv4 database

**Tabela 7:** Napovedane invariantne reakcije v ternarnem sistemu Al-Sb-Zn s podatkovno bazo SGTEv4

E1	559.1 °C	$L \rightarrow \beta\text{-Sb}_2\text{Zn}_3 + \gamma\text{-Sb}_3\text{Zn}_4 + \text{AlSb}$
U1	538.44 °C	$L + \gamma\text{-Sb}_3\text{Zn}_4 \rightarrow \text{SbZn} + \text{AlSb}$
E2	509.29 °C	$L \rightarrow \text{SbZn} + (\text{Sb}) + \text{AlSb}$
P1	446.71 °C	$L + \beta\text{-Sb}_2\text{Zn}_3 + \text{AlSb} \rightarrow \alpha\text{-Sb}_2\text{Zn}_3$
E3	409.6 °C	$L \rightarrow (\text{Zn}) + \alpha\text{-Sb}_2\text{Zn}_3 + \text{AlSb}$
E4	380.7 °C	$L \rightarrow (\text{Al})^* + (\text{Zn}) + \text{AlSb}$

\* (Al) or  $\beta$ -Al phase.  $\beta$ -Al phase decomposes at lower temperature to  $\alpha$ -Al + (Zn)

**Table 8:** Phase Information

**Tabela 8:** Podatki o fazi

Phase Name**	Stoichiometric formula *	Phase name**	Stoichiometric formula *
Sb <sub>2</sub> Zn <sub>3</sub> _T	$\beta\text{-Sb}_2\text{Zn}_3$	CdSb_OME	SbZn
Sb <sub>2</sub> Zn <sub>3</sub> _D	$\alpha\text{-Sb}_2\text{Zn}_3$	Zincblend	AlSb
Sb <sub>3</sub> Zn <sub>4</sub> _G	$\gamma\text{-Sb}_3\text{Zn}_4$	Rhombone	(Sb)
FCC_Al	(Al)	HCP_Zn	(Zn)

\*denotations of stoichiometric formula are taken by Okamoto <sup>19</sup>

**Table 6:** Experimental results from the KEMS method for 0.77Al0.13Sb0.1Zn from 478 K to 566 K

**Tabela 6:** Eksperimentalni rezultati, dobljeni z metodo KEMS za 0.77Al0.13Sb0.1Zn v območju 478–566 K

T/K	1/T	I+(Zn)	p(Zn) /Pa	p(Zn pure)/ Pa	K	a (Zn)	$\gamma_{Zn}$	$G^{xs}_{Zn}/(\text{J/mol})$
478	0.002092	780	5.67E-04	0.000855594	1.52E-09	6.63E-01	6.63	7519
461	0.002169	300	2.13E-04	0.000256755	1.54E-09	8.29E-01	8.29	8106
494	0.002024	1800	1.34E-03	0.002462639	1.51E-09	5.44E-01	5.44	6955
503	0.001988	3450	2.60E-03	0.004333383	1.50E-09	5.99E-01	5.99	7489
505	0.00198	4050	3.06E-03	0.004899798	1.50E-09	6.24E-01	6.24	7688
509	0.001965	4870	3.70E-03	0.006246299	1.49E-09	5.92E-01	5.92	7524
515	0.001942	6400	4.89E-03	0.008927265	1.49E-09	5.48E-01	5.48	7286
534	0.001873	17420	1.36E-02	0.026233813	1.47E-09	5.20E-01	5.20	7318
542	0.001845	22200	1.75E-02	0.040378946	1.46E-09	4.34E-01	4.34	6619
557	0.001795	46400	3.73E-02	0.087665647	1.44E-09	4.25E-01	4.25	6705
intbl566	0.001767	78600	6.38E-02	0.136857484	1.43E-09	4.66E-01	4.66	7244

\*K – Instrumental constant, I – Intensity of zinc

The presented model, using the GSM for the prediction of the extension of AlSb + L two-phase region inside the ternary system also predicts six invariant reactions (**Figure 8**). The calculation of the invariant ternary reaction E1 was made on the assumption that the eutectic reaction ( $L \rightarrow \gamma\text{-Sb}_3\text{Zn}_4 + \beta\text{-Sb}_2\text{Zn}_3$ ) appears at higher temperatures in the Zn-Sb binary system<sup>17,18,19</sup>. A peritectic reaction was also obtained ( $L + \beta\text{-Sb}_2\text{Zn}_3 \rightarrow \gamma\text{-Sb}_3\text{Zn}_4$ ) by other authors<sup>20,21,22</sup>.

#### 4 CONCLUSIONS

The results from the Oelsen Calorimetry show a good agreement with the results from the Chou, Toop and Muggianu models. A positive deviation from the Raoult's law was determined by the obtained activity of aluminium in the Al-Sb0.1Zn0.9 section (**Table 6**). A positive deviation of the zinc activity was also confirmed in the aluminium-rich corner with the sample 0.77Al0.13Sb0.1Zn in an extended temperature range. Using the SGTEv4 we were able to predict the nature of various heterogeneous equilibria in the Al-Sb-Zn system. These thermodynamic data are being published for the first time, to the best of our knowledge.

#### ACKNOWLEDGMENTS

This work is a contribution to the European COST MP0602 Action. The authors are grateful to Mr. Arkadij Popović from IJS for all his help regarding the work than on the KEMS.

#### 5 REFERENCES

- <sup>1</sup>G. Klančnik, P. Mrvar, J. Medved; Phase relations in the Pt-Ag17.5-Si4.5 ternary alloy; *Mater. tehnol.* 44 (2010) 4, 213–217
- <sup>2</sup>K. T. Raić, R. Rudolf, B. Kosec, I. Anžel, V. Lazić, A. Todorović; Dental joining practice and jewellery manufacturing; *Mater. tehnol.* 43 (2009) 1, 3–9

- <sup>3</sup>A. D. Pelton; A general geometric thermodynamic model for multi-component solutions; *Calphad Journal*, 25 (2001) 2, 319–328
- <sup>4</sup>K. M. Kadish, R. S. Ruoff, Fullerenes, recent advances in the chemistry and physics of fullerenes and related materials, The electrochemical society, Inc., Pennington, 1994
- <sup>5</sup>L. Bencze, R. Milačić, R. Jačimović, D. Žigon, L. Matyas, A. Popović, Knudsen effusion mass spectrometric determination of mixing thermodynamics data of liquid Al-Cu-Sn alloy, *International journal of mass spectrometry*, 289 (2010), 11–19
- <sup>6</sup>W. Oelsen, P. Zuhlke; *Arch. Eisenhüttenwess*, 27 (1956), 12, 743
- <sup>7</sup>K. C. Chou, A general solution model for predicting ternary thermodynamic properties, *Calphad*, 19 (1995), 315–325
- <sup>8</sup>G. W. Toop, Predicting ternary activities using binary data, *Trans. AIME*, 233 (1965), 850–855
- <sup>9</sup>Y. M. Muggianu, M. Gambino, J. P. Bros, Enthalpies of formation of liquid alloys, *J. Chim. Phys.*, 72 (1975), 83–88
- <sup>10</sup>Y. Liu, D. Liang; A contribution to the Al-Pb-Zn ternary system; *Journal of Alloys and Compounds*, 403 (2005), 110–117
- <sup>11</sup>T. Balakumar, M. Medraj; Thermodynamic modeling of the Mg-Al-Sb system; *Calphad*, 29 (2005), 24–36
- <sup>12</sup>X. J. Liu, C. P. Wang, I. Ohnuma, R. Kainuma, K. Ishida; Thermodynamic Assessment of the Phase Diagrams of the Phase Diagrams of the Cu-Sb and Sb-Zn Systems, *Journal of Phase Equilibria*, 21 (2000) 5, 432–442
- <sup>13</sup>L. A. Zabdyr; Phase equilibria in ternary Cd-Sb-Zn system; *Calphad*, 21 (1997) 3, 349–358
- <sup>14</sup>K. Niwa, T. Yokokawa, H. Wada; Vapor pressure of Tin-Zinc binary liquid alloy; *Bulletin of the chemical society of Japan*, 33(1960) 10, 1345–1349
- <sup>15</sup>L. C. Prasad, A. Mikula; Effect of temperature on inter-metallic associations in Sb-Zn liquid alloys; *Journal of Alloys and Compounds*, 299 (2000), 175–182
- <sup>16</sup>Z. Zhu, X. Su, F. Yin, J. Wang, C. Wu; Experimental Investigation of the Zn-Al-Sb system at 450 °C; *Journal of Phase equilibria and Diffusion*, 30 (2009) 6, 595–601
- <sup>17</sup>T. B. Massalski; *Binary Alloy phase diagrams*; ASM International, Materials park, (1990), 3320–3321
- <sup>18</sup>G. Vuillard, J. P. Piton; *Compt. Rend*, 263 (1966), 1081–1021
- <sup>19</sup>H. Okamoto, Sb-Zn (Antimony-Zinc); *Journal of Phase Equilibria and Diffusion*, 29 (2008), 3
- <sup>20</sup>T. Takei; *Sci. Rep. Tahoku Imp. Univ*, 16 (1927), 1031–1056
- <sup>21</sup>M. Hansen, K. Anderko; *Constitutional of Binary Alloys*; McGraw-Hill, New York, 1958
- <sup>22</sup>COST Action 531 – Atlas of Phase Diagrams for Lead-Free Soldering, 2008



## XPS AND SEM OF UNPOLISHED AND POLISHED FeS SURFACE

### RENTGENSKA FOTOELEKTRONSKA SPEKTROSKOPIJA IN VRSTIČNA ELEKTRONSKA MIKROSKOPIJA NEPOLIRANE IN POLIRANE POVRŠINE FeS

**Djordje Mandrino**

Institute of Metals and Technology, 1000 Ljubljana, Lepi pot 11, Slovenia  
djordje.mandrino@imt.si

*Prejem rokopisa – received: 2011-04-04; sprejem za objavo – accepted for publication: 2011-07-11*

It was attempted to measure parameters of Fe 2p and S 2p transitions for Fe and S in FeS to compare them with range of values obtainable from the literature. FeS specimen was manufactured from the standard material used for chemical analysis. X-ray Photoelectron spectroscopy (XPS) was first performed on non-polished and then on polished surface. Scanning Electron Microscopy (SEM) was used to image both surfaces. It was found that major constituents of non-polished surfaces are sulphate and sulphite compounds but that composition and structure of the polished surface are also complex and may become increasingly so after cleaning by ion sputtering. At best, composition of the surface approximated FeS very poorly, thus necessitating the use of literature Fe 2p and S 2p parameter values instead of directly measuring improved values.

Keywords: iron sulphide, FeS, XPS, SEM, ion etching, surface active element

Poskusili smo izmeriti parametre prehodov Fe 2p in S 2p za Fe in S v FeS, da bi jih primerjali s širokim razponom vrednosti iz literature. Vzorec FeS za meritve smo izdelali iz standardne kemikalije, ki se uporablja v kemijski analitiki. Z rentgensko fotoelektronsko spektroskopijo smo najprej opravili meritve na nepolirani in potem še na polirani površini vzorca. Z vrstično elektronsko mikroskopijo smo upodobili obe površini. Ugotovili smo, da nepolirano površino v pomembnem delu sestavljajo sulfati in sulfiti, da pa sta tudi sestava in struktura polirane površine kompleksni in da to kompleksnost čiščenje površine z ionskim jedkanjem lahko še poveča. V najboljšem primeru je sestava površine zelo slab približek za FeS, in je bolje še naprej uporabljati literaturne vrednosti za ustrezne parametre za Fe 2p in S 2p namesto direktno izmerjenih na obravnavanem vzorcu.

Ključne besede: železov sulfid, FeS, rentgenska fotoelektronska spektroskopija, vrstična elektronska mikroskopija, XPS, SEM, ionsko jedkanje, površinsko aktivni elementi

## 1 INTRODUCTION

Sulphur and its compounds appear in several of our recent and current research topics. It was found to be present in sulphide form in inclusions or oxide layers on austenitic stainless steels<sup>1-3</sup> or electrical steels<sup>4-6</sup>, in minute quantities as sulphate after electrochemical treatments of metals<sup>2,3,7-10</sup>, and as surface active segregant facilitating surface reconstruction<sup>11</sup>. In most of the above studies surface sensitive techniques have been extensively used<sup>12-20</sup>, X-ray photoelectron spectroscopy (XPS) among them. In literature rather wide ranges of binding energies for characteristic transitions corresponding to S in sulphides, especially in FeS are reported<sup>23,22</sup>. Part of the cause for the reported discrepancies may be in different experimental set-ups with variations in instrumentation and experimental parameters. Therefore an attempt to measure these values on the instrument used for all other XPS measurements in our recent and current studies was considered worthwhile. To this purpose a specimen was manufactured in two different ways from pure FeS used for chemical analysis. While variety of surface compounds was expected for the unpolished specimen the polished surface still did not yield predominantly FeS species corresponding to the

bulk of the specimen. With prolonged ion sputtering it developed a local surface reconstruction, thus hinting at fundamental surface unhomogeneity and at unsuitability of a bulk specimen as an XPS standard.

## 2 EXPERIMENTAL

Area of approximately  $12 \times 9 \text{ mm}^2$  flattened by grinding at the top of a bulk specimen of FeS of approximately 5 mm thickness was investigated by SEM and XPS. This flat area was then polished down to  $1 \mu\text{m}$  and investigations repeated. FeS was standard compound of molecular mass 87.92 (= 55.85(Fe) + 32.07(S)), used for chemical analysis. Unpolished and polished sample were cleaned by ion sputtering using  $\text{Ar}^+$  at 3 keV,  $1 \mu\text{A}$ , over  $4 \times 4 \text{ mm}^2$  area. Estimated sputtering rate at these parameters is of the order of  $1 \text{ nm} / \text{min}$ <sup>23,24</sup>.

SEM imaging as well as XPS of the sample were performed by VG-Scientific Microlab 310F SEM/AES/XPS. For all XPS measurements  $\text{Mg K}\alpha$  radiation at 1253.6 eV with anode voltage  $\times$  emission current = 12.5 kV  $\times$  16 mA = 200 W power was used. Beneficial carbon contamination at 284.8 eV C 1s binding energy (BE) was used to calibrate the binding energy scale. High resolution windows were measured around C 1s Fe 2p and S

2p transitions. Channel widths of 1 and 0.1 eV were used for survey and high resolution measurements. Several consecutive measurements were averaged to improve signal to noise ratio in high resolution measurements. XPS spectra were acquisitioned using Avantage 3.41v data acquisition & data processing software supplied by the SEM/AES/XPS equipment manufacturer. Casa XPS software<sup>25</sup> was also used for post-acquisition data processing.

### 3 RESULTS AND DISCUSSION

In **Figure 1** SEM images of unpolished and polished sample are shown.

Surface of the unpolished sample is heavily corrugated with corrugation amplitude up to several  $\mu\text{m}$  (**Figure 1a**), while surface of the polished sample is much smoother with maximum corrugation amplitudes below 1  $\mu\text{m}$  (**Figure 1b**), which is consistent with the type of polishing applied.

Facet-like structure on the part of the surface visible in **Figure 2** but not in **Figure 1** suggests that surface reconstruction due to the ion etching and/or surface active element may have occurred. The fact that it only affects part of the surface may be due to the inhomogeneity of the surface

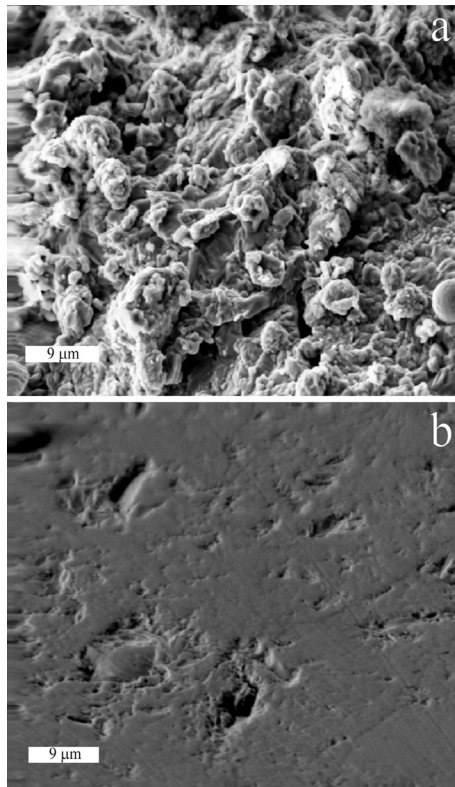


**Figure 1:** SEM images of unpolished (a) and polished (b) FeS specimen

**Slika 1:** Površina nepoliranega (a) in poliranega (b) vzorca FeS upodobljena z vrstično elektronsko mikroskopijo

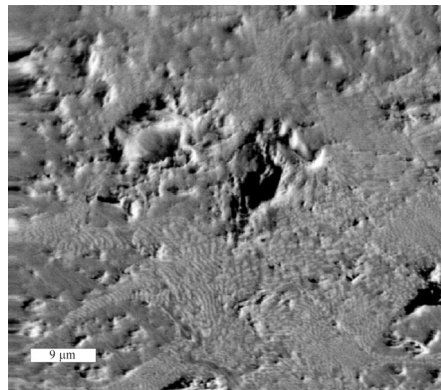


**Figure 2:** SEM image of polished specimen after 8100 s of sputtering  
**Slika 2:** Površina poliranega vzorca po 8100 s ionskega jedkanja upodobljena z vrstično elektronsko mikroskopijo

In **Figure 3** high resolution XPS scans around S 2p, Fe 2p<sub>3/2</sub> and O 1s on unpolished and polished surface after 300 s of sputtering are shown. Different components corresponding to different chemical states of S, Fe and O were used in fitting. They are listed in **Table 1**.

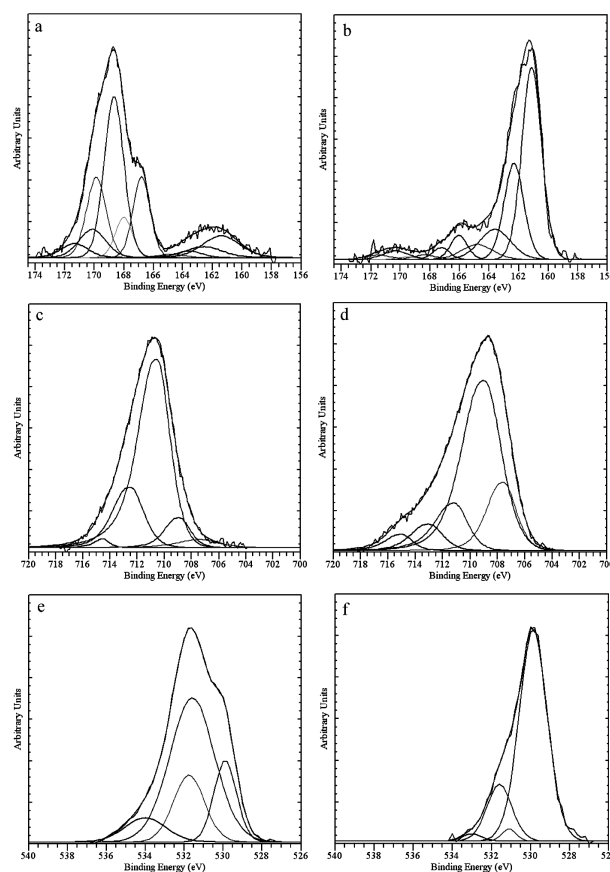


**Figure 3:** High resolution XPS scans around S 2p (a, b), Fe 2p<sub>3/2</sub> (c, d) and O 1s (e, f) on unpolished (a, c, e) and polished (b, d, f) surface after 300 s of sputtering

**Slika 3:** Visokoločljive meritve z rentgensko fotoelektronsko spektroskopijo okoli 2p (a, b), Fe 2p<sub>3/2</sub> (c, d) in O 1s (e, f) na nepoliranem (a, c, e) in poliranem (b, d, f) vzorcu po 300 s ionskega jedkanja

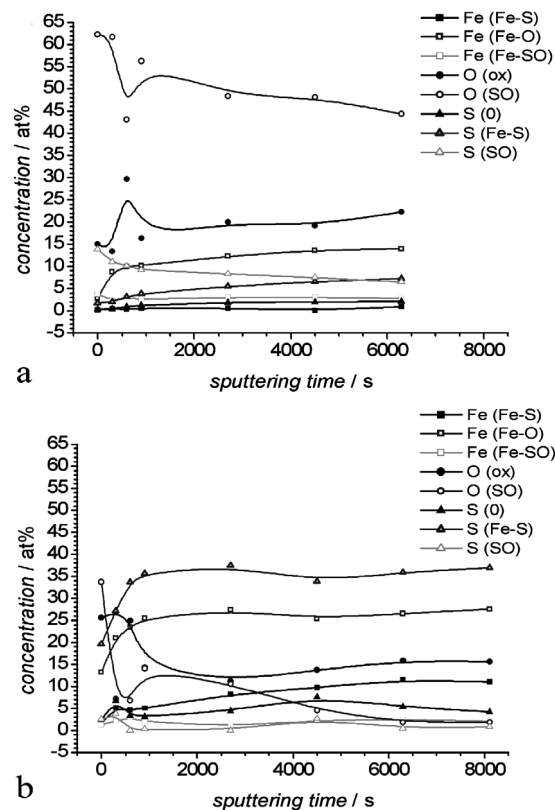
**Table 1:** S 2p, Fe 2p<sub>3/2</sub> and O 1s components used in fitting High resolution XPS scans shown in **Figure 3****Tabela 1:** Komponente S 2p, Fe 2p<sub>3/2</sub> in O 1s, ki smo jih uporabili pri fitanju meritev iz **Slike 3**

component	BE / eV	FWHM / eV
S (S <sup>0</sup> ) 2p <sub>3/2</sub>	163.6 ± 0.2	2.5 ± 0.2
S (S <sup>0</sup> ) 2p <sub>1/2</sub>	164.8 ± 0.2	2.5 ± 0.2
S (S <sup>2-</sup> ) 2p <sub>3/2</sub>	161.1 ± 0.2	1.6 ± 0.2
S (S <sup>2-</sup> ) 2p <sub>1/2</sub>	162.3 ± 0.2	1.6 ± 0.2
S (SO <sub>3</sub> <sup>2-</sup> ) 2p <sub>3/2</sub>	166.0 ± 0.2	1.3 ± 0.2
S (SO <sub>3</sub> <sup>2-</sup> ) 2p <sub>1/2</sub>	167.2 ± 0.2	1.3 ± 0.2
S (SO <sub>4</sub> <sup>2-</sup> ) 2p <sub>3/2</sub>	168.4 ± 0.2	1.9 ± 0.2
S (SO <sub>4</sub> <sup>2-</sup> ) 2p <sub>1/2</sub>	169.6 ± 0.2	1.9 ± 0.2
S (CHSO) 2p <sub>3/2</sub>	170.3 ± 0.2	2.0 ± 0.2
S (CHSO) 2p <sub>1/2</sub>	171.5 ± 0.2	2.0 ± 0.2
Fe (Fe <sup>3+</sup> ) 2p <sub>3/2</sub>	711.0 ± 0.3	2.0 ± 0.3
Fe (Fe <sup>2+</sup> - S) 2p <sub>3/2</sub>	707.1 ± 0.3	1.7 ± 0.3
Fe (Fe <sup>2+</sup> - O) 2p <sub>3/2</sub>	708.7 ± 0.2	2.9 ± 0.2
Fe (Fe <sup>3+</sup> - SO <sub>4</sub> ) 2p <sub>3/2</sub>	712.7 ± 0.2	2.1 ± 0.3
[Fe (Fe <sup>2+</sup> - O) 2p <sub>3/2</sub> ] <sub>sat</sub>	714.7 ± 0.2	1.7 ± 0.2
O (SO <sub>4</sub> <sup>2-</sup> ) 1s	532.0 ± 0.4	1.5 ± 0.3
O (SO <sub>3</sub> <sup>2-</sup> ) 1s	531.0 ± 0.4	1.4 ± 0.4
O (Fe oxide) 1s	530.0 ± 0.3	1.4 ± 0.2
O (contamination) 1s	533.5 ± 0.3	1.5 ± 0.4

Individual components in **Table 1** as well as their parameters were identified with reference to previous published work of XPS measurements on Fe-S compounds <sup>21,26,27</sup>. It is to be noted that on the average 10 – 20 % larger half-widths of the components compared to references <sup>26–28</sup> are not unexpected, since those XPS spectra were measured using monochromated X-ray source. Significantly larger half-widths (of the order of 50 %) than in references were measured for components corresponding to S (S<sup>0</sup>) i.e. elemental sulphur and Fe (Fe<sup>2+</sup> - O) i.e. iron in iron(II) oxide.

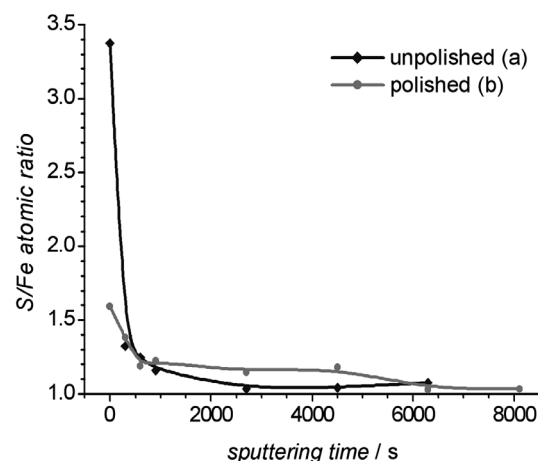
The first may be explained due to components characteristic of elemental sulphur and of polysulphides being very close in their binding energies to the point of virtual overlap, not being resolved into two components <sup>27</sup>. The second is most probably an effect due to preferential sputtering of oxygen compared to iron which causes continuous change in binding energy of iron oxides.

In **Figure 4** results of sputter cleaning onto concentration of different types of surface compounds on the unpolished and polished specimen is shown. These types of compounds are classified as iron oxides, iron – sulphur compounds and sulphur – oxygen compounds. They were arrived at by summing concentrations of corresponding components (e.g. O (SO<sub>3</sub><sup>2-</sup>) 1s and O (SO<sub>4</sub><sup>2-</sup>) 1s for oxygen in sulphur – oxygen compounds). **Figure 4a** shows that majority of the unpolished surface consists of sulphates and sulphites and that their percentage remains significant even after intense cleaning by ion etching (6300 s). Another significant constituent are iron oxides that change even less with sputtering time. Probable reason for this is that 6300s of ion etching roughly corresponds to 0.1 μm of material etched off, in

**Figure 4:** Main types of compounds on the surface during sputter-cleaning of the unpolished (a) and polished (b) specimen**Slika 4:** Glavni tipi spojin na površini nepoliranega (a) in poliranega (b) vzorca med čiščenjem z ionskim jedkanjem

some areas even less due to shading effects of the highly corrugated surface with average corrugation amplitude of the order of several μm (**Figure 1a**).

**Figure 4b** shows that on the polished surface sulphates drop much faster than on the unpolished one, which additionally suggests that much of the highly corrugated surface structure on the unpolished surface

**Figure 5:** S/Fe atomic ratio with sputtering time for unpolished (a) and polished (b) specimen.**Slika 5:** Atomsko razmerje S/Fe v odvisnosti od časa ionskega jedkanja za nepoliran (a) in poliran (b) vzorec

actually consists of sulphates. It can be also seen that there is more Fe and S corresponding to FeS than on the unpolished surface, though far from being the major components, but also lot of iron oxides and some elemental sulphur.

In **Figure 5** S/Fe atomic ratios with sputtering time for unpolished and polished specimen are shown. Initial values are rather high, they, however drop below 1.2 after first sputtering cycle and remains approximately constant in unpolished sample while in polished one it decreases somewhat further and approaches 1 towards end of the sputtering time. Even at this stage, with iron and sulphur atomic ratio close to 1, actual surface stoichiometry is much more complex as can be seen from **Figure 4**.

Real inhomogeneity of the surface, structural as well as compositional is best revealed by facet-like structure that appeared in small area of the polished sample after 8100 s of sputtering (**Figure 2**, compare to the same area in **Figure 1b** before sputtering). This structure is most probably induced by ion etching<sup>14,29–31</sup>, but its appearance may also be enhanced by elemental sulphur acting as surface active element<sup>11,32</sup>. If this is indeed the case, islands of the structural and compositional homogeneity over the surface of the polished and ion etched sample seem to be of the size of the order of micrometers.

#### 4 CONCLUSIONS

Non-polished and polished flat areas on specimens manufactured from FeS were XPS profiled. Both surfaces were imaged by SEM. It was found that major constituents of non-polished surfaces are sulphate and sulphite compounds with slightly increasing iron oxides species concentration during the ion etching. In polished surface there is a fast drop of sulphate and sulphite compounds concentration accompanied by increasing iron oxides species concentration as well as iron sulphide and elemental sulphur concentrations. While S/Fe ratios for both types of specimen may reach approximately or virtually 1 during the ion etching, this is not due to the specimens' surfaces consisting (primarily) of FeS. Comparing SEM images of polished surface before and after profiling a localized facet-like surface reconstruction is revealed that may have been induced by combination of ion beam etching and elemental sulphur as surface active element. Localized nature of this surface reconstruction also suggests high surface unhomogeneity of the specimen. For some types of materials, especially for non-metallic ones, it may be necessary to prepare a useable standard for surface sensitive spectroscopy in a form of a thin film<sup>33–36</sup>.

#### 5 REFERENCES

- <sup>1</sup> C. Donik, I. Paulin, M. Jenko, *Mater. Tehnol.* 44 (2010), 67–72
- <sup>2</sup> A. Kocijan, M. Conradi, *Mater. Tehnol.* 44 (2010), 21–24
- <sup>3</sup> A. Kocijan, D. K. Merl, M. Jenko, *Corrosion Science* 53 (2011), 776–783
- <sup>4</sup> M. Godec, M. Jenko, H. J. Grabke, R. Mast, *Isij International* 39 (1999), 742–746
- <sup>5</sup> D. S. Petrovic, M. Jenko, *Vacuum* 71 (2003), 33–40
- <sup>6</sup> M. Jenko, F. Vodopivec, H. J. Grabke, H. Viefhaus, B. Pracek, M. Lucas, M. Godec, *Steel Research* 65 (1994), 500–504
- <sup>7</sup> M. Torkar, M. Godec, M. Lamut, *Engineering Failure Analysis* 16 (2009), 176–181
- <sup>8</sup> D. A. Skobir, M. Godec, M. Balcar, M. Jenko, *Vacuum* 84 (2009), 205–208
- <sup>9</sup> A. Kocijan, I. Milosev, B. Pihlar, *Journal of Materials Science-Materials in Medicine* 15 (2004), 643–650
- <sup>10</sup> A. Kocijan, C. Donik, M. Jenko, *Corrosion Science* 49 (2007), 2083–2098
- <sup>11</sup> M. Jenko, D. Mandrino, M. Milun, *Metalurgija* 41 (2002), 191–197
- <sup>12</sup> M. Godec, B. Sustarsic, M. Jenko, *Metalurgija* 47 (2008), 9–12
- <sup>13</sup> D. A. Skobir, M. Godec, M. Jenko, B. Markoli, *Surface and Interface Analysis* 40 (2008), 513–517
- <sup>14</sup> B. S. Batic, M. Jenko, *Surface and Interface Analysis* 42 (2010), 703–706
- <sup>15</sup> D. A. Skobir, F. Vodopivec, S. Spaic, B. Markoli, *Zeitschrift Fur Metallkunde* 95 (2004), 1020–1024
- <sup>16</sup> D. A. Skobir, F. Vodopivec, L. Kosec, M. Jenko, *J. Vojvodic-Tuma, Steel Research International* 75 (2004), 196–203
- <sup>17</sup> D. A. Skobir, M. Godec, A. Nagode, M. Jenko, *Surface and Interface Analysis* 42 (2010), 717–721
- <sup>18</sup> T. V. Pirtovsek, G. Kugler, M. Godec, M. Tercej, *Materials Characterization* 62 (2011), 189–197
- <sup>19</sup> D. Jenko, A. Bencan, B. Malic, J. Holc, M. Kosec, *Microscopy and Microanalysis* 11 (2005), 572–580
- <sup>20</sup> J. Tellier, B. Malic, B. Dkhil, D. Jenko, J. Cilensek, M. Kosec, *Solid State Sciences* 11 (2009), 320–324
- <sup>21</sup> C. D. Wagner, A. V. Naumkin, A. Kraut-Vass, J. W. Allison, C. J. Powell, J. R. Rumble (eds.), *NIST X-ray Photoelectron Spectroscopy Database*. <http://srdata.nist.gov/xps>
- <sup>22</sup> J. Chastain (ed.) *Handbook of X-ray photoelectron spectroscopy*, Physical electronics, Eden Prairie 1995
- <sup>23</sup> C. Donik, A. Kocijan, I. Paulin, M. Jenko, *Mater. Tehnol.* 43 (2009), 137–142
- <sup>24</sup> C. Donik, A. Kocijan, J. T. Grant, M. Jenko, A. Drenik, B. Pihlar, *Corrosion Science* 51 (2009), 827–832
- <sup>25</sup> N. Fairley, <http://www.casaxps.com/>
- <sup>26</sup> J. E. Thomas, W. M. Skinner, R. S. C. Smart, *Geochimica Et Cosmochimica Acta* 67 (2003), 831–843
- <sup>27</sup> M. Mullet, S. Boursiquot, J. J. Ehrhardt, *Colloids and Surfaces a-Physicochemical and Engineering Aspects* 244 (2004), 77–85
- <sup>28</sup> Y. F. Cai, Y. G. Pan, J. Y. Xue, Q. F. Sun, G. Z. Su, X. Li, *Applied Surface Science* 255 (2009), 8750–8760
- <sup>29</sup> A. Toma, B. S. Batic, D. Chiappe, C. Boragno, U. Valbusa, M. Godec, M. Jenko, F. B. de Mongeot, *Journal of Applied Physics* 104 (2008), 104313
- <sup>30</sup> A. Toma, D. Chiappe, B. S. Batic, M. Godec, M. Jenko, F. B. de Mongeot, *Physical Review B* 78 (2008), 153406
- <sup>31</sup> B. S. Batic, M. Jenko, *Journal of Vacuum Science & Technology A* 28 (2010), 741–744
- <sup>32</sup> E. A. González, P. V. Jasen, M. Sandoval, P. Bechthold, A. Juan, B. S. Batic, M. Jenko, *Applied Surface Science* 257 (2011), 6878–6883
- <sup>33</sup> W. Lisowski, A. H. J. van den Berg, D. Leonard, H. J. Mathieu, *Surface and Interface Analysis* 29 (2000), 292–297
- <sup>34</sup> M. Kosec, D. Murko, J. Holc, B. Malič, M. Čeh, T. Hauke, H. Beige, *Zeitschrift für Metallkunde* 92 (2001), 8
- <sup>35</sup> H. Ursic, A. Bencan, M. Skarabot, M. Godec, M. Kosec, *Journal of Applied Physics* 107 (2010), 033705
- <sup>36</sup> Guo-zheng Ma, Bin-Shi Xu, Hai-dou Wang, Hong-juan Si, *Applied surface Science* 257 (2010), 1204–1210

## SURFACE CHARACTERIZATION AND PICKLING CHARACTERISTICS OF THE OXIDE SCALE ON DUPLEX STAINLESS STEEL

### POVRŠINSKA KARAKTERIZACIJA IN LASTNOSTI LUŽENJA OKSIDNE PLASTI NA DUPEKSNEM NERJAVNEM JEKLU

Črtomir Donik

Institute of metals and technology, Lepi pot 11, SI-1000 Ljubljana, Slovenia  
crtomir.donik@imt.si

*Prejem rokopisa – received: 2011-05-03; sprejem za objavo – accepted for publication: 2011-07-05*

Mixtures of hydrofluoric ( $\text{HF}_{(\text{aq})}$ ) and nitric acids ( $\text{HNO}_3$ ) used for the pickling of stainless steels to remove thick oxide scale generate waste liquids with a high HF concentration. The oxide formation during production annealing and the subsequent pickling response in mixed acids have been studied. A cost reduction and a procedure optimization can be achieved by the use of the proper concentration of mixed acids and a low pickling temperature. In this work, new mixtures of both with a high pickling efficiency for solutions designed for duplex stainless steel are checked. The experiments were carried with mixtures consisting of mass fractions 0.5–4.0 %  $\text{HF}_{(\text{aq})}$  and 12.5–22.0 %  $\text{HNO}_3$  at room and elevated temperatures. The goal of the presented work was to determine the optimal pickling time with respect to the temperature and the acid mixture concentration.

Keywords: duplex stainless steel, pickling, oxide scale, HF,  $\text{HNO}_3$

Mešanice fluorovodikove in dušikove(V) kisline z visoko koncentracijo fluorovodikove kisline se uporablja za luženje nerjavnega jekla, ko po žarjenju ostanejo na površini visokotemperaturni oksidi. Raziskovali smo tvorjenje visokotemperaturnih oksidov pri žarjenju in posledično vpliv kislinskih mešanic pri odstranjevanju le-teh. Z optimizacijo postopkov uporabe kislinskih mešanic in procesov, povezanih s tem, ter uporabo najprimernejše mešanice pri najnižji temperaturi lahko zelo zmanjšamo stroške, povezane s končno pripravo nerjavnih jekel. V predstavljenem delu smo preiskovali, kako in katere kislinske mešanice fluorovodikove ( $\text{HF}_{(\text{aq})}$ ) in dušikove(V) kisline ( $\text{HNO}_3$ ) so najugodnejše za luženje dupleksnih nerjavnih jekel. Preiskave smo naredili pri mešanicah 0.5–4.0 %  $\text{HF}_{(\text{aq})}$  in 12.5–22.0 %  $\text{HNO}_3$  pri sobni in povišanih temperaturah. Cilj predstavljenega dela je bila povezava med sestavo oksidne plasti na površini DSS 2205 in hitrostjo odstranjevanja le-te v povezavi s temperaturo in sestavo kislinske mešanice za optimalno dekapirno raztopino.

Ključne besede: dupleksno nerjavno jeklo, luženje, oksidna plast, HF,  $\text{HNO}_3$

## 1 INTRODUCTION

Stainless steels are widely used materials and they have many different applications.<sup>1–9</sup> Duplex stainless steels with a ferrite/austenite volume ratio of about 1:1 have been recognized as good corrosion-resistant materials in various aqueous environments. For this reason, these steels are often exposed to different and relatively aggressive media. Different oxides can be formed on the steel surface and these, often complex, oxides may affect the processing and change the mechanical, chemical and physical properties of the material<sup>10–14</sup>. The alloy selected for this study consisted of the following mass fractions: 22 % chromium, 5–6 % nickel, 3 % molybdenum, 2 % manganese and nitrogen-alloyed duplex stainless steel (DSS 2205). The oxidation and corrosion resistance of the stainless steel have already been the subject of several studies<sup>9,13,15–18</sup>. The corrosion resistance of stainless steel is known to be due to a passivation layer of chromium oxide ( $\text{Cr}_2\text{O}_3$ ) on the surface, which acts as a protective layer against corrosion and has low volume diffusion constants for oxygen and metal ions. It was found that the stabilizing effect of molybdenum on the surface of the passive film

enhances the formation of a layer on duplex stainless steel with a higher Cr/Fe ratio.<sup>19–21</sup> A well-prepared surface of stainless steel shows its superiority over other steels in terms of the possibility of self-preservation with a protective oxide layer with an excellent ability of re-oxidation after damage<sup>22–24</sup>.

On the other hand, it was found that the high-temperature oxide layer, which forms during heat treatment or welding, has inferior protective properties due to the rapid growth, and the chromium content in such a layer is lower than in the scale formed during high-temperature soaking.<sup>1</sup> The high-temperature oxide layer lowers the surface quality and increases the non-uniformity of the surface to the corrosion process. Thus, a high quality of pickling is required. Pickling is the procedure of removing the oxide scale formed over steel surface, mostly during soaking and the hot rolling and forming processes that take place in pickling baths. The bath is exhausted when the metal concentration rises up to 5 wt% of the total liquid; however, this value depends on the acid mixture and the steel composition. The pickling rate efficiency decreases progressively and the pickling bath must be substituted with a fresh acid mixture. Thus, fresh acids are added to make up for the HF and  $\text{HNO}_3$

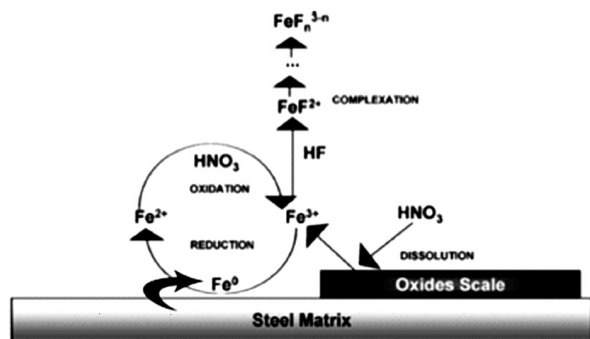


Figure 1: Chemical pickling mechanism proposed by Galvez et al.<sup>33</sup>  
 Slika 1: Mehanizem kemijskega luženja, ki ga predlagal Galvez s sodelavci.<sup>33</sup>

consumed in the pickling process. For this reason, it is important to measure frequently and preserve the optimized individual acidic concentrations of the pickling liquid. For a quantitative analysis of the HF and HNO<sub>3</sub> concentrations in the pickling liquid, the method developed by Galvez et al.<sup>25</sup> is used. This treatment is more efficient than other scale-removing processes, but it generates a great volume of dangerous and toxic wastes: air pollutants (hydrogen fluoride and NO<sub>x</sub>), solid wastes (metal fluorides with descaled chromium oxides) and exhausted pickling liquor are generated<sup>16,25–32</sup>. Nitric(V) acid oxidizes and dissolves the Fe(II)–oxides scale, while hydrofluoric acid is used because of its great reactivity and the stabilizing capacity of metals in solution with complexes formation in the process.

The pickling process is carried out by submerging steel plates in an aqueous solution of hydrofluoric and nitric acids, pickling baths. The scale-dissolution mechanism depends on the oxidation reactions with nitric acid and it is catalyzed by Fe<sup>3+</sup>, as shown in the simplified reaction scheme (Figure 1).<sup>33</sup>

The aim of the present work was to investigate the thick high-temperature oxides on the steel DSS 2205 in order to determine the acid mixture for descaling. For the analysis of the scale, energy-dispersive x-ray spectroscopy (EDS) was used.

## 2 MATERIALS AND METHODS

The DSS 2205 with the composition shown in Table 1 was obtained from the steel plant Acroni. The chemical analyses were performed using an ICP-AES Perkin Elmer 3300. Before annealing, the stainless-steel slab was soaked at 1200 °C for 3 h, hot-rolled to plates of thickness of 28 mm, and annealed at 1100 °C for 2 min to obtain the certified microstructure. The specimens

were used as received from the steel plant, where these were cut out from plates and already sandblasted. The test specimens were cut into squares of 25 × 25 mm, sunk in pickling solutions with different concentrations of HF and HNO<sub>3</sub> for different times at room and elevated temperatures up to 60 °C. All the as-prepared samples were analyzed by FE-SEM JEOL JSM 6500 F SEM/EDS/WDS. The SEM was operated at primary beam energies of 15 and 5 keV in the EDS mode, corresponding to probing depths of approximately 0.8–1.5 μm and 0.25–0.5 μm in layers with predominantly the Fe/Cr/Ni/Mn-oxide composition. In samples of layer thickness well below 1 μm, the average layer density decreased considerably, due to the oxide nature of the layer. A lower primary beam energy was used because it produced better compositional information from the layer only. All the chemicals used were p.a. quality from Merck, Darmstadt, Germany.

## 3 RESULTS

Secondary-electron image of the cross-section of the oxide scale on the DSS 2205 is shown in Figure 2. The scale is not homogeneous and has many cracks that offer the possibility of penetration of the pickling solution to the interface scale/metal to accelerate the pickling process. The figure also shows the rugosity of the interface oxide layer/metal in the range of 10 μm to 20 μm. The scale has on the same areas a clear two-phase microstructure, as shown in the backscattered-electron image in Figure 3. A careful observation shows that the white phase is equal to the base metal and this suggests

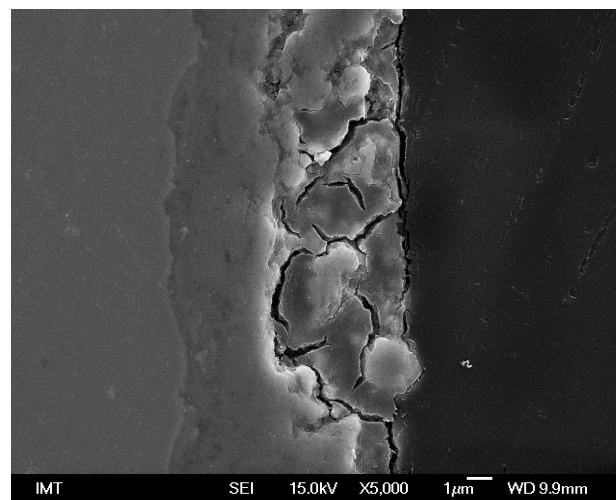
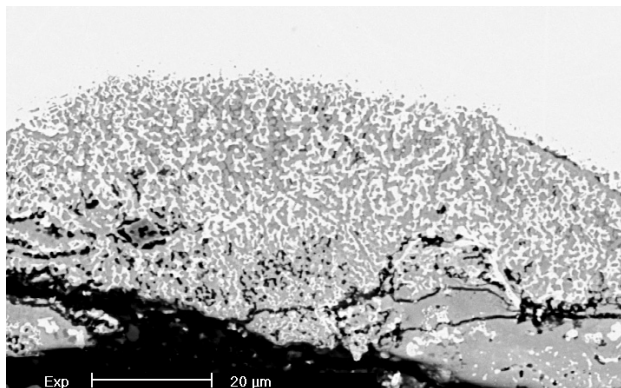


Figure 2: SEM image of cross-section of the oxide scale on DSS 2205  
 Slika 2: SEM slika prečnega preza oksidne plasti na DSS 2205

Table 1: Chemical composition of the duplex stainless steel in mass fractions w/%

Tabela 1: Kemijska sestava preiskovanega dupleksnega jekla v masnih deležih w/%

	Cr	Ni	Mn	Si	P	S	C	Mo	N	Fe
w/%	22.52	5.14	1.47	0.43	0.032	0.001	0.029	3.17	0.17	balance



**Figure 3:** BE image of cross-section of oxide scale on DSS 2205  
**Slika 3:** BE slika prečnega prereza oksidne plasti na DSS 2205

that the gray phase is oxidized metal, very probably it is mostly chromium oxide. In areas with less or without white inserts the content of iron is probably higher. This conclusion is made by the high Gibbs energy of formation for the  $\text{Cr}_2\text{O}_3$ , while it is much lower for oxides like  $\text{FeO}$ ,  $\text{Fe}_2\text{O}_3$  and  $\text{Fe}_3\text{O}_4$  and still lower than for  $\text{NiO}$ , which are presented on Ellingham-Richardson diagram.<sup>1</sup> **Figure 4** shows the EDS mapping, which shows the distribution of elements on the cross-section of the scale. The distribution of oxygen is shown on the second-top image. As expected, oxygen is found only in the oxide layer. The third-top image shows the chromium distribution with an increased chromium concentration in the thin layer in the contact with the metal matrix. In this layer, chromium is enriched; iron and nickel are depleted at the metal of the interface

In the top layer of the oxide scale the chromium content is, as shown later, very similar to the content of chromium in the steel. The lower content of chromium may increase the scale solubility in the pickling solution. It also indicates that the difference in the Gibbs free energy of formation for chromium and iron oxides is efficient and stronger in internal parts of the scale, where the effect of the diffusion of the oxygen is lower. This explanation is confirmed by the image Fe K, which shows the distribution of iron in the scale with a higher content of iron on the upper part and a gradual decrease of iron towards the steel surface and the increase of chromium content in the opposite direction. This demonstrates the competition of these two elements in forming the oxides inside the oxide layers, which is due to the difference in the Gibbs free energies<sup>1</sup>. The last two images of nickel and manganese show the distribution of these elements and no particular pattern is shown. An increase in the manganese content is found in the intermediate layer between the metal and the oxide, probably due to its diffusion characteristics.

**Figures 5** and **6** show the pretreated surface with sandblasting just before the stainless-steel sheets were placed in the pickling baths. Sandblasting in the Acroni steel plant is used to reduce the time and consumption of

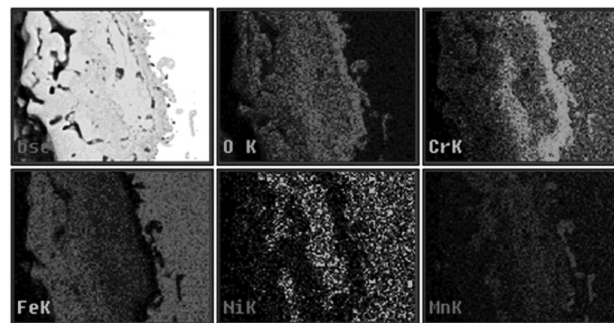


**Figure 4:** BE image with additional EDS mapping (O, Cr, Fe, Ni and Mn) of the scale on the DSS 2205

**Slika 4:** BE slika z EDS površinsko porazdelitvijo elementov (O, Cr, Fe, Ni in Mn) na prečnem prerezu oksidne plasti na DSS 2205

acid pickling solutions. **Figure 5** shows the aim of sandblasting of the surface – the formation of the cracks that are marked in **Figure 5**, the complex oxide scale on stainless steels consisting of  $\text{Fe}_2\text{O}_3$ ,  $\text{Fe}_3\text{O}_4$ ,  $\text{FeCr}_2\text{O}_4$ ,  $\text{Cr}_2\text{O}_3$ ,  $\text{CrO}_3$ ,  $\text{FeCrO}_3$  and  $\text{MnO}_2$ , as confirmed in our previous work<sup>34–37</sup> and allowing a faster reaction of the acid mixture with the oxides in the scale and more importantly, the acid mixture penetrates between the scale and the steel surface, making possible a rapid dissolution of a thin layer of steel that separates the un-dissolved scale from the metal. **Figure 5** also confirms, as reported by Riquier<sup>17,38</sup>, that if the DSS 2205 is normally cooled down, the top layer of duplex stainless steel consists of more austenite grains than the matrix material where the ratio of austenite to ferrite is 1:1. Its presence shows that the share of oxidation of the chromium is greater than that of iron, as expected from the difference of the Gibbs free energy for the formation of the oxides of both metals. This layer has to be removed with the pickling process to gain the certified properties of DSS 2205.

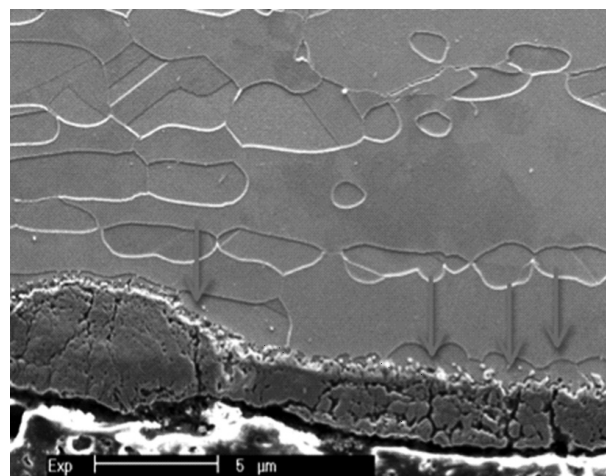


**Figure 5:** SEM image of cross-section of oxide scale on DSS 2205 after sandblasting

**Slika 5:** SEM slika prečnega prereza oksidne plasti na DSS 2205 po peskanju

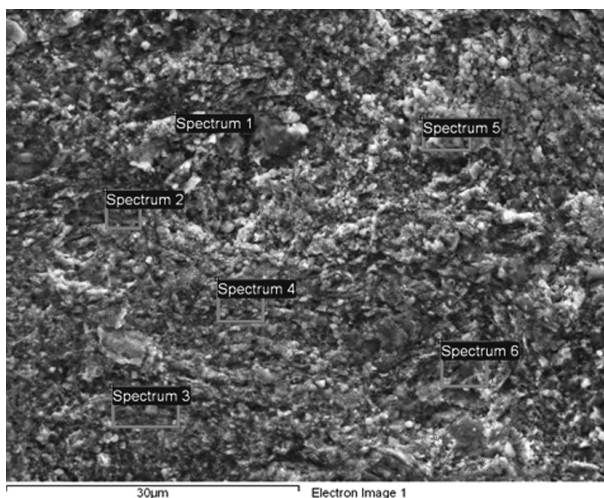


**Figure 6:** SE image of the sandblasted surface of as-received sample  
**Slika 6:** SE slika peskane površine prejetega vzorca

**Figure 6** shows a sandblasted surface of DSS 2205 just before the stainless-steel sheets were placed in the pickling baths to decrease the pickling time and the consumption of the pickling solutions. The surface is rough and from the analyzed areas in **Table 2** it is concluded that the top layers were not completely removed since the content of iron is high. From the results in **Table 2** it can be concluded that after sandblasting the remaining scale contains oxygen iron, chromium and nickel in different contents. From the data in **Table 3** it is concluded that with sandblasting approximately the upper half of the scale layer in Figure 5 is removed. From the data in **Table 2** we can also conclude that the increase in manganese up to more than twice is an artifact that was also observed in our previous works.<sup>35,36</sup>

**Table 2:** Content of elements on the sandblasted sample, as received from the steel plant in mass fractions w/%. The areas of the EDS analyses are marked in **Figure 6**.

**Tabela 2:** Vsebnost elementov na površini peskanih vzorcev iz jeklarne po peskanju v masnih deležih w/%. Analizirana področja so označena na **sliki 6**.

Spectrum	O	Si	Ca	Cr	Mn	Fe	Ni	Mo
Spectrum 1	25.19	0.61	0.94	27.13	2.33	37.45	6.35	
Spectrum 2	25.80	0.76		41.57		28.27	2.11	1.49
Spectrum 3	25.59	0.46	0.42	24.61	1.82	43.45	3.65	
Spectrum 4	19.51	0.57	0.52	46.68	1.27	28.34	2.09	1.02
Spectrum 5	28.60	0.50	0.56	38.68	1.94	26.41	3.31	
Spectrum 6	15.72	0.61	0.57	47.21	1.55	31.76	2.58	

Data in **Table 3** show that the removal rate of the high-temperature scale from the DSS 2205 depends on the pickling solution's composition and temperature. From the data in **Table 3** it is concluded that even a slight increase in the pickling temperature shows a large increase in the pickling effect. This is even stronger when the solution is already used and/or the concentration of the acting media is reduced. From **Table 3** it can also be concluded that the acting agent in

**Table 3:** Effect of the temperature and composition of the pickling solution on the removal rate of the scale of DSS 2205

**Tabela 3:** Hitrost odstranjevanja oksidne plasti z jekla DSS 2205 pri različnih temperaturah in sestavah kislinskih mešaníc

HF / g/L	HNO <sub>3</sub> / g/L	25 °C /h	40 °C /h	60 °C /h
40	220	2	0.75	0.5
40	200	2	0.75	0.5
40	175	2	0.75	0.5
40	150	2	0.75	0.5
40	125	2	0.75	0.5
30	220	3	1.25	0.75
30	200	3	1.25	0.75
30	175	3	1.25	0.75
30	150	3	1.25	0.75
30	125	3	1.25	0.75
20	220	5.5	2	1
20	200	5.5	2	1
20	175	5.5	2	1
20	150	5.5	2	1
20	125	5.5	2	1
10	220	15	3.5	1.25
10	200	15	3.5	1.25
10	175	15	3.5	1.25
10	150	15	3.5	1.25
10	125	15	3.5	1.25
5	220	32	5	2.5
5	200	32	5	2.5
5	175	32	5	2.5
5	150	32	5	2.5
5	125	32	5	2.5
2	220	>100	8	3.5
2	200	>100	8	3.5
2	175	>100	8	3.5
2	150	>100	8	3.5
2	125	>100	8	3.5

the pickling of stainless steel is HF, while HNO<sub>3</sub> is important in the processes after the oxide scale removal with the role of passivation of the DSS 2205 surface.

#### 4 CONCLUSIONS

The role of hydrofluoric acid in the pickling of scale from the surface of duplex stainless steel is essential, as it bonds excess Fe<sup>3+</sup>, so forming fluoride complexes.

A continuous layer of scale formed by the soaking and rolling of slabs of duplex stainless steel is present at the surface. The scale consists of an outer layer of mainly iron chromium oxide that is easily spalled, and an inner layer of oxide with a higher content of chromium.

It was found that sandblasting removes the upper scale layer and forms cracks that increase the surface for acid mixture action and makes possible the penetration of the acid mixture into the interface metal oxide that accelerates the separation of the layer of scale from the steel surface. The results obtained in the present investigation confirm the importance of sandblasting and the

proper selection of the pickling solution composition and temperature for steel plants using pickling for high-temperature oxide scale removal.

### Acknowledgements

This work has been supported by the company Acroni Jesenice with the data and the material used for the presented work. The authors also acknowledge Mrs A. Kosmač, Mr J. Triplat and Mrs E. Bricelj for providing the DSS 2205 specimens and data on the pickling solutions. The views expressed in this publication reflect only the views of the authors and Acroni Jesenice is not liable for any use that may be made of the information contained therein.

### 5 REFERENCES

- <sup>1</sup> J. R. Davis, ASM specialty handbook: Stainless Steels, ASM, 1996
- <sup>2</sup> P. Sevc, D. Mandrino, J. Blach, M. Jenko, J. Janovec, *Kovove Materialy-Metallic Materials*, 40 (2002), 35–44
- <sup>3</sup> M. Godec, A. Kocijan, D. Dolinar, D. Mandrino, M. Jenko, V. Antolic, *Biomedical Materials*, 5 (2010), Sp. iss., doi: 10.1088/1748-6041/5/4/045012
- <sup>4</sup> D. Mandrino, M. Lamut, M. Godec, M. Torkar, M. Jenko, *Surface and Interface Analysis* 39 (2007), 438–444
- <sup>5</sup> D. Mandrino, M. Godec, A. Kocijan, M. Lamut, M. Torkar, M. Jenko, *Metalurgija*, 47 (2008), 119–123
- <sup>6</sup> M. Torkar, D. Mandrino, M. Lamut, *Materiali in Tehnologije*, 42 (2008), 39–43
- <sup>7</sup> A. Kocijan, I. Milosev, B. Pihlar, *Journal of Materials Science-Materials in Medicine*, 14 (2003), 69–77
- <sup>8</sup> A. Kocijan, M. Conradi, *Materiali in Tehnologije*, 44 (2010), 21–24
- <sup>9</sup> A. Kocijan, D. K. Merl, M. Jenko, *Corrosion Science*, 53 (2011), 776–783
- <sup>10</sup> G. D. S. A. Cigada, A. M. Gatti, A. Roos, D. Zaffe, *Journal of Applied Biomaterials*, 4 (1993), 39–46
- <sup>11</sup> M. Gojic, D. Marijan, L. Kosec, *Corrosion*, 56 (2000), 839–848
- <sup>12</sup> A. Kocijan, I. Milosev, D. K. Merl, B. Pihlar, *Journal of Applied Electrochemistry*, 34 (2004), 517–524
- <sup>13</sup> A. Kocijan, I. Milosev, B. Pihlar, *Journal of Materials Science-Materials in Medicine*, 15 (2004), 643–650
- <sup>14</sup> L. Milosev, V. Antolic, A. Minovic, A. Cor, S. Herman, V. Pavlovic, P. Campbell, *Journal of Bone and Joint Surgery-British Volume*, 82B (2000), 352–357
- <sup>15</sup> P. Jian, L. Jian, H. Bing, G. Y. Xie, *Journal of Power Sources*, 158 (2006), 354–360
- <sup>16</sup> L. F. Li, J. P. Celis, *Canadian Metallurgical Quarterly*, 42 (2003), 365–376
- <sup>17</sup> L. F. Li, Z. H. Jiang, Y. Riquier, *Corrosion Science*, 47 (2005), 57–68
- <sup>18</sup> D. Mandrino, M. Jenko, *Vacuum*, 61 (2001), 157–161
- <sup>19</sup> C. M. Abreu, M. J. Cristóbal, R. Losada, X. R. Nóvoa, G. Pena, M. C. Pérez, *Electrochimica Acta*, 49 (2004), 3049–3056
- <sup>20</sup> C. M. Abreu, M. J. Cristobal, X. R. Novoa, G. Pena, M. C. Perez, *Surface and Interface Analysis*, 40 (2008), 294–298
- <sup>21</sup> M. Jenko, D. Mandrino, M. Milun, *Metalurgija*, 41 (2002), 191–197
- <sup>22</sup> M. Jenko, D. Mandrino, M. Godec, J. T. Grant, V. Leskovsek, *Materiali in Tehnologije*, 42 (2008), 251–255
- <sup>23</sup> M. Ristic, S. Music, M. Godec, *Journal of Alloys and Compounds*, 417 (2006), 292–299
- <sup>24</sup> A. Minovic, I. Milosev, V. Pisot, A. Cor, V. Antolic, *Journal of Bone and Joint Surgery-British Volume*, 83B (2001), 1182–1190
- <sup>25</sup> J. L. Galvez, J. Dufour, C. Negro, F. Lopez-Mateos, *Isij International*, 46 (2006), 281–286
- <sup>26</sup> B. S. Covino, T. J. Driscoll, J. P. Carter, P. M. Fabis, *Journal of Metals*, 37 (1985), A50–A50
- <sup>27</sup> L. A. Fernando, D. R. Zaremski, *Metallurgical Transactions a-Physical Metallurgy and Materials Science*, 19 (1988), 1083–1100
- <sup>28</sup> G. Hubmer, K. Rendl, A. Osterkorn, R. Puntigam, R. Sestak, W. R. Thiele, *Stahl Und Eisen*, 122 (2002), 59–65
- <sup>29</sup> N. Ipek, B. Holm, R. Pettersson, G. Runnsjo, M. Karlsson, *Materials and Corrosion-Werkstoffe Und Korrosion*, 56 (2005), 521–532
- <sup>30</sup> W. F. Kladnig, *International Journal of Materials & Product Technology*, 19 (2003), 550–561
- <sup>31</sup> L. F. Li, C. Peter, J. P. Celis, *Corrosion Science*, 50 (2008), 804–810
- <sup>32</sup> L. Narvaez, E. Cano, D. M. Bastidas, P. P. Gomez, *Revista de Metalurgija* (2005), 417–422
- <sup>33</sup> J. L. Galvez, J. Dufour, C. Negro, F. Lopez-Mateos, *Journal of Hazardous Materials*, 154 (2008), 135–145
- <sup>34</sup> Č. Donik, A. Kocijan, J. T. Grant, M. Jenko, A. Drenik, B. Pihlar, *Corrosion Science*, 51 (2009), 827–832
- <sup>35</sup> Č. Donik, A. Kocijan, D. Mandrino, I. Paulin, M. Jenko, B. Pihlar, *Applied Surface Science*, 255 (2009), 7056–7061
- <sup>36</sup> Č. Donik, A. Kocijan, I. Paulin, M. Jenko, *Materiali in Tehnologije*, 43 (2009), 137–142
- <sup>37</sup> Č. Donik, D. Mandrino, M. Jenko, *Vacuum*, 84 (2010), 1266–1269
- <sup>38</sup> Y. Riquier, H. Zhang, *Revue De Metallurgie-Cahiers D Informations Techniques*, 101 (2004), 855–865



## CFD ANALYSIS OF EXOTHERMIC REACTIONS IN Al-Au NANO MULTI-LAYERED FOILS

### CFD-ANALIZA EKSOTERMNIH REAKCIJ V VEČPLASTNIH NANOFOLIJAH Al-Au

**Karlo T. Raić<sup>1</sup>, Rebeka Rudolf<sup>2,3</sup>, Primož Ternik<sup>4</sup>, Zoran Žunič<sup>5</sup>, Vojkan Lazić<sup>6</sup>,  
Dragoslav Stamenković<sup>6</sup>, Tatjana Tanasković<sup>7</sup>, Ivan Anžel<sup>2</sup>**

<sup>1</sup>University of Belgrade, Faculty of Technology and Metallurgy, Karnegijeva 4, Belgrade, Serbia

<sup>2</sup>University of Maribor, Faculty of Mechanical Engineering, Maribor, Slovenia

<sup>3</sup>Zlatarna Celje, d. d., Kersnikova ul.19, 3000 Celje, Slovenia

<sup>4</sup>Private Researcher, Bresterniška ulica 163, 2354 Bresternica, Slovenia

<sup>5</sup>AVL-AST, Trg Leona Štuklja 5, 2000 Maribor, Slovenia

<sup>6</sup>University of Belgrade, School of Dentistry, Clinic for Prosthodontics, Belgrade, Serbia

<sup>7</sup>College of Vocational Studies-Belgrade Polytechnics, Belgrade, Serbia  
karlo@tmf.bg.ac.rs

*Prejem rokopisa – received: 2011-02-18; sprejem za objavo – accepted for publication: 2011-03-07*

This work presents the possibility of numerical modelling using Computational Fluid Dynamics (CFD) in the field of nano-foils. The governing equations were solved using a Finite Volume Methodology (FVM). The computational domain was discretized using a uniform Cartesian grid with the appropriate mesh size along the  $x$  and  $y$  directions employing the corresponding number of grid points. The field variables were discretized at the cell centres and the spatial, as well as the time, derivatives were approximated using the second-order accurate numerical scheme. The time-evolution of the temperature and concentration fields, as well as the atomic diffusion coefficient, will be presented for the appropriate Al-Au nano-foil geometry and boundary conditions.

Key words: Au-Al nano-foils, finite volume method, temperature and concentration transfer

V delu je predstavljena možnost numeričnega modeliranja z uporabo računske dinamike fluidov (CFDC) v primeru nanofolij. Ustrezne enačbe so bile rešene z uporabo metodologije končnih prostornin (FVM). Področje izračunov je bilo opredeljeno z uporabo enakomerne kartezijske mreže s primerno velikostjo vzdolž smeri  $x$  in  $y$  z ustreznim številom mrežnih točk. Spremenljivke polj so bile opredeljene za središče celic in prostorske ter časovne derivate ter aproksimirane z uporabo numerične sheme z drugim redom velikosti natančnosti. Časovni razvoj temperaturnih in koncentracijskih polj in koeficient atomske difuzije sta predstavljena za ustrezno geometrijo Al-Au-nanofolij in mejne pogoje.

Ključne besede: Al-Au nanofolije, metoda končnih elementov, prenos temperature in koncentracije

## 1 INTRODUCTION

Combustion synthesis, also called reaction synthesis, is a process in which two or more materials with large exothermic heats of mixing, known as reactants, are combined together. When the reactants are heated sufficiently, they begin to spontaneously intermix on the atomic scale, releasing heat in the process. A large body of literature exists on this process, and it has been reviewed extensively.<sup>1</sup>

In general, combustion synthesis has been accomplished using mixed reactant powders that are pressed into a pellet of a certain green density. The combustion is initiated by an external energy source to heat the compact. Once combustion begins, the energy released by intermixing contributes to an increase of the local temperature, resulting in faster intermixing and combustion. A large amount of materials are reported to have been synthesized with this general method, including carbides, borides, silicides, nitrides, sulfides, hydrides, intermetallics, and complex composites. Combustion synthesis has many advantages, such as the ability to create high-melting-temperature materials in a low-temperature

process, near-net-form fabrication, and rapid material synthesis.

The ignition of combustion synthesis can be subdivided into two different modes. The first mode, important for present research, is termed self-propagating high-temperature synthesis, or SHS. In this method, the compact is heated locally using an external heat source. The local heating initiates the reaction locally, releasing heat that drives the reaction forward. The reaction moves across the compact in a self-propagating manner, driven by its own heat. The other method of ignition is termed thermal explosion, or simultaneous ignition.

However, powder compacts have several limitations when used for combustion synthesis. The density of the final product is often limited by the green density of the powder compact. If the combustion synthesis reaction is solid state, the particles can only inter diffuse with each other where they are in physical contact. The size of the powder particles is often large compared to the characteristic diffusion distance for a given system, making it difficult to achieve full intermixing. Particles of highly reactive components will often have a passivating outer

coating that acts as a barrier to the diffusion with other reactants. Moreover, voids between the powder particles limit thermal diffusion through the compact, reducing the ability of the reaction to be driven by its own heat.

With modern thin-film deposition techniques, fully dense multilayer materials with similar exothermic reactions can be fabricated (**Figure 1**). Such reactive multilayer foils consist of hundreds or thousands of nanometer-scale alternating layers of two or more materials, known as reactants, which can mix exothermically. When heat is applied locally to the foil, it undergoes SHS in a fashion similar to powder compacts. Structures of reactive multilayer foils offer several potential improvements over powder compacts.

The individual layers in a reactive foil are usually on the scale of tens of nanometers, which significantly decreases the diffusion distances involved in interatomic diffusion between the reactants. The thickness of the individual reactant layers can be controlled during fabrication, allowing significant control over the properties of the foil. The individual layers are in intimate contact with each other, which increases both thermal and atomic diffusion in the system while also eliminating voids in the system. Moreover, having thin layers of reactants that are in intimate contact with each other makes the SHS reaction propagate faster in most reactive foils than in a powder compact with the same components.

In an A-B multilayer system (here Al-Au), when one end of the foil is ignited with a small thermal pulse (such as a spark) at room temperature, local atoms will diffuse normal to the layers with A-A and B-B bonds being exchanged for A-B bonds, as shown in **Figure 1**.

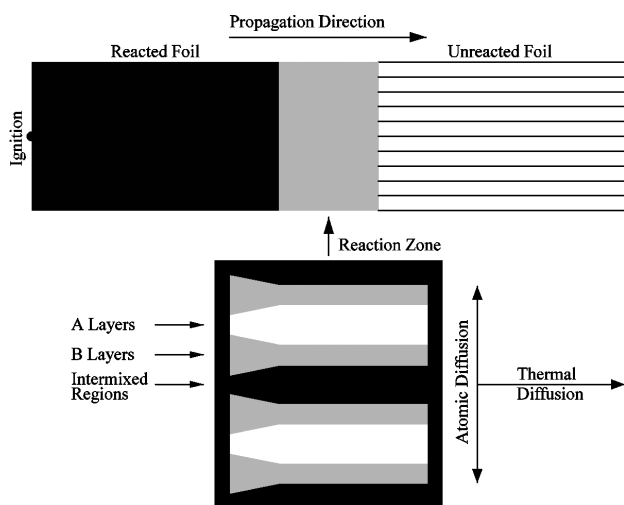


**Figure 1:** Schematic representation of a self-propagating reaction in a multilayer foil that is propagating from left to right. The unreacted foil consists of alternating layers of elements A and B with an intermixed region between the layers.

**Slika 1:** Shematična slika samonapredujuće reakcije z leve na desno v večplastni foliji. Nezreagirana folija je iz izmeničnih plasti elementov A in B s področjem mešanja med plastmi.

In this process, the heat is released and conducted parallel to the layers. If the atomic diffusion and energy release are sufficiently fast, then the reactions are self-propagating. These reactions can travel as fast as 25 m/s and can reach temperatures above 1500 °C.

Numerous studies of interface reactions have been performed in different multilayer systems. A common feature of these multilayers is the apparently large free energy, typically several tens of kJ/mol, available for the phase formation. This leads us to conclude that all possible product phases should be able to form from the very beginning of the reaction.

The aim of the present work is to support the development of novel reactive Au-Al nano-multilayered material that enables the rapid bonding of similar and dissimilar materials by using a Computational Fluid Dynamics (CFD) analysis. The advantage of numerical modelling is that, once the model is set up and established, a wide range of scenarios can be investigated with relatively little effort, and complex two-dimensional<sup>2</sup> as well as three-dimensional<sup>3</sup> problems may be solved using numerical models. The potential use for the reactive Al-Au nano-foils is as a controllable, localised heat source for joining applications<sup>4,5</sup>. To optimize the performance of the Al-Au foils it is necessary to have a clear understanding of the physical processes that dictate the reaction temperature, the rate of heat generation and the velocity at which the reaction propagates along a foil.

## 2 NUMERICAL MODELLING

The formulation of the mathematical model used to describe the self-propagating reactions in multi-layered Al-Au nano-foil is based on the following assumptions: (1) the effects of phase changes in the foil (e.g., melting of the reactants and/or products) are neglected; (2) the atomic diffusion is represented by a single binary diffusion coefficient  $D$ ; (3) the physical properties of the foil (e.g., density  $\rho$ , thermal conductivity  $\lambda$  and specific heat  $c_p$ ) are assumed to be dependent on the composition. Last but not least, the width of the foil ( $z$ ) is large in comparison to the thickness ( $y$ ) and small in comparison to the length ( $x$ ). As a result, it is possible to treat the thermal and atomic diffusion in the foil as a two-dimensional problem.

### 2.1 Governing equations

Under the assumptions above the atomic mixing is described using a time-dependent, conserved scalar field  $C(x,y,t)$ , defined such that  $C = 1$  for pure Au and  $C = 0$  for pure Al. The evolution of  $C$  is governed by:

$$\frac{\partial C}{\partial t} = \frac{\partial}{\partial x_j} \left( D \frac{\partial C}{\partial x_j} \right) \quad (1)$$

The atomic diffusivity is assumed to be independent of the composition and to follow the Arrhenius dependence on the temperature, according to:

$$D = D_0 \exp\left(-\frac{E}{RT}\right) \quad (2)$$

where  $D_0$  is the Arrhenius pre-exponent,  $E$  is the activation energy and  $R$  is the universal gas constant. The values and  $E = 25.20$  kJ/mol as used in the present study are taken from the work of Fouracre<sup>6</sup>.

The time-evolution of the concentration field is coupled with the temperature equation:

$$\frac{\partial T}{\partial t} = \frac{\partial}{\partial x_j} \left( \frac{\lambda}{\rho c_p} \frac{\partial T}{\partial x_j} \right) + \frac{\partial}{\partial t} \left[ \frac{Q(C)}{\rho c_p} \right] \quad (3)$$

where the physical properties (thermal conductivity  $\lambda$ , density  $\rho$  and specific heat  $c_p$ ) in any control volume of the domain are given by the corresponding fraction of the phase (Au and Al) in that volume. They are mathematically obtained as:

$$\begin{aligned} \lambda &= \lambda_{Au} C + \lambda_{Al} (1-C) \\ \rho &= \rho_{Au} C + \rho_{Al} (1-C) \\ c_p &= c_{p,Au} C + c_{p,Al} (1-C) \end{aligned} \quad (4)$$

The rate at which the heat is generated ( $\partial Q(C)/\partial t$ ) is assumed to be proportional to the rate at which the composition of the foil changes. In the simplest case, the linear relationship between the composition and the energy released can be assumed<sup>7</sup>. However, a parabolic function may be closer to the real situation.<sup>8,9</sup>

$$Q(C) = -\rho c_p (T_{f0} - T_0) C^2 \quad (5)$$

and this was used in the present study.

$T_{f0}$  and  $T_0$  are the adiabatic temperature of the reaction and the initial temperature of the foil.

## 2.2 Geometry, boundary and initial conditions

The laminar and time-dependent thermal and species transport in a two-dimensional nano-foil was considered as depicted in **Figure 2**.

At the inlet we prescribed the constant temperature  $T = 1000$  K, while the convective heat flux condition (for natural convection along the vertical plate) was used at

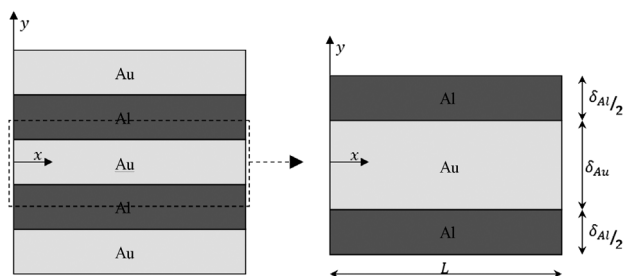


**Figure 2:** Schematic of multi-layered Au-Al nano-foil.  $L = 2000$  nm,  $\delta_{Au} = \delta_{Al} = 100$  nm

**Slika 2:** Shema večplastne Au-Al nanofolije.  $L = 2000$  nm,  $\delta_{Au} = \delta_{Al} = 100$  nm

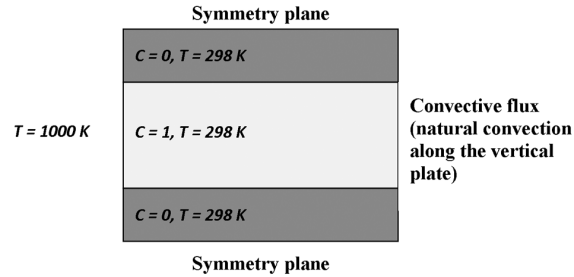


**Figure 3:** Boundary and initial conditions

**Slika 3:** Začetni in mejni pogoji

the outlet of the nano-foil. The initial conditions were as follows:

- Temperature  $T = 298$  K in the whole nano-foil.
- Concentration  $C = 1$  for Au and  $C = 0$  for Al, see **Figure 3**.

For the nano-foil, the following physical properties were used for Au:

- Density  $\rho = 19320$  kg/m<sup>3</sup>
- Specific heat  $c_p = 130$  J/kgK
- Thermal conductivity  $\lambda = 318$  W/mK

and Al:

- Density  $\rho = 2700$  kg/m<sup>3</sup>
- Specific heat  $c_p = 910$  J/kgK
- Thermal conductivity  $\lambda = 237$  W/mK

## 2.3 Numerical procedure

The governing equations were solved using with the Ansys CFX numerical code which employs a standard finite-volume methodology<sup>10</sup> with all the variables defined at the centre of control volumes populating the physical domain being considered. Each equation is integrated over the control volume to obtain a discrete equation which connects the variable at the centre of the volume with its neighbours.

The computational domain was discretized using a uniform Cartesian grid of mesh size  $\Delta x = \Delta y$  along the  $x$  and  $y$  directions, respectively. The corresponding number of grid points is denoted by  $N_x = 800$  and  $N_y = 80$ . For a spatial discretization of diffusive terms, the second-order accurate scheme based on central-differences was used, while temporal derivatives were approximated with a second-order accurate backward differences for a fixed time step  $\Delta t = 10^{-9}$  s.

## 3 RESULTS AND DISCUSSION

The time-evolution of both the temperature and concentration field is presented in **Figure 4**. It can be seen that the temperature (i.e., thermal) transport is essentially unidirectional (mostly taken in the axial direction) and occurs parallel to the layering.

In contrast to other studies<sup>7,8,9,11</sup> where the atomic diffusion was modelled as a one-dimensional pheno-

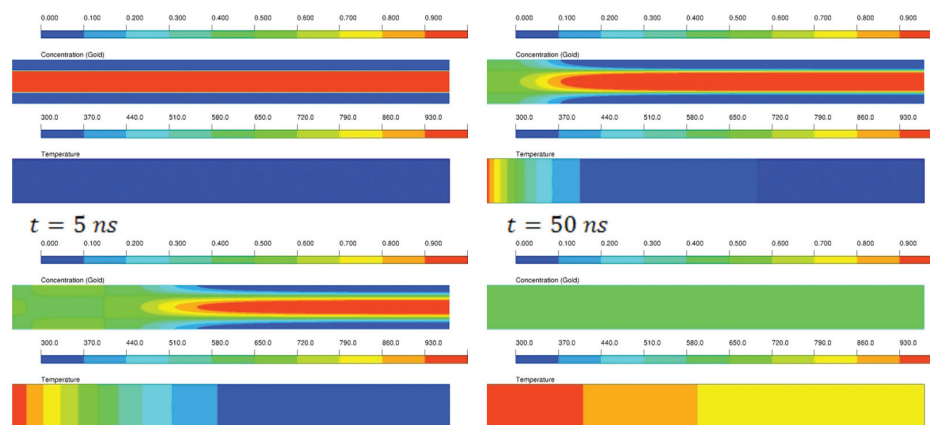


**Figure 4:** Time evolution of the temperature and concentration field  
**Slika 4:** Časovni razvoj temperaturnega in koncentracijskega polja

menon (occurring normal to the layering) the present study shows that the atomic diffusion is actually a two-dimensional phenomenon (see **Figure 4**). This is due to the fact that the diffusion coefficient  $D$ , as defined by Eq. (2), varies with the temperature (as a matter of fact it increases as the temperature increases) in the axial direction. Of course, if the diffusion coefficient is kept constant, the concentration diffusion would occur only in the streamwise direction (due to the concentration gradient).

Finally, in the present study the concentration diffusion is a much faster process due to the higher value of the diffusion coefficient  $D$  in comparison to the value of the thermal diffusion coefficient  $\alpha$ .

#### 4 CONCLUSIONS

In the present study, the time-dependent temperature and concentration diffusion in the multi-layered Al-Au nano-foil was studied numerically using mathematical modelling and a finite-volume-based CFD code. The atomic diffusion coefficient  $D$  was taken to be independent of the composition and to follow the Arrhenius dependence on the temperature while the physical properties (and therefore the thermal diffusion) in any control volume of the domain were taken to be dependent on the corresponding fraction of the phase (Au and Al) in that volume.

The present numerical results show that the temperature diffusion is essentially unidirectional (in the axial direction) while the atomic diffusion occurs in both (i.e., axial and streamwise) directions due to the variable diffusion coefficient and the concentration gradient. The latter is an important fact (influencing the thickness of the intermixed region between layers as well as the heat

release in the process) which has been ignored in most of the existing analytical as well as computational models.

#### 5 REFERENCES

- A. J. Swiston, T. C. Hufnagel, T. P. Weihs, Joining bulk metallic glass using reactive multilayer foils. *Scripta Materialia*, 48 (2003), 1575–1580
- P. Ternik, New contributions on laminar flow of inelastic non-Newtonian fluid in the two-dimensional symmetric expansion: Creeping and slowly moving flow conditions. *Journal of Non-Newtonian Fluid Mechanics*, 165 (2010), 1400–1411
- P. Ternik, J. Marn, Numerical study of blood flow in stenotic artery. *Applied Rheology*, 19 (2009), 13060
- K. T. Raić, R. Rudolf, B. Kosec, I. Anžel, V. Lazić, A. Todorović, Nanofoils for soldering and brazing in dental joining practice and jewellery manufacturing. *Mater. Tehnol.*, 43 (2009), 3–9
- K. T. Raić, R. Rudolf, A. Todorović, D. Stamenković, I. Anžel, Liquid metal-ceramic interfaces in dental practice and jewellery manufacturing. *Mater. Tehnol.*, 44 (2010) 2, 59–66
- R. A. Fouracre, Electron microscope observations of chemical diffusion in the Al/Au system. *Thin Solid Films*, 135 (1986), 189–201
- A. J. Gavens, D. Van Heerden, A. B. Mann, M. E. Reiss, T. P. Weihs, Effect of intermixing on self-propagating exothermic reactions in Al/Ni nanolaminate foils. *Journal of Applied Physics*, 87 (2000), 1255–1263
- A. B. Mann, A. J. Gavens, M. E. Reiss, D. Van Heerden, G. Bao, T. P. Weihs, Modeling and characterizing the propagation velocity of exothermic reactions in multilayer foils. *Journal of Applied Physics*, 82 (1997), 1178–1188
- S. Jayaraman, A. B. Mann, M. Reiss, T. P. Weihs, O. M. Knio, Numerical Study of the Effect of Heat Losses on Self- Propagating Reactions in Multilayer Foils. *Combustion and Flame*, 124 (2001), 178–194
- P. Ternik, Planar sudden symmetric expansion flows and bifurcation phenomena of purely viscous shear-thinning fluids. *Journal of Non-Newtonian Fluid Mechanics*, 157 (2009), 15–25
- E. Bensoin, S. Cerutti, O. M. Knio, T. P. Weihs, Effect of reactant and product melting on self-propagating reactions in multilayer foils. *Journal of Applied Physics*, 92 (2002), 5474–5481

## MICROSTRUCTURE EVOLUTION IN SAF 2507 SUPER DUPLEX STAINLESS STEEL

### RAZVOJ MIKROSTRUKTURE V SUPERDUPLEKSNEM NERJAVNEM JEKLU SAF 2507

**Franc Tehovnik<sup>1</sup>, Boris Arzenšek<sup>1</sup>, Boštjan Arh<sup>1</sup>, Danijela Skobir<sup>1</sup>,  
Boštjan Pirnar<sup>2</sup>, Borut Žužek<sup>1</sup>**

<sup>1</sup>Institute of Metals and Technology, Lepi pot 11, 1000 Ljubljana, Slovenia

<sup>2</sup>Acroni, d. o. o., Kidričeva 44, 4270 Jesenice, Slovenia  
franc.tehovnik@imt.si

*Prejem rokopisa – received: 2011-02-28; sprejem za objavo – accepted for publication: 2011-05-24*

The change of microstructure for a super duplex stainless steel SAF 2507 during hot rolling was investigated. Its evolution during hot deformation was very different in each phase. The dominant restoration mechanism for ferrite and austenite were dynamic recovery (DRV) and dynamic recrystallization (DRX), respectively. Also, the effect of temperature on the deleterious phase precipitation was investigated. The specimens were heat treated isothermally in the temperature range 800 °C to 1000 °C. Hardness tests, and optical and scanning electron microscopy were used to detect the sigma phase.

**Key words:** super duplex stainless steel, hot rolling, microstructural evolution, sigma phase, ageing, hardness

Med vročim valjanjem je bil raziskan mikrostrukturni razvoj v superdupleksnem nerjavnem jeklu SAF 2507, ki se med vročo deformacijo razlikuje v vsaki fazi. Prevladujoč mehanizem mehčanja v feritu in avstenitu je bila dinamična poprava in/ali dinamična rekristalizacija. V superdupleksnem nerjavnem jeklu je bil raziskan vpliv temperature na izločanje škodljivih faz. Vzorci so bili izotermno toplotno obdelani v temperaturnem območju od 800 °C do 1000 °C. Uporabljene so bile meritve trdote ter optična in elektronska mikroskopija za analizo sigma-faze.

**Ključne besede:** superdupleksno nerjavno jeklo, vroče valjanje, mikrostrukturni razvoj, sigma-faza, žarjenje, trdota

## 1 INTRODUCTION

Depending on the chemical composition and applied thermomechanical processing, the microstructure of super duplex stainless steels (SDSS) consists mostly of different shares of ferrite and austenite and eventually of deleterious intermetallic phases. As a result, the optimisation of the mechanical properties and corrosion resistance of SDSS depends on the precise control of the evolution of the microstructure during the hot deformation and the subsequent ageing process. On the other hand, a solidification mode and an appropriate treatment is necessary to avoid the formation of undesirable intermetallic phases, e.g.,  $\sigma$  and  $\chi$ .<sup>1,2,3</sup> It is supposed that among the intermetallic precipitates, the sigma phase is the most detrimental, as it causes a considerable drop in the toughness and the corrosion resistance.<sup>4</sup> Thus, the proper control of the thermomechanical processing and subsequent ageing treatment are obligatory, not only for avoiding harmful precipitates, but also for achieving the desired mechanical properties. The hot ductility of the SDSS turns out to be extremely poor, making the production of DSS sheet steel very challenging.<sup>5,26</sup> Some authors suggested that the strain partitioning between ferrite and austenite of internal stresses at the phase boundaries and the segregation of impurities may lead to crack formation.<sup>5,6,7</sup>

Duplex or ferritic-austenitic stainless steels have a history almost as long as stainless steels. Along with the increased knowledge of use of alloying elements the process techniques in steel mills were also improved. With AOD or VOD and similar refining processes it was possible to add nitrogen in an inexpensive way and so reduce the levels of harmful impurities. The increasing alloying content makes the microstructure more prone to the precipitation of intermetallic phases with a negative effect on the corrosion resistance and ductility. There has been ample discussion concerning the individual effects of molybdenum and tungsten and the conclusion was that the replacement of Mo with W or Cu has a negligible effect on the phase stability and corrosion resistance. Copper additions were made to improve the corrosion resistance in reducing acids and alloying with tungsten was used to further improve the pitting resistance.<sup>8</sup> On the other hand, copper has been found to segregate on the surface of ferritic steels. The intensity of its surface segregation depends on the annealing temperature and its bulk content.<sup>9</sup>

The purpose of our investigation was to determine the effect of ageing in the temperature range from 800 °C to 1000 °C and hot rolling in the range from 1250 to 900 °C on the microstructural evolution of SDSS grade SAF 2507.

## 2 EXPERIMENTAL WORK

The SDSS SAF 2507 with the composition in **Table 1** was received as 20-mm thick plate from an industrial hot-rolling line. The as-received microstructure of the SAF 2507 shown in **Figure 1** consisted of approximately 58 % austenite and 42 % ferrite. Flat-shaped specimens (dimension of  $60 \times 47 \times 20$ ) mm) were soaked for 30 min at 1250 °C, transferred to a furnace, held at the rolling temperature in the range from 1250 °C to 900 °C in steps of 50 °C. The specimens were hot rolled in three passes with 20 % of the pass deformation. Afterwards, the specimens were aged at a temperature of 800 °C to 1000 °C for different times of (30, 120, 240 and 420) min and water quenched. To characterize the microstructures, the specimens were treated with standard grinding and polishing techniques, etched and examined with optical and scanning electron microscopy using secondary-electron emission with a 15 kV to 20 kV electron beam.

The material was supplied with a PREN (pitting resistance equivalent number) of 43, calculated using equation 1, which estimates the influence of the alloying elements Cr, Mo and N on the corrosion resistance in Fe-Cr-Ni alloys. The chemical composition (*w*%) of duplex stainless steel is balanced to give approximately equal amounts of ferrite and austenite in the solution-annealed condition. The higher the annealing temperature, the higher is the ferrite content.

$$PREN/\% = w(\text{Cr}) + 3.3 w(\text{Mo}) + 16 w(\text{N}) \quad (1)$$

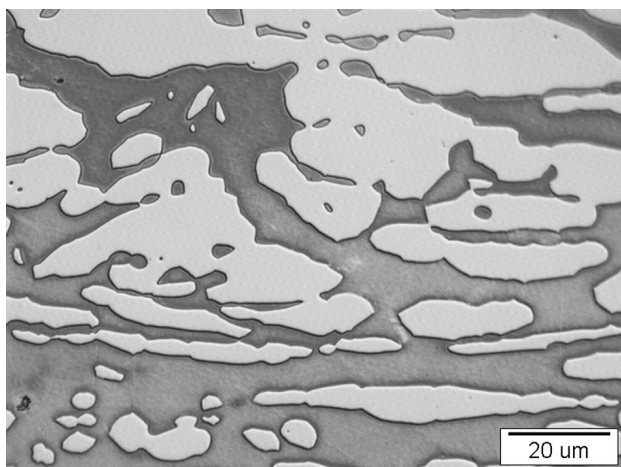


**Figure 1:** Microstructure of the as-received SAF 2507 super duplex stainless steel

**Slika 1:** Mikrostruktura superdupleksnega nerjavnega jekla SAF 2507

## 3 RESULTS AND DISCUSSION

### 3.1 Evolution of the microstructure

The two-phase microstructure shown in **Figure 1** consists of austenite islands in a ferrite matrix. The microstructure after rolling with  $(3 \times 20)$  % deformation is shown in **Figure 2**. The austenite islands are slightly elongated in the rolling direction. During test rollings the main change in microstructure is a more uniform distribution of ferrite and austenite. The presence of a bcc ferrite phase, which has numerous slip systems and a high stacking fault energy (SFE) in the vicinity of a fcc

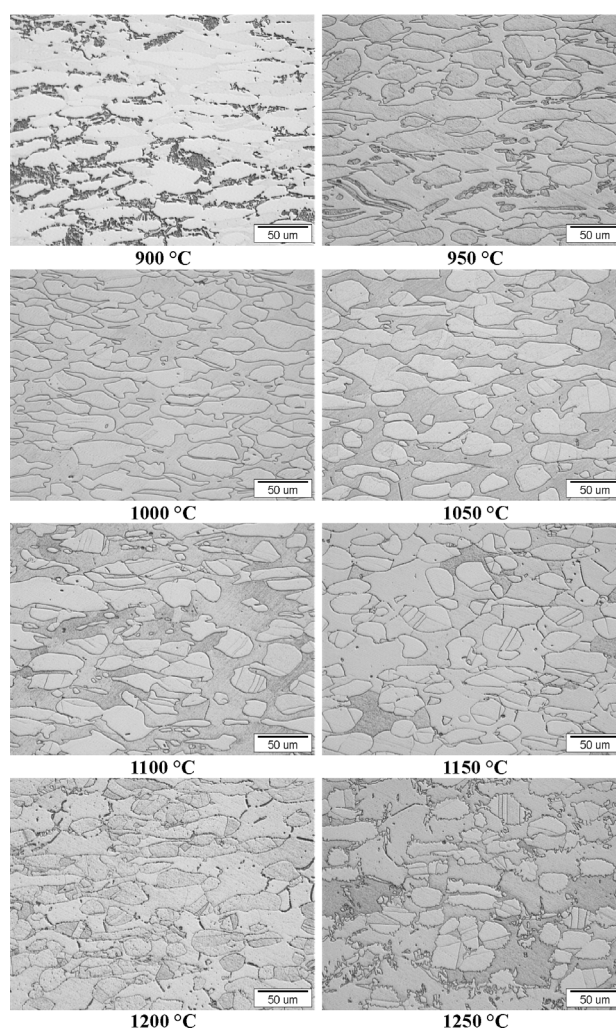


**Figure 2:** Microstructural evolution of SAF 2507 by  $(3 \times 20)$ % per pass deformation

**Slika 2:** Razvoj mikrostrukture SAF 2507 po  $(3 \times 20)$ -odstotni deformaciji

**Table 1:** Chemical composition of SDSS SAF 2507 in mass fractions, *w*%

**Tabela 1:** Kemijska sestava SDSS SAF 2507 v masnih deležih, *w*%

Elements	C	Si	Mn	P	S	Cr	Ni	Mo	Cu	N
<i>w</i> %	0.023	0.3	0.73	0.023	0.0006	25.19	6.86	3.614	0.1	0.26

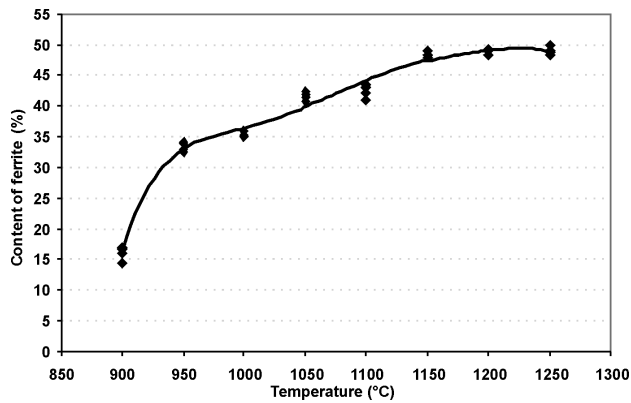


**Figure 3:** Evolution of the content of  $\delta$ -ferrite with deformation temperature

**Slika 3:** Vsebnost  $\delta$ -ferita v odvisnosti od temperature deformacije

austenite phase with less slip systems and low SFE strongly affects the recrystallisation behaviour. The kinetics of the austenite recrystallisation of austenite in the duplex structure is much slower than in a single-phase austenitic steel.<sup>10</sup> The dominant dynamic restoration mechanisms for ferrite and austenite are dynamic recovery (DRV) and dynamic recrystallization (DRX) respectively.<sup>11</sup> The coexistence of hard austenite and soft ferrite at high temperatures is found to result in a strain partitioning at the early stages of deformation, when the strain is mostly accommodated by the ferrite phase.<sup>12</sup> At higher strains, the load is transferred from the ferrite to the austenite leading to increment of dislocation density in the latter till triggering of DRX. An important difference between the DRX austenite phase of a duplex structure and a single-phase austenitic stainless steel is the role of grain-boundary serration and the bulging of new DRX grains with serrated boundaries (only above 1150 °C). Grain-boundary serration and bulging are the most important DRX mechanism in single-phase austenitic steels,<sup>13</sup> whereas this phenomenon is not often observed in the duplex structure, owing to the limited

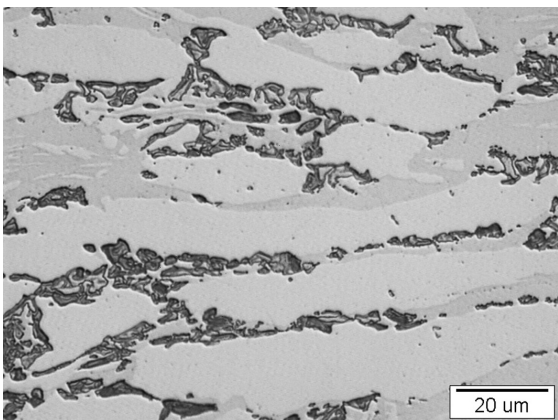


**Figure 4:** SEM secondary-electron micrograph after deformation at 900 °C

**Slika 4:** SEM-posnetek mikrostrukture po deformaciji pri temperaturi 900 °C

number of austenite/austenite grain boundaries. However, where these boundaries exist, they are the sites for new DRX grains on the serrated  $\gamma/\gamma$  boundaries (**Figure 2**, by 1200 °C and 1250 °C).

The microstructure evolution during the hot deformation of the investigated duplex microstructure started with the formation of low-angle grain boundaries (LAGBs) in ferrite without any major influence on austenite<sup>14</sup>. These LABGs are the result of DRV as the dominant restoration mechanism in ferrite. These LABGs evolve and lead to a gradual build-up of higher misorientation between the neighbouring subgrains. The increase in ferrite subgrain size appears to be proportional to the increase in the average misorientation of the sub-boundaries in that phase.<sup>14</sup>

In contrast to ferrite, some discrete grain boundaries were observed in austenite. These actual grains were mostly formed on the serrated initial grain boundaries indicating DRX. The degree of recrystallization becomes larger with an increasing rolling temperature.

The volume fraction of each phase changed during hot deformation by hot rolling. **Figure 3** shows the evolution of the volume fraction of ferrite with the deformation temperature. The amount of ferrite increases between 1050 °C and 1250 °C with a maximum at 1250 °C. Above 1050 °C, the amount of  $\gamma$  phase decreases considerably with the deformation temperature, which is attributed to the  $\gamma \rightarrow \delta$  phase transformation.

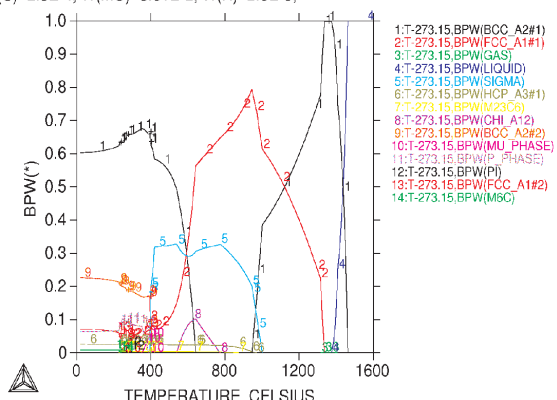
**Figure 4** shows an SEM micrograph of a specimen deformed at 900 °C with a higher magnification. The content of  $\delta$ -ferrite in the specimen was about 15 %. The  $\delta$ -ferrite phase appears slightly darker than the bulk austenite, while the secondary sigma phases are brown. Secondary austenite ( $\gamma_2$ ) appears in the form of islands in a matrix of ferrite, wrapped with a sigma phase having a lacy morphology.<sup>15</sup> It is known that the nucleation of the secondary austenite and sigma phase occurs through the eutectoid reaction  $\delta \rightarrow \sigma + \gamma_2$ .<sup>16</sup> As the precipitation continues, the ferrite stabilisers Cr and Mo diffuse from the ferrite to the sigma phase, which simultaneously force the ferrite to transform to the secondary austenite. While the Cr content only decreases slightly in ferrite, the decrease of Mo is pronounced and forces the Mo to diffuse from the inner parts of the ferrite matrix. This indicates that Mo is the main element controlling the

**Table 2:** Chemical composition of various phases obtained by EDS analysis (w/%)

**Tabela 2:** Kemijska sestava različnih faz z EDS-analizo, v masnih deležih, w/%

Elements	$w(\delta)$	$w(\gamma)$	$w(\sigma)$
Si	$0.36 \pm 0.04$	$0.34 \pm 0.03$	$0.5 \pm 0.08$
Mn	$0.69 \pm 0.11$	$0.95 \pm 0.18$	$0.77 \pm 0.19$
Cr	$26.61 \pm 0.59$	$24.41 \pm 0.36$	$28.23 \pm 0.56$
Mo	$5.11 \pm 0.34$	$3.63 \pm 0.22$	$8.16 \pm 0.21$
Ni	$5.59 \pm 0.45$	$8.03 \pm 0.33$	$4.74 \pm 0.24$

THERMO-CALC (2010.03.30.09.58) :  
 DATABASE:TCFE5  
 P=1.01325E5, N=1, W(SI)=3E-3, W(MN)=7.3E-3, W(CR)=0.2519, W(NI)=6.86E-2,  
 W(C)=2.3E-4, W(MO)=3.61E-2, W(N)=2.6E-3;



THERMO-CALC (2010.03.30.09.59) :  
 DATABASE:TCFE5  
 P=1.01325E5, N=1, W(SI)=3E-3, W(MN)=7.3E-3, W(CR)=0.2519, W(NI)=6.86E-2,  
 W(C)=2.3E-4, W(MO)=3.61E-2, W(N)=2.6E-3;

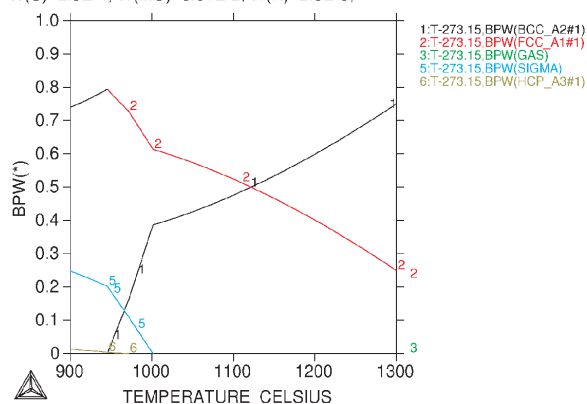


Figure 5: Calculated phase fractions in the investigated super duplex stainless steel SAF 2507

Slika 5: Izračunani deleži faz superdupleksnega nerjavnega SAF 2507

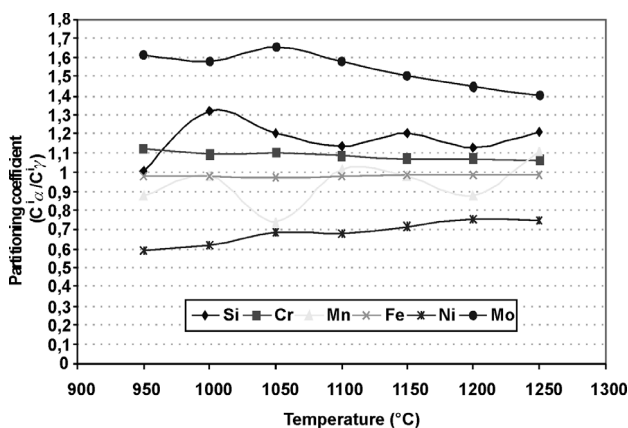


Figure 6: The partitioning coefficient of the alloying elements as a function of rolling temperature

Slika 6: Porazdelitveni koeficient legirnih elementov v odvisnosti od temperature valjanja

sigma phase precipitation.<sup>16</sup> The nucleation of the sigma phase predominantly occurs in ferrite/ferrite and ferrite/austenite grain boundaries. The nucleus then grows into

the adjacent ferrite grains. The average compositions of the constituent phases, i.e.,  $\delta$ -ferrite,  $\gamma$  and sigma phases determined with EDS microanalysis are presented in Table 2. The results indicate that while  $\delta$ -ferrite is rich in Cr and depleted with Ni,  $\gamma$  is rich in Ni and depleted in Cr. The EDS results further reveal that the sigma phase is rich in both Cr and Mo. These values are in good agreement with earlier reported results.<sup>17,18</sup>

As shown in Figure 5 for the SAF 2507 (calculated with Thermo-Calc), intermetallic phase formation does not occur at temperatures above 1010 °C. With a decrease of the rolling temperature, the austenite volume fraction increases significantly from 33 % at 1250 °C up to 62 % at 1000 °C. This change of austenite volume fraction influences the mechanical behaviour of the duplex stainless steel because of the large difference in strength between ferrite and austenite.

### 3.2 Partitioning of elements

In the two-phase structure a clear compositional difference exists between the constituting phases. The elements Cr, Mo and Si are enriched in ferrite, while N, C, Ni and Mn are enriched in austenite and the change in the partitioning of elements as function of temperature occurs (Figure 6). The chemical composition of the phase influences its strength and SFE, hence its softening behavior.<sup>19</sup> Consequently, the changing partitioning of alloying elements with varying temperature contributes to the difference in the hot deformation behaviour of duplex stainless steel between the start and the end of hot rolling. Super duplex stainless steels show excellent hot deformability with a relatively low strain hardening up to at least 1230 °C. If hot rolling takes place at too low a temperature, deformation accumulates in the weaker but less ductile ferrite, which can result in cracking of the ferrite in the deformed region. Additionally, a large amount of sigma phase can be precipitated when the hot rolling temperature drops too low.

### 3.3 Precipitation of $\sigma$ phase

The sigma phase is non-magnetic and intermetallic with the origin composition based in the iron-chromium system. According to the ternary iron-chromium-nickel system, the sigma phase is a thermodynamically stable phase that forms on the chromium-rich side of the ternary phase diagram Fe-Cr-Ni.<sup>20</sup> The mechanism of precipitation is a eutectoid transformation of ferrite into austenite and the sigma phase. The morphology of the sigma-phase precipitation changes depending on the temperature (Figure 7). At the lower temperature of 800 °C, a coral-like structure of sigma phase can be found. The number of single sigma nuclei at the beginning of the formation is rather high and it depends on diffusion distances that are smaller at a lower temperature. The different precipitation behaviour can be observed at higher temperatures of 1000 °C. The sigma phase is

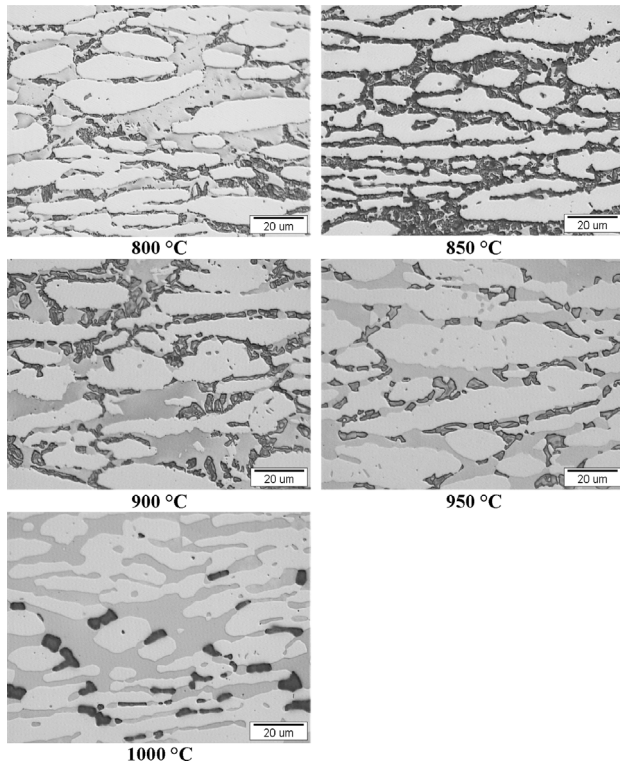


Figure 7: Morphology of the sigma phase at different isothermal annealing temperature, annealing time – 30 min

Slika 7: Morfologija sigma-faze pri različnih temperaturah izotermnega žarjenja; čas žarjenja 30 min

coarser and more compact and the difference is explained by the lower nucleation rate and higher diffusion rate at elevated temperatures.<sup>21</sup> For the SAF 2507 super duplex stainless steel, the precipitation level is pronounced, especially at 850 °C, where the intermetallic sigma phase formed after only 1 minute. In the super duplex stainless steel SAF 2507, ferrite did transform almost completely after only 1 h of ageing at 850 °C.<sup>22</sup>

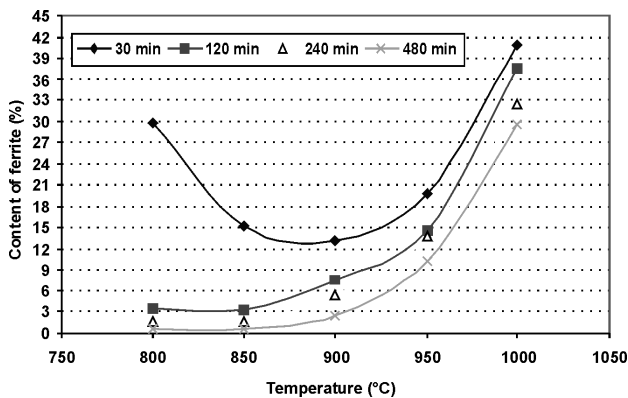


Figure 8:  $\delta$ -ferrite content depending on temperature and time of isothermal annealing

Slika 8: Vsebnost  $\delta$ -ferita v odvisnosti od temperature in časa izotermnega žarjenja

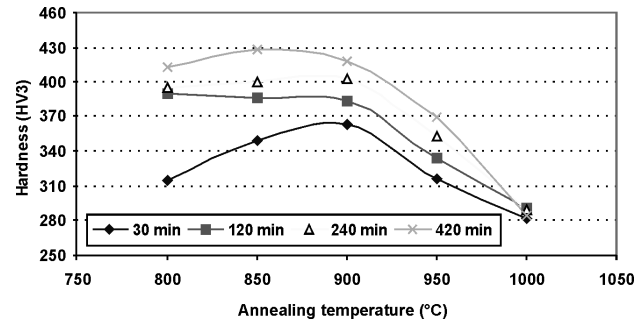


Figure 9: Effect of ageing temperature on the hardness of the steel at different ageing times

Slika 9: Vpliv temperature in časa žarjenja na trdoto jekla

Depending on the temperature and time of isothermal annealing, the microstructure of SAF 2507 super duplex stainless steel may consist of ferrite, austenite and sigma phase delimiting ferritic grain boundaries. The micrographs in Figure 7 show that SAF 2507 is susceptible to sigma-phase formation in the temperature range 800 °C to 900 °C. Mostly, sigma phase is formed preferentially at the ferrite grain boundaries. The high susceptibility of the duplex stainless steels to sigma-phase formation is often attributed to the ferrite chemical composition, since ferrite is rich in sigma-forming elements such as Cr, Mo and Si, and poor in C, N and Ni, which are less soluble in the sigma phase than in austenite.<sup>23</sup> The chemical composition of austenite differs significantly from that of the ferrite due to the presence of ferrite-promoting elements (Cr, Mo and Si), that are enriched in ferrite during the solidification, while austenite-promoting elements (C, Ni and N) are enriched in austenite. With increasing annealing the quantity of sigma phase is increased with gradual growth through ferrite until the eventual consumption of entire ferrite grains.

The content of ferrite in the microstructure as a function of the annealing treatment is shown in Figure 8. It depends on the temperature and time of isothermal annealing.

The formation of  $\sigma$  phase is considered to be the main reason for the increase of hardness with annealing time and temperature. Figure 9 shows the dependence between the hardness and the annealing time for different temperatures. The curves are similar in shape in the temperature range of 800 °C to 1000 °C for annealing times of (120, 240 and 480) min. For 30 min annealing the hardness is increased in the temperature range 800 °C to 900 °C from an initial non-aged value of 256 HV3, for the microstructure in Figure 1, to a maximum hardness value of 363 HV3 at 900 °C. The increased hardness is caused by the presence of a greater amount of secondary austenite and  $\sigma$  phase. After the ageing at 1000 °C, the hardness was slightly higher (282 HV3) than that measured at the solution annealed material (256 HV3). A pronounced increase in hardness was found in the temperature range 800 °C to 900 °C

with an increase in the ageing time from 30 min to 120 min. The hardness values are in general agreement with the microstructure evolution and it seems that the longer-time isothermal ageing is much more effective in hardening the super duplex stainless steel.<sup>24</sup>

After solution annealing at 1075 °C, 1100 °C and 1125 °C and quenching in water the sigma phase is decomposed and a duplex microstructure of ferrite and austenite is obtained. No intermetallic phase was found at the grain boundaries and inside the ferrite grains. **Table 3** shows the properties obtained after solution annealing. Similar results have been reported for the UNS S32750 super duplex stainless steel after the same testing conditions.<sup>25</sup>

**Table 3:** The tensile test results obtained after solution treatment  
**Tabela 3:** Mehanske lastnosti jekla po raztopnem žarjenju

Temperature $T/^\circ\text{C}$	$\sigma_{\text{YS}}/\text{MPa}$	$\sigma_{\text{UTS}}/\text{MPa}$	Elongation (%)	Reduction of area (%)
1125	616	869	31	64
1100	613	864	31,1	64
1075	612	859	31,9	64

#### 4 CONCLUSIONS

The microstructure of duplex stainless steel SAF 2507 consists of different amounts of ferrite and austenite as well as unwanted intermetallic phases. The optimisation of the mechanical properties and corrosion resistance of this steel depends on the development of the microstructure of the alloy between hot deformation and latest process of annealing for preventing the formation of intermetallic phases. From the results of the investigation of the microstructure after rolling and isothermal annealing in the range of temperature between 800 °C and 1250 °C it is concluded that:

During hot deformation, dynamic recovery and polygonization in the ferrite occurs. In austenite there are nuclei of recrystallized grains on serrated boundaries at the temperature of rolling equal to 1200 °C and above. Practically at all temperatures of super duplex deformation over 1000 °C the deformation twins in grains of austenite appear. The dominant dynamic restoration mechanisms for ferrite and austenite are dynamic recovery (DRV) and dynamic recrystallization (DRX), respectively. However, owing to the limitation in the number of austenite/austenite boundaries, the evolution of DRX in austenite was limited. In stainless steel SAF 2507 the intermetallic phase  $\sigma$  at temperature of deformation 950 °C and lower is also formed.

In the area of hot deformation the proportion of phases ferrite and austenite is changed, also. The content of ferrite after triple deformation at initial temperature of deformation 1250 °C is of 47 % and it is reduced to 34 % at a temperature of deformation of 950 °C. At a deformation temperature of 900 °C, the share of ferrite is

drastically reduced because of the eutectoid transformation in the phase  $\sigma$  and in the secondary austenite.

In a two-phase microstructure the differences in the contents of alloying elements between the phase constituents exist. The elements chromium, molybdenum and silicon are enriched in ferrite, while nitrogen, carbon, manganese and nickel are enriched in austenite. At a higher temperature of deformation the differences in the composition of both phases are lower, because of the change of their ratio.

Within the optimal area of hot processing and air cooling the microstructure of the duplex stainless steel remains within the two-phase field of the phase diagram Fe-Cr-Ni. The microstructure consists of alternative lamellas of ferrite and austenite.

The volume share of the  $\sigma$ -phase is relatively great at a temperature of deformation of 900 °C and is he cause for an increase of the deformation resistance and the mechanical properties of steel. The temperature of isothermal annealing affects strongly the volume share and morphology of the phase  $\sigma$ . At a lower temperature of precipitation the phase  $\sigma$  has a coral morphology. The higher propensity to precipitation of the phase  $\sigma$  in the duplex stainless steel is connected with the ferrite composition, which is enriched by elements that form phase  $\sigma$  (Cr, Mo and Si) and depleted of elements that are less soluble, for example, C, N and Ni. The phase  $\sigma$  grows into ferrite grains because it is thermodynamically more stable and with its formation the system achieves the equilibrium state.

The equilibrium microstructure in the temperature range between 800 °C and 900 °C is a mixture of austenite and phase  $\sigma$ . The results show that the super duplex stainless steel SAF 2507 is very sensitive to the formation of phase  $\sigma$  in the temperature range between 800 °C and 900 °C.

The investigation verified that the formation of the phase  $\sigma$  is the main reason for an increase of the hardness independent of the annealing time and temperature. By annealing at 1075 °C, 1100 °C and 1125 °C the sigma phase is dissolved and ferrite and austenite are obtained, which is typical for the duplex structure.

#### 5 REFERENCES

- <sup>1</sup> L. Karlsson, L. Bengtsson, U. Rolander, S. Pak, Applications of Stainless Steel 92, Stockholm, Sweden, (1992) 1, 335–344
- <sup>2</sup> S. Hetzman, B. Lehtinen, E. Symniotis-Barradal, Applications of Stainless Steel 92, Stockholm, Sweden, (1992) 1, 345–359
- <sup>3</sup> D. Steiner Petrovič, G. Klančnik, M. Pirnat, J. Medved. J. Therm. Anal. Calorim., (2011), doi: 10.1007/s10973-011-1375-2
- <sup>4</sup> Y. S. Ahn, J. P. Kang, Mater. Sci. Technol., (2000) 16, 382–387
- <sup>5</sup> E. Evangelista, H. J. McQueen, B. Verlinden, M. Barteri, Proc. 3<sup>rd</sup> European Stainless Steels Conf., Science and Market, Sardinia, Italy, (1999), 253
- <sup>6</sup> O. Balancin, W. A. M. Hoffmann, J. J. Jonas, Metalurgical and Materials Transactions A, 31A (2000), 1353
- <sup>7</sup> M. Torkar, F. Vodopivec, S. Petovar, Mater. Sci. Eng. A, 173 (1993), 313–316

- <sup>8</sup> S. Hertzman, B. Lehtinen, E. Symnietis-Barrdahl, Proc. of the Duplex Stainless Steels 2000, Venezia, Italy, (2000), 347
- <sup>9</sup> D. Steiner - Petrovič, D. Mandrino, S. Krajinović, M. Jenko, M. Milun, V. Doleček, M. Jeram, ISIJ Int., 46 (2006) 10, 1452–1457
- <sup>10</sup> A. Izza - Mendia, A. Pinol - Juez, J. J. Urcola, I. Gutierrez, Metall. Mater. Trans. A, 29A (1998), 2975–2986
- <sup>11</sup> T. Maki, T. Furuhashi, K. Tsuzaki, ISIJ Int., (2001) 41, 571–579
- <sup>12</sup> O. Balancin, W. A. M. Hoffmann, J. J. Jonas, Metall. Mater. Trans. A, 31A (2000), 1353–1364
- <sup>13</sup> A. Belyakov, H. Miura, T. Sakai, Mater. Sci. Eng. A, A255 (1998), 139–147
- <sup>14</sup> X. Huang, T. Tsuzaki, T. Maki, Acta. Metall. Mater., 43 (1995), 3375–3384
- <sup>15</sup> M. Martins, L. C. Casteletti, Mater. Charact., (2005) 55, 225–233
- <sup>16</sup> J. O. Nilsson, Mater. Sci. Technol., (1992) 8, 571–579
- <sup>17</sup> T. H. Chen, K. L. Weng, J. R. Yang, Mater. Sci. Eng. A, A338 (2002), 259–270
- <sup>18</sup> Y. Maehara, M. Koike, N. Fujino, T. Kunitake, Trans. ISIJ, 23 (1983), 240–246
- <sup>19</sup> L. Duprez, B. C. Decooman, N. Akdut, Steel Research, 73 (2002) 12, 531–538
- <sup>20</sup> H. Hoffmeister, R. Mundt, Arch. Eisenhüttenwes., 52 (1981), 159–164
- <sup>21</sup> M. Pohl, O. Storz, T. Glogowski, Mater. Charact., 58 (2007), 65–71
- <sup>22</sup> H. Liu, P. Johansson, M. Liljas, Proc. 6<sup>th</sup> European Stainless Steels Conf., Science and Market, Helsinki, Finland, (2008), 555–560
- <sup>23</sup> D. M. E. Villanueva, F. C. P. Junior, R. L. Plaut, A. F. Padilha, Mater. Sci. Technol., 22 (2006), 1098–1104
- <sup>24</sup> S. K. Ghosh, S. Mondal, Mater. Charact., 59 (2008), 1776–1783
- <sup>25</sup> J. M. Pardal, S. S. M. Tavares, M. Cindra Fonseca, J. A. de Souza, Mater. Charact., 60 (2009), 165–172
- <sup>26</sup> A. Kocijan, Č. Donik, M. Jenko, Mater. Technol., 43 (2009) 1, 39–42



# OPTIMIZATION OF THE QUALITY OF CONTINUOUSLY CAST STEEL SLABS USING THE FIREFLY ALGORITHM

## OPTIMIZACIJA KAKOVOSTI KONTINUIRNO LITE JEKLENE PLOŠČE Z UPORABO ALGORITMA "FIREFLY"

**Tomas Mauder, Cenek Sandera, Josef Stetina, Milos Seda**

Brno University of Technology, Faculty of Mechanical Engineering, Technicka 2, Brno, Czech Republic  
ymaude00@stud.fme.vutbr.cz

*Prejem rokopisa – received: 2010-10-20; sprejem za objavo – accepted for publication: 2011-03-21*

The ambition to increase both the productivity and the product quality in the continuous casting process, led us to study new, effective mathematical approaches. The quality of the steel produced with the continuous casting process is influenced by the controlled factors, such as the casting speed or cooling rates. The appropriate setting of these factors is usually obtained with expert estimates and expensive experimental runs. This paper describes an algorithm for obtaining a black-box-type solution which maintains a high production rate and the high quality of the products. The core of the algorithm is our original numerical model of 2D temperature field designed for the real caster geometry. The mathematical model contains Fourier-Kirchhoff equation and includes boundary conditions. Phase and structural changes are modeled by the enthalpy computed from the chemical composition of the steel. The optimization part is performed with a recently created heuristic method, the so-called Firefly algorithm, in which the principles of searching for optimal values are inspired by the biological behavior of fireflies. Combining the numerical model and heuristic optimization we are able to set the controlled values and to obtain high-quality steel that satisfies the constraints for the prescribed metallurgical length, core and surface temperatures. This approach can be easily utilized for an arbitrary class of steel only by changing its chemical composition in the numerical model. The results of the simulations can be validated with real historical data in order to compare the relationship between the temperature field and the final product quality.

**Key Words:** continuous casting, Firefly algorithm, temperature field, enthalpy approach

Ambicije za povečanje produktivnosti in kakovosti končnega proizvoda pri kontinuirnem ulivanju sta nas pripeljala do študija novih učinkovitih matematičnih prijemov. Na kakovost jekla, proizvedenega s kontinuirnim ulivanjem, vplivajo številni nadzorovani dejavniki, kot sta npr. hitrost ulivanja in ohlajanja. Ustrezno določanje teh dejavnikov je navadno povezano s strokovnimi ocenami in dragimi poizkusi. Prispevek opisuje algoritem za vrsto rešitev za ohranjanje visoke stopnje proizvodnje in visoke kakovosti izdelkov. Jedro algoritma je naš prvotni numerični model 2D-polja temperature, namenjen ulivalni geometriji. Ta matematični model vsebuje Fourier-Kirchhoffovo enačbo in tudi robne pogoje. Fazne in strukturne spremembe so bile modelirane z entalpijo, izračunano iz kemijske sestave jekla. Optimizacijski del je bil izveden z nedavno narejeno heuristično metodo, s tako imenovanim algoritmom Firefly, kjer načela iskanja optimalnih vrednosti temeljijo na biološkem vedenju kresnic. Z združevanjem numeričnega modela in heuristične optimizacije smo lahko predpisali nadzorovane vrednosti za izdelavo visokokakovostnega jekla, ki izpolnjuje predpisane pogoje za zagotovitev metalurške dolžine, ter temperature jedra in površine. Ta način je mogoče enostavno uporabiti za katero koli vrsto jekla le s spremembo kemične sestave v numeričnem modelu. Rezultate simulacij lahko potrdimo z resničnimi podatki iz preteklosti s primerjavo razmerja med temperaturnim poljem in kakovostjo končnega izdelka.

**Ključne besede:** kontinuirno litje, entalpija, algoritem Firefly, temperaturno polje

## 1 INTRODUCTION

Nowadays, continuous casting is the most common way of producing steel in the world. Every year, the steel industry processes millions of tons of liquid steel into semi-finished products such as slabs, blooms, and billets. A schematic representation of the continuous caster is shown in **Figure 1**. Molten steel (roughly 1550 °C) is poured down from a tundish into a water-cooled mould (primary cooling zone), where the steel obtains a solid shell. Afterwards, the steel is transported by rollers and cooled down by water sprays (secondary cooling zone). Groups of nozzles of sprays divide the secondary cooling zone into several coolant circuits. In the last zone, the steel surface is cooled down by free convection and radiation only (tertiary cooling zone).

Every steel company wants to produce steel as quickly as possible, while preserving the required

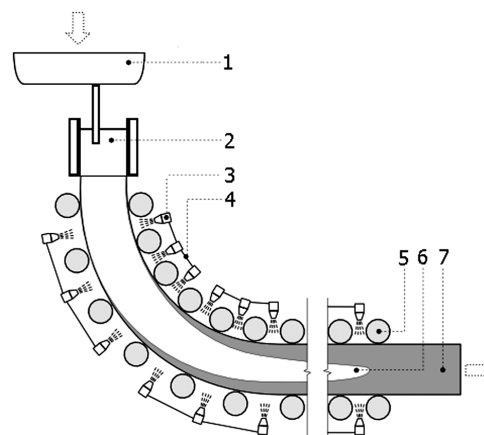


**Figure 1:** Scheme of continuous casting. 1 – tundish; 2 – mould; 3 – nozzle; 4 – coolant circuit; 5 – roller; 6 – liquid material; 7 – solid material

**Slika 1:** Shema kontinuirnega litja: 1 – vmesna ponova; 2 – kokila, 3 – šobe; 4 – hladilne šobe, 5 – valj, 6 – tekoči koren; 7 – trdna snov

quality<sup>1</sup>. There are a few ways to optimize the casting velocity and the output quality simultaneously. One possible method is to perform industrial trials, but this is very expensive and time-consuming. A better way is to use numerical simulations of the casting process and adjust these parameters to the optimal values. Previous studies were generally based on a simplified 2D temperature field model and were optimized by mathematical programming<sup>6</sup>, neural networks or a genetic algorithm.<sup>2</sup> These models describe the casting process very roughly and, therefore, their usage in real casters is not satisfactory.

Our original numerical model of the temperature field is designed for the real caster geometry. A modern heuristic method called the Firefly algorithm is used for the optimization of the model.

## 2 DEFINITION OF THE PROBLEM

The goal of the optimization is to improve the material properties of the final slab and increase the rate of production. With the aim to achieve this goal, we modified the casting process by controlling the casting speed and the cooling rates. The productivity is defined as the amount of cast material per unit time, thus, we maximize the casting speed under certain metallurgical criteria. The metallurgical criteria used in the optimization are formulated as a series of constraints that represent the quality of the slab products and the process feasibility. The criteria that must be met are the completeness of solidification before the unbending point (metallurgical length) and reaching the prescribed temperature in the exit area. The quality of the final material is influenced by the change of the surfaces and the core temperatures. The changes have to decrease in the whole profile and the temperature in the straightening area must be in the given range. The values for these constraints depend on the grade of cast steel.

## 3 MATHEMATICAL MODEL OF THE TEMPERATURE FIELD

All three basic mechanisms of heat transfer are incorporated into our model in a differential form. The conduction mechanism plays the dominant role inside the body of the cast steel, whereas convection and radiation take place only in the secondary and tertiary cooling zones, where they form the boundary conditions. The temperature field of the slab is described by the Fourier-Kirchhoff equation,<sup>3,4</sup> where the velocity component  $v_y$  (m/s) is considered only in the direction of casting. Phase and structural changes are included in the model by the use of a thermo-dynamical function of the volume enthalpy  $H$  (J/m<sup>3</sup>). The method is also called an enthalpy approach.<sup>3</sup>

$$\frac{\partial H}{\partial \tau} = \frac{\partial}{\partial x} \left( k \frac{\partial T}{\partial x} \right) + \frac{\partial}{\partial y} \left( k \frac{\partial T}{\partial y} \right) + v_y \frac{\partial H}{\partial y} \quad (1)$$

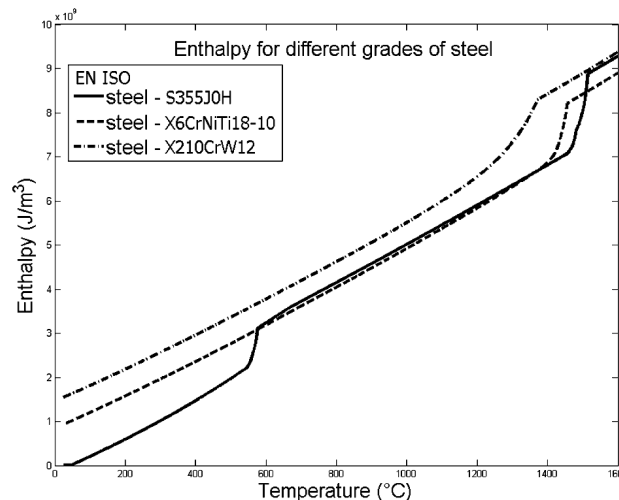


**Figure 2:** Relationship between the temperature and the enthalpy for three grades of steel

**Slika 2:** Razmerje med temperaturo in entalpijo za tri različna jekla

Equation (1) describes an unsteady-state 2D heat transfer (Fourier-Kirchhoff) written in Cartesian coordinates, where  $k$  (W/mK) is the thermal conductivity,  $T$  (K) is the temperature,  $H$  (J/m<sup>3</sup>) is the volume enthalpy,  $\tau$  (s) is the real time, and  $x$ ,  $y$ , are space coordinates. In order to have a well-defined problem, the initial and boundary conditions must be provided. The boundary conditions include the heat flux in the mould and under the rollers, forced convection under the nozzles and free convection and radiation in the tertiary cooling zone. The complete numerical model of the temperature field, including boundary conditions in Cartesian and cylindrical coordinates, can be found in.<sup>4</sup>

Equation (1) is discretized by the finite-difference method<sup>3,4</sup> using an explicit formula for the time derivative. The mesh for the finite-difference scheme is non-equidistant and its nodes are adapted to the real rollers and the positions of the nozzles. Equation (1) contains both enthalpy and temperature, so during the simulation the corresponding temperature must be calculated from the enthalpy for each node at each time step. **Figure 2** shows the relationship between the temperature and the enthalpy for three different grades of steel. This numerical model allows us to apply various enthalpy-temperature functions and thermal conductivity-temperature curves, and thus the temperature field can be calculated for various steels, only by defining their chemical composition.

## 4 OPTIMIZATION ALGORITHM

Our aim is to optimize the continuous casting process by processing its mathematical model. The only parameters we can control are the casting speed and the cooling rates. These parameters are included in the initial and boundary conditions of the model and they can acquire real values from a given continuous bound

interval. We need to find their values such that the final temperature field is the best possible. This problem belongs to the area of nonlinear constraint optimization and, therefore, it is usually impossible to obtain the exact solution. We use a method based on nature-inspired metaheuristics called the firefly algorithm.

The main principle is to maintain a group of fireflies where each of them represents one particular solution. These solutions must be comparable with each other in order to be able to decide which one represents a better solution and which one is worse. The algorithm starts with a number of randomly generated solutions (fireflies) and with their evaluations. The evaluation (also called the objective function) describes how much the solution is good and how much it violates the prescribed constraints. During the iteratively repeated algorithm steps, the worse fireflies move towards the better ones and at the end of the computation most of them are concentrated around the best discovered solution. A detailed description of these metaheuristics can be found in.<sup>5</sup>

The firefly, in our implementation, is represented by a vector of fourteen real numbers, the first of which is the casting speed and the next thirteen numbers describe the cooling rates for thirteen cooling circles in the caster. Therefore, the search space of all possible solutions has fourteen independent dimensions and the fireflies moves there according to the aforementioned scheme. The evaluation function is defined as a weighted sum of optimized quantity (casting speed) and values representing the violations of the prescribed metallurgical criteria.

Each evaluation involves one simulation run of the model with parameters related to the actual firefly. This is quite time-consuming because the numerical simulations usually take a long time.

The firefly algorithm is not the only possible method for solving problems like this. It was chosen from a range of other heuristics because of its uncomplicated implementation and its appropriate performance in a real-valued optimization.

## 5 RESULTS AND DISCUSSION

We implemented the described heuristic algorithm in Python and the numerical model of the temperature field in MATLAB. The communication between them is provided through COM technology. The algorithm was tested on the geometry of a real caster with the steel number S355J0H. The objective function contains the weighted sum of the casting speed, the conditions for the length of the liquid material between 15 and 20 meters, the temperature in the bent part above 1000 °C, the decreasing trend of the temperature courses and the temperature in the exit part between 700 °C and 800 °C. The criteria of the metallurgical length and the exit temperature have to be fulfilled, and thus they have the

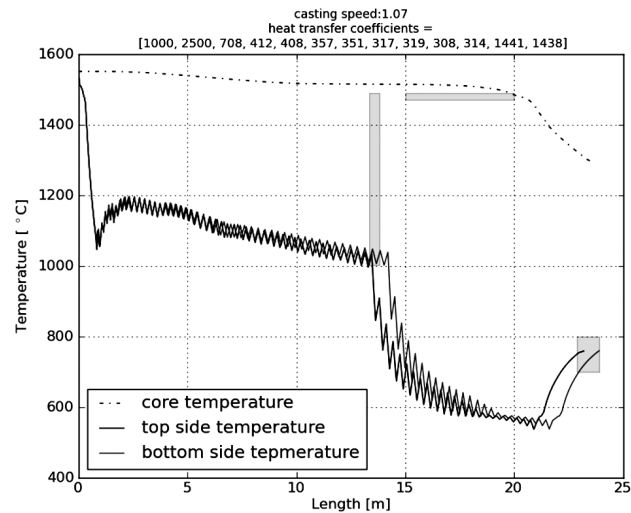


Figure 3: Surface and core temperature  
Slika 3: Temperatura površine in jadra

highest weight. The rest of the conditions have similar weights as each other.

After 10 iterations of 6 randomly chosen fireflies we obtained the result shown in **Figure 3**. It represents temperatures in the middle of the slab, and on its surfaces. The small oscillations are caused by alternating rollers and nozzles and they do not influence the quality of the material significantly.

The optimal speed was found to be 1.07 m/min and the metallurgical length is 19.9 m. If the metallurgical length was not on its maximum it would mean that there is a possibility for increasing the casting speed. But because our metallurgical length is almost 20 m, we have a good indication that we found at least a local extreme. The surface temperatures are above 1000 °C in the whole bent part (up to 13 m) and it keeps the material deformable before the straightening. The temperature in the last part increases, because there are no nozzles and the heat from the kernel is transported on the surface.

The obtained optimal solution fulfils all the prescribed conditions and the steel cast produced with this setting is of high quality and very economical.

## 6 CONCLUSION

This paper deals with suitable tools for optimization of the slab casting process. We have created an algorithm for the fast and effective casting of high-quality steel. The algorithm controls the cooling rates in the developed numerical model and optimizes it by using the so-called firefly algorithm. The obtained solution complies with all the specified criteria and therefore it can produce cheap final material. The whole method is very flexible and can be modified for an arbitrary grade of steel or quality conditions.

Further research will focus on making the algorithm more precise. This includes the 3D numerical model and

the specification of all the conditions that influence the final quality of the cast steel.

#### ACKNOWLEDGEMENT

The authors gratefully acknowledge the financial support from the projects GA106/08/0606 and GA106/09/0940 funded by the Czech Science Foundation, Junior research project on BUT BD13002 and Specific research BD 13001002.

#### 7 REFERENCES

- <sup>1</sup> A. S. Normanton, et al., Improving surface quality of continuously cast semis by an understanding of shell development and growth, Final report, Technical steel research series, Luxembourg, (2005), 349
- <sup>2</sup> C. A. Santos, J. A. Spim, A. Garcia, Mathematical modeling and optimization strategies (genetic algorithm and knowledge base) applied to the continuous casting of steel, *Engineering Applications of Artificial Intelligence*, 16 (2003), 511–527
- <sup>3</sup> D. M. Stefanescu, *Science and Engineering of Casting Solidification*, Second Edition, New York, Springer Science, (2009), 402
- <sup>4</sup> J. Stetina, F. Kavicka, J. Dobrovska, L. Cemek, M. Masarik, Optimization of a concasting technology via a dynamic solidification model of a slab caster. *Materials Science Forum*, (2005) 5, 475–479, 3831–3834
- <sup>5</sup> S. Lukasik, S. Zak, Firefly Algorithm for continuous constrained optimization tasks, *Computational Collective Intelligence. Semantic Web, Social Networks and Multiagent Systems Lecture Notes in Computer Science*, 5796 (2009), 97–106, DOI: 10.1007/978-3-642-04441-0\_8
- <sup>6</sup> T. Mauder, J. Novotny, Two mathematical approaches for optimal control of the continuous slab casting process, *Mendel 2010 – 16th International Conference on Soft Computing*, Brno, Brno University of Technology, 2010, 395–400

## HOT WORKABILITY OF 95MnWCr5 TOOL STEEL VROČA PREOBLIKOVALNOST ORODNEGA JEKLA 95MnWCr5

Ažbe Križaj<sup>2</sup>, Matevž Fazarinc<sup>1</sup>, Monika Jenko<sup>2</sup>, Peter Fajfar<sup>1</sup>

<sup>1</sup>University of Ljubljana, Faculty of Natural Science and Technology, Aškerčeva cesta 12, SI-1000, Ljubljana, Slovenia

<sup>2</sup>Institute of Metals and Technology, Lepi pot 11, SI-1000 Ljubljana, Slovenia  
peter.fajfar@omm.ntf.uni-lj.si

*Prejem rokopisa – received: 2011-04-18; sprejem za objavo – accepted for publication: 2011-06-01*

The hot workability of a 95MnWCr5 medium-alloyed cold-work tool steel was investigated with hot-compression tests on a Gleeble 1500D thermo-mechanical simulator. The tests were performed in the temperature range 850–1150 °C and strain-rate range 0.001–10 s<sup>-1</sup>. With decreasing of the deformation temperature and increasing of the strain-rate values of the peak strain, the peak and steady-state stresses increase. The hyperbolic sine Arrhenius function was used to determine the apparent activation energy for the hot workability. The apparent activation energy of 356 kJ mol<sup>-1</sup> for entire hot-working range was calculated using the peak stresses. The power-dissipation maps exhibited a single domain with the peak of efficiency in the range 30–40 %, the temperature range 960–1100 °C and a strain rate of 1.0 s<sup>-1</sup>.

Key words: cold-work tool steel, hot workability, activation energy, power-dissipation maps

Raziskana je bila vroča preoblikovalnost orodnega jekla za delo v hladnem 95MnWCr5. Na termomehanskem simulatorju Gleeble 1500D so bili izvedeni tlačni preizkusi v temperaturnem območju 850–1150 °C in v območju hitrosti deformacije 0,001–10 s<sup>-1</sup>. S padajočo temperaturo deformacije naraščajo vrednosti najvišjih deformacij in napetosti ter napetosti pri stabilnem stanju. Z uporabo sinušiperbolične Arrheniusove funkcije je bila izračunana navidezna aktivacijska energija za vroče preoblikovanje. Na celotnem temperaturnem področju ter za maksimume napetosti tečenja izračunana aktivacijska energija je 356 kJ mol<sup>-1</sup>. Na mapah učinkovitosti porazdelitve energije je le eno območje z največjim izkoristkom v območju 30–40 %, in sicer pri temperaturah v območju 960–1100 °C in hitrosti deformacije 1,0 s<sup>-1</sup>.

Gljučne besede: orodna jekla za delo v hladnem, vroča preoblikovalnost, aktivacijska energija, mapa učinkovitosti porazdelitve energije

### 1 INTRODUCTION

Tool steels are used for tools and dies where resistance to wear, toughness, strength at high temperatures and stability during heat treatment are required. These properties are achieved by a combination of solid-solution enrichment of the matrix (Mn, Si) and the effect of carbides (W, V, Cr). However, the presence of carbides makes the hot deformation very difficult.<sup>4,5</sup> The type of eutectic carbides, their quantity, morphology, size and distribution, depend on the chemical composition of the tool steel as well as on the production sequences route that lead to different initial microstructures and, consequently, to different hot-deformation abilities of the tool steels. Thus, a large number of parameters, i.e., chemical composition, processing parameters, deformation conditions, stress state, etc., which are usually mutually dependent, influences the hot workability of the tool steels that makes a study of the hot workability of these steels very demanding. It is now generally understood that the workability consists of two independent parts: the state-of-stress workability (SoS) and the intrinsic workability.<sup>1</sup> The SoS workability depends on the geometry of the deformation zone in which the workpiece is subject to a three-dimensional stress state. Thus, for obtaining good intrinsic workability, it is essential to select the appropriate process parameters to obtain the appropriate initial microstructure. The internal

behavior in the material during hot deformation, i.e., the hardening, dynamic recrystallization (DRX), etc., can be implicitly expressed by the shape and the height of the flow curves.<sup>2,3</sup>

The hot workability of tool steels and other steels has been studied by several authors.<sup>4–18</sup> Imbert *et al.*<sup>7–11</sup> investigated the hot workability of five different steel grades: A2, a medium carbon cold-work tool steel; D2, a high-carbon, high-chromium, cold-work die steel; M2, a high-speed steel; W1, a water-hardening, carbon tool steel; and H13, an air-hardening tool steel. For these grades that represent a wide variety of compositions (and carbide contents) continuous hot torsion tests were performed in the temperature range 900–1200 °C and strain rate range 0.1–4 s<sup>-1</sup>. In a series of continuous deformation tests, the flow stress and ductility were determined. The dependence of the static restoration on the pass strain, the strain rate, the temperature, and the time between passes were determined.<sup>2</sup> The influence of hard carbides particles and incipient melting on the intrinsic ductility as a function of temperature and strain rate for the A2, M2 and H13 tool steels was investigated.<sup>3</sup> The effect of temperature and strain rate on the DRX kinetics of the A2, M2, D2, W1 and K310 tool steels was analyzed. The dependence of the peak stress on the temperature and strain rate is represented very well by the hyperbolic sine Arrhenius function. The hot-deformation energies for the investigated tool steels were determined.

Večko Pirtovšek *et al.*<sup>4, 6, 13, 14</sup> used processing maps to investigate the hot workability of six different tool steel grades: A2, M2, D2, M42, 1.17 C–11.3 Cr–1.48 V–2.24 W–1.35 Mo and 1.2690 cold-work tool steel. Hot-compression tests were performed on a Gleeble 1500D thermo-mechanical simulator in the temperature range 850–1200 °C and strain-rate range 0.001–10 s<sup>-1</sup>. For increasing the hot workability of tool steels, several research steps were carried out, i.e., a determination of the appropriate casting temperature and cooling rate, soaking temperature, safe domain for hot working and chemical composition. The analysis carried out by the conditional average estimator neural network (CAE NN) revealed the influence of carbide-forming elements on the appearance of surface cracking during hot rolling. The results of the analysis were additionally supported by the THERMOCALC calculation.<sup>14</sup>

From the above-mentioned investigations it is clear that to avoid the unexpected occurrence of surface cracking during the hot deformation, due to the complexity of the hot workability of tool steels, for each type of tool steel the optimal hot-deformation conditions should be found. Namely, the safe domains for hot working for the studied tool steel are different, especially at the upper and lower limits of the safe domain for hot working.<sup>4</sup>

The 95MnWCr5 tool steel is one of the most widely used, general purpose, oil-hardening tool and die steels. Because of its high wear resistance and sufficient toughness, the 95MnWCr5 steel is used for a wide variety of tool and die applications, such as cutting and punching tools, shear knives, thread-rolling tools and measuring instruments. Furthermore, the constant pressure on the increase of its production as well as the demands on the hot rolling of the profiles with the lower final dimensions require reliable data through a wide range of hot-deformation conditions, i.e., data about its mechanical response during the hot deformation as well as about its deformation ability. In the literature, no reliable data about the hot working of 95MnWCr5 tool steel can be found. In the present work, the hot workability of the 95MnWCr5 medium-alloyed tool steel by hot-compression tests was investigated. Optimal deformation parameters of the hot working as well as constants for the hyperbolic sine Arrhenius equation were obtained. The efficiency of the power-dissipation map was used to reveal the appropriate range for the working conditions.

## 2 EXPERIMENTAL

The chemical composition of the 95MnWCr5 cold-work tool steel used in the present study is given in **Table 2**. The cylindrical specimens used for the compression tests were 10 mm in diameter and 15 mm in height and were machined from an annealed forged billet. The initial microstructure of the investigated steel is shown in **Figure 1**. The hot-compression tests were performed on a Gleeble 1500D thermal-mechanical

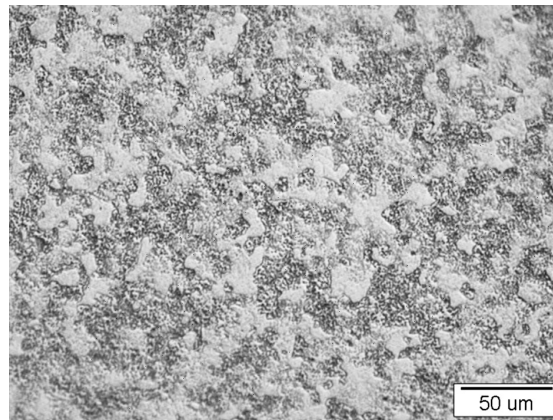


**Figure 1:** Initial microstructure of the specimen  
**Slika 1:** Mikrostruktura osnovnega stanja

simulator in the temperature range 850–1150 °C and strain rates of 0.001–10 s<sup>-1</sup>. A time course of the temperature during the hot-compression test is shown in **Figure 2**. The specimens were heated with a rate of 3 °C s<sup>-1</sup> (1) to a soaking temperature of 1200 °C, held there for 10 min (2), and then cooled with a rate of 2 °C s<sup>-1</sup> to the deformation temperature (3), held for 10 min at the deformation temperature (4), deformed with a prescribed strain rate (5), and water quenched (6) to retain the recrystallized microstructures. For the reduction of the friction and to prevent mutual welding between the specimens and the tool anvil, a Ni-based lubricant, carbon and tantalum foils were used. The temperature of the test specimens was measured by means of an S-type thermocouple welded at the centre of the specimen's surface.

The specimens were sectioned along the compression axis and prepared for optical microscopy. The ferric chloride acid solution (5 g FeCl<sub>3</sub>, 10 g HCl in 100 mL Ethanol) was used for the etching. The microstructures in the centre of the section plane were examined using a NIKON MICROPHOT-FXA optical microscope with a HITACHI HV-C20A video camera, and Soft Imaging-

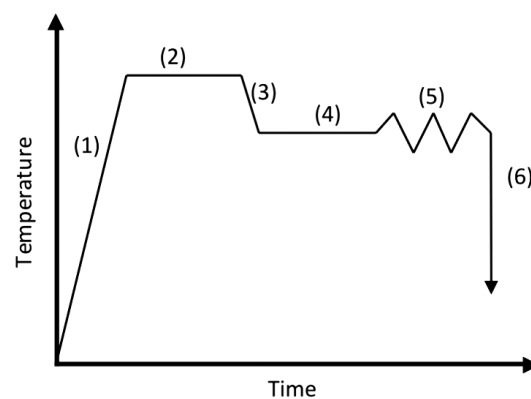


**Figure 2:** Time course of temperature during compression tests  
**Slika 2:** Shematski prikaz poteka temperature vzorcev pri preizkusu vročega stiskanja

System analysis software for the metallographic image analysis.

### 3 RESULTS AND DISCUSSION

#### 3.1 Flow curves

Representative flow curves of the 95MnWCr5 cold-work tool steel obtained from a hot-compression test are shown in **Figure 3**. The flow curves exhibit the behavior of materials that undergo dynamic recrystallization (DRX) with strain hardening to the peak stress  $\sigma_p$  and later softening towards the steady-state stress  $\sigma_{ss}$ . The onset of the  $\sigma_p$  is less obvious at the higher strain rates (**Figure 3a**). The value of the peak strains for the strain rate of  $0.001 \text{ s}^{-1}$  is 0.14 and it increases up to 0.5 at the strain rate of  $10 \text{ s}^{-1}$ . The curves in the temperature range of  $1200\text{--}1050 \text{ }^\circ\text{C}$  (**Figure 3b**) exhibit peaks and softening to a steady state, which indicates DRX behavior.

With decreasing the deformation temperature and increasing the strain rate, the values of the peak strain, peak and steady-state stress increase.

Activation energy for hot working

The activation energy of the deformation  $Q$  can be estimated using the following hyperbolic sine function:<sup>7,10,19,24</sup>

$$\dot{\epsilon} = A[\sinh(\alpha\sigma)]^n \exp\left(-\frac{Q}{RT}\right) \quad (1)$$

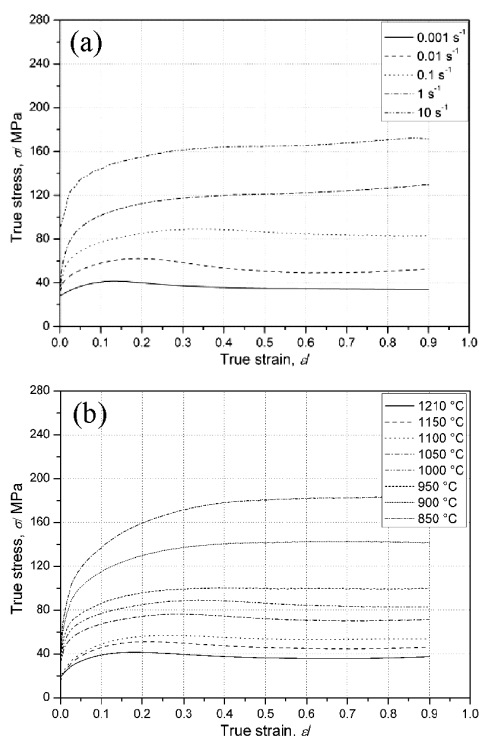


**Figure 3:** True stress / true strain curves for 95MnWCr5 **a)** at a temperature of  $1000 \text{ }^\circ\text{C}$ , **b)** at a strain rate of  $0.1 \text{ s}^{-1}$

**Slika 3:** Krivulja tečenja jekla 95MnWCr5: **a)** pri temperaturi  $1000 \text{ }^\circ\text{C}$ , **b)** pri hitrosti deformacije  $0.1 \text{ s}^{-1}$

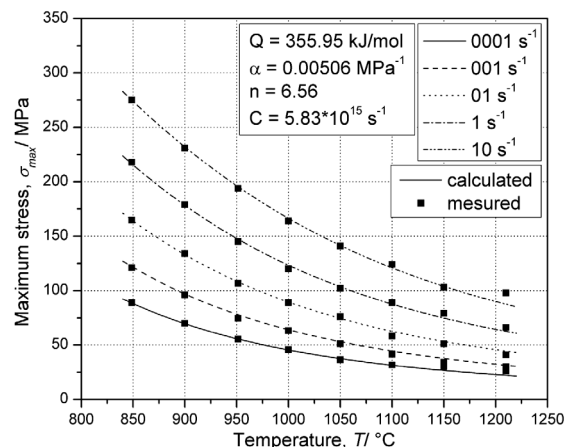


**Figure 4:** Comparison between the calculated and the measured peak stresses as a function of temperature and strain rate

**Slika 4:** Primerjava med izmerjeno in izračunano maksimalno napetostjo pri različnih temperaturah in hitrostih deformacije

where  $A$  and  $\alpha$  are material constants,  $n$  is the stress exponent,  $\dot{\epsilon}$  is the strain rate,  $\sigma$  is the flow stress,  $T$  is the absolute temperature and  $R$  is the universal gas constant. The method for calculating the parameters of Eq. 1 is described by Kugler.<sup>19</sup> The peak stresses of the flow curves were used for the calculation of the activation energy of the deformation and other constants. The comparison between the measured and calculated dependences of the peak stresses on the temperature for different strain rates is shown in **Figure 4**. A very good

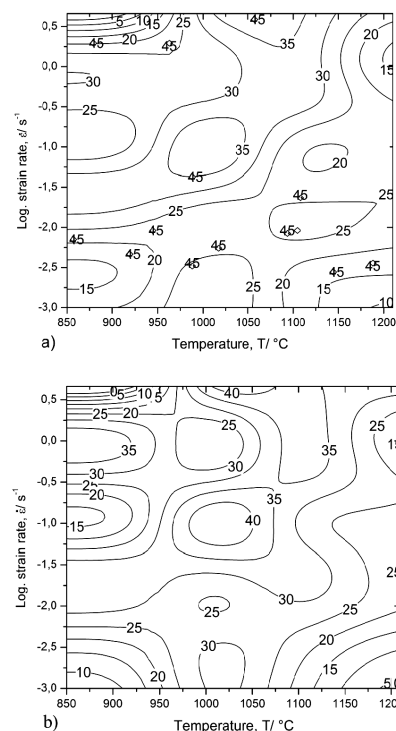


**Figure 5:** Efficiency of power-dissipation maps for 95MnWCr5 at different strains: **a)**  $\epsilon = 0.3$ , **b)**  $\epsilon = 0.9$

**Slika 5:** Učinkovitost porazdelitve energije za jeklo 95MnWCr5 pri različnih stopnjah deformacije: **a)**  $\epsilon = 0,3$ , **b)**  $\epsilon = 0,9$

fit of the data was obtained by taking  $\alpha = 0.005 \text{ MPa}^{-1}$  and  $n = 6.5$ . The value of the apparent activation energy of the deformation was  $356 \text{ kJ mol}^{-1}$ . This value for the activation energy was compared with other investigations, as summarized in **Table 1**. By comparing the results of the activation energies (**Table 1**) with the chemical composition of compared tool steels (**Table 2**), we can conclude that the obtained value of the activation energy is close to those for the A2 tool steel. Usually, this increases with the alloy contents and with the carbide volume fraction.<sup>10,12,23</sup> The activation energy for relatively pure iron is about  $280 \text{ kJ/mol}$ , and for low-carbon steel it is approximately  $300 \text{ kJ mol}^{-1}$ .<sup>24</sup>

**Table 1:** Values of the activation energy for the deformation of tool steels.

**Tabela 1:** Vrednosti aktivacijske energije za deformaciju orodnih jekel

Tool steel	$Q/(\text{kJ mol}^{-1})$	References
M2	455	C. A. C. Imbert <sup>12</sup>
D2	428	C. A. C. Imbert <sup>5</sup>
A2	399	C. A. C. Imbert <sup>12</sup>
A2*	400	T. Vecko Pirtovsek <sup>6</sup>
W1	286	C. A. C. Imbert <sup>5</sup>
K310	227	H. R. Ezatpour <sup>7</sup>
1.17C–11.3Cr–1.48V–2.24W–1.35Mo	554	T. Vecko Pirtovsek <sup>4</sup>
M35	607	P. Fajfar <sup>5</sup>
95MnWCr5	356	Current work

### 3.2 Efficiency of the power-dissipation map and the microstructure of deformed specimens

The efficiency of power-dissipation maps was developed for the optimization of the hot-deformation process of materials. They represent an explicit response of a material, in terms of microstructural mechanisms, to the imposed process parameters.<sup>1,22</sup> The basis for power-dissipation maps is the Dynamic Materials Model (DMM), where a deformed workpiece is considered to be a dissipater of the power.<sup>23</sup> The characteristics of the power dissipation through microstructural changes are expressed in terms of the efficiency of the power dissipation,  $\eta$ :

$$\eta = \frac{2m}{m+1} \quad (2)$$

$$m = \frac{\partial(\ln \sigma)}{\partial(\ln \dot{\epsilon})} \quad (3)$$

where  $m$  is the strain-rate sensitivity of the flow stress,  $\sigma$  is the flow stress and  $\dot{\epsilon}$  is the strain rate.

To obtain the optimal hot-working parameters of the investigated material, several maps for different strains must be calculated.<sup>1,13–15,22,23</sup> In the current work, the efficiency of the power-dissipation maps is presented in the temperature-strain rate plane for strains of 0.3 (**Figure 5a**) and (**Figure 5b**). The contour numbers represent the efficiency of the power dissipation  $\eta/\%$ . The domain of dynamic recrystallization at a strain of 0.3 is in the temperature range  $950\text{--}1020 \text{ }^\circ\text{C}$  and strain-rate range  $0.01\text{--}1 \text{ s}^{-1}$  with a maximum efficiency of 45 % at  $1005 \text{ }^\circ\text{C}$  and  $0.1 \text{ s}^{-1}$  (**Figure 5a**). The domain of dynamic recrystallization at a strain of 0.9 is in the temperature range  $970\text{--}1120 \text{ }^\circ\text{C}$  and strain-rate range  $0.01\text{--}1 \text{ s}^{-1}$  with a maximum efficiency of 40 % occurring at  $1005 \text{ }^\circ\text{C}$  and  $0.1 \text{ s}^{-1}$  (**Figure 5b**).

Carbide precipitates of vanadium, tungsten and chromium along austenite grain boundaries influence the ductility of the steel grade 95MnWCr5. The microstructure for the optimal range for hot working where DRX occurs (i.e.,  $1000 \text{ }^\circ\text{C}$ ,  $0.1 \text{ s}^{-1}$ ) is presented in **Figure 6a**. Deformation at higher temperatures (i.e.,  $1200 \text{ }^\circ\text{C}$ ) and the strain-rate range  $0.001\text{--}10 \text{ s}^{-1}$  causes cracks due to incipient melting at the grain boundaries (**Figure 6b**). At lower temperatures (i.e.,  $850 \text{ }^\circ\text{C}$ ) and higher strain rates (i.e.,  $10 \text{ s}^{-1}$ ), high stress values are responsible for void formation at the carbides, which leads to crack formation (**Figure 6c**). Material flow instability also occurs at strain rate of  $1 \text{ s}^{-1}$  in the form of twinning (**Figure 6d**).

Thus, all the areas with too high or too low values of efficiency of power dissipation should be avoided during hot deformation, if possible. On the other hand, hot deformation in areas with values in the range 30–40 % should be intensified.

As mentioned in the introduction, the hot deformability of each of the individual tool steels is not a

**Table 2:** Chemical composition of tool steels in mass fractions, w/%

**Tabela 2:** Kemijska sestava orodnih jekel v masnih deležih, w/%

	C	Cr	Ni	Si	Mn	Mo	V	W	Co
M2	0,84	4.00		0.30	0.25	5,00	1.90		
D2	1.45	11.09	0.21	0.24	0.38	0.72	0.71		
A2	1.00	5,00		0.30	0.70	1.15	0.30		
A2*	0.99	4.95	0.15	0,28	0,48	0,94	0,18	0,08	
W1	1.03	0.07	0.14	0.23	0.31	0.03			
K310	0.83	1.9		0.45	0.40	0.30			
1.17C–11.3Cr–1.48V–2.24W–1.35Mo	1.17	11.3		0.24	0.26	1.35	1.48	2.24	
M35	0.91	4.15				4.7	2.1	6.3	4.75
95MnWCr5	0.95	0.48		0.25	1.20	0.94	0.13	0.55	

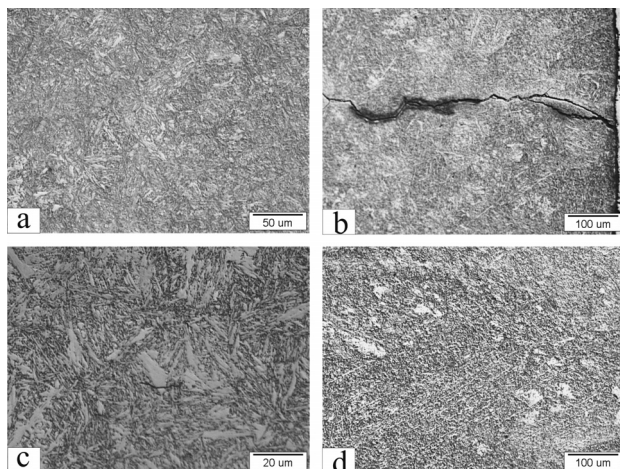


**Figure 6:** Microstructure of 95MnWCr5: a)  $T = 1000\text{ }^{\circ}\text{C}$ ,  $\dot{\epsilon} = 0.1$ , b)  $T = 1200\text{ }^{\circ}\text{C}$ ,  $\dot{\epsilon} = 1.0$ , c)  $T = 1150\text{ }^{\circ}\text{C}$ ,  $\dot{\epsilon} = 10.0$ , d)  $T = 850\text{ }^{\circ}\text{C}$ ,  $\dot{\epsilon} = 1.0$ ,  
**Slika 6:** Mikrostruktura jekla 95MnWCr5: a)  $T = 1000\text{ }^{\circ}\text{C}$ ,  $\dot{\epsilon} = 0.1$ , b)  $T = 1200\text{ }^{\circ}\text{C}$ ,  $\dot{\epsilon} = 1.0$ , c)  $T = 1150\text{ }^{\circ}\text{C}$ ,  $\dot{\epsilon} = 10.0$ , d)  $T = 850\text{ }^{\circ}\text{C}$ ,  $\dot{\epsilon} = 1.0$

constant value. A variation in the processing parameters as well as in the chemical composition can lead to widening/narrowing of the safe/unsafe domain for hot working.

#### 4 CONCLUSION

The hot workability of 95MnWCr5 cold-work tool steel was investigated by means of hot-compression tests. The tests were conducted in the temperature range 850–1150 °C in intervals of 50 °C and in the strain rate range 0.001–10 s<sup>-1</sup>. A Gleeble 1500D thermo-mechanical simulator was applied. The following conclusions can be drawn from this investigation:

The flow curves exhibit the behavior of materials that undergo dynamic recrystallization DRX with strain hardening to the peak stress  $\sigma_p$  and then work softening towards a steady-state stress  $\sigma_{ss}$ . The onset of  $\sigma_p$  is less obvious at higher strain rates and lower temperatures.

The apparent activation energy  $Q$  for hot deformation has a value of 356 kJ mol<sup>-1</sup>, and the stress exponent has a value of 6.5.

The optimum domain for hot working is in the temperature range 960–1050 °C, and a strain rate of 1.0 s<sup>-1</sup> with a peak efficiency of power dissipation  $\eta$  of about 30–40 % was found.

The domain of dynamic recrystallization at a strain of 0.9 is in the temperature range 970–1120 °C and strain rate range 0.01–1 s<sup>-1</sup> with a maximum efficiency of 40 % occurring at 1005 °C and 0.1 s<sup>-1</sup>.

The material exhibits flow instability at temperatures of 850 °C and 1200 °C for the entire range of the strain rate, and at the strain rate of 10 s<sup>-1</sup> for the entire range of temperatures.

#### 5 REFERENCES

- <sup>1</sup> Y. V. R. K. Prasad, S. Sasidhara, Hot Working Guide: A Compendium of Processing Maps, ASM International, Materials Park, OH, (1977), 543
- <sup>2</sup> G. Kugler, R. Turk, Acta Materialia, 52 (2004), 4659–4668
- <sup>3</sup> T. Večko - Pirtovšek, I. Peruš, G. Kugler and M. Terčelj, ISIJ International, 49 (2009) 3, 395–401
- <sup>4</sup> T. Večko - Pirtovšek, G. Kugler, M. Godec, M. Terčelj, Materials Characterization, 62 (2011), 189–197
- <sup>5</sup> P. Fajfar, D. Bombač, B. Markoli, RMZ – Materials and Geoenvironment, 57 (2010) 2, 159–164
- <sup>6</sup> T. Večko - Pirtovšek, I. Peruš, G. Kugler, R. Turk, M. Terčelj, Metalurgija, 47 (2008) 4, 307–311
- <sup>7</sup> C. Imbert, N. D. Ryan, H. J. McQueen, Metallurgical Transaction A, 15A (1984), 1855–1864
- <sup>8</sup> C. A. C. Imbert, H. J. McQueen, Canadian Metallurgical Quarterly, 40 (2001), 235–244
- <sup>9</sup> C. A. C. Imbert, H. J. McQueen, Materials Science and Engineering A, 313 (2001), 104–116
- <sup>10</sup> C. A. C. Imbert, H. J. McQueen, Materials Science and Technology, 16 (2000), 524–531
- <sup>11</sup> C. A. C. Imbert, H. J. McQueen, Materials Science and Engineering A, 313 (2001), 88–103
- <sup>12</sup> H. R. Ezatpour, S. A. Sajjadi, M. Haddad Sabzevar, Materials Science and Engineering A, 527 (2010), 1299–1305
- <sup>13</sup> T. Večko - Pirtovšek, G. Kugler, M. Godec, R. Turk, M. Terčelj, RMZ – Materials and Geoenvironment, 53 (2006), 1, 93–101
- <sup>14</sup> T. Večko - Pirtovšek, M. Fazarinc, G. Kugler, M. Terčelj, RMZ – Materials and Geoenvironment, 55 (2008), 2, 147–162
- <sup>15</sup> G. Roberts, G. Krauss, R. Kennedy, Tool Steels, ASM International, (1998), 364
- <sup>16</sup> F. Tehovnik, B. Arzenšek, B. Arh, Metalurgija, 47 (2008) 2, 75–79
- <sup>17</sup> F. Tehovnik, F. Vodopivec, R. Celin, B. Arzenšek, J. Gontarev, Mater. sci tehnol., 27 (2011) 4, 774–782
- <sup>18</sup> A. Kveder, Železarski zbornik 10 (1976) 4, 179–192
- <sup>19</sup> G. Kugler, M. Knap, H. Palkowski, R. Turk, Metalurgija, 43 (2004) 4, 267–272
- <sup>20</sup> C. A. C. Imbert, H. J. McQueen, Materials Science and Engineering A, 313 (2001), 88–103
- <sup>21</sup> P. V. Sivaprasad *et al*, Journal of Materials Processing Technology, 132 (2003), 262–268
- <sup>22</sup> Y. V. R. K. Prasad, H. L. Gegel, S. M. Doraivelu, J. C. Malas, J. T. Morgan, K. A. Lark, D. R. Baker, Metallurgical Transaction A, 15A (1984), 1883–1883
- <sup>23</sup> M. M. Myshlyayev, H. J. McQueen, A. Mwembela, E. Konopleve, Materials Science and Engineering A, 337 (2002), 121–133
- <sup>24</sup> H. J. McQueen, S. Yue, N. D. Ryan, E. Fry, Journal of Materials Processing Technology, 53 (1995), 293–310



## LIFETIME EVALUATION OF A STEAM PIPELINE USING NDE METHODS

### OCENA PREOSTALE TRAJNOSTNE DOBE PAROVODA Z UPORABO NEPORUŠITVENIH PREISKAV (NDE)

**Fevzi Kafexhiu, Jelena Vojvodič Tuma**

Institute of Metals and Technology, Lepi pot 11, 1000 Ljubljana, Slovenia  
fevzi.kafexhiu@imt.si

*Prejem rokopisa – received: 2010-08-24; sprejem za objavo – accepted for publication: 2011-02-15*

Before its shutdown, the steam pipeline made from X20CrMoV121 steel in the Power Plant Toplarna – Ljubljana operated at 530 °C and 95 bar for 150 000 h. A non-destructive evaluation (NDE) of the microstructure using the replica method and hardness measurements on pipeline bends and welded joints with the aim to evaluate for possible damage due to creep deformation was applied. The hardness of the different zones of the welded joints, base material, heat-affected zone and the weld material itself was appropriate and corresponded to the tensile strength in the range required by the standards. A martensitic appearance in all the observed locations was noticeable. Micro-voids that arise due to creep deformation along the former austenite grain boundaries and along the martensite lamellas on the inspected sites were not observed. According to the VGB<sup>1</sup> classification, the steel corresponds to the 2b class.

Keywords: steel X20CrMoV121, steam pipelines, life time, micro-voids, NDE methods

Ob zaustavitvi je bil parovod v Termoelektrarni-Toplarni Ljubljana v obratovanju že 150 000 h pri tlaku 95 bar in temperaturi pare 530 °C. Parovod je izdelan iz jekla X20CrMoV121. Na cevnih kolenih in zvarjenih spojih parovoda smo naredili neporušitvene preiskave (NDE) mikrostrukture po metodi replik in meritve trdote za oceno stanja parovoda ter ocenili morebitne poškodbe zaradi deformacije z lezenjem. Trdota različnih delov zvara, osnovnega materiala, toplotno vplivanega področja in vara je ustrezna in ustreza natezni trdnosti, ki je v mejah, določenih po standardu. Martenzitni habitus je na vseh mestih izrazil. Mikropore, ki nastanejo zaradi deformacije z lezenjem po mejah prvotnih avstenitnih zrn in po martenzitnih lamelah, na pregledanih mestih nismo opazili. Po klasifikaciji VGB<sup>1</sup> ustreza jeklo razredu 2b.

Ključne besede: jeklo X20CrMoV121, parovodi, preostala trajnostna doba, mikropore, neporušitvene preiskave (NDE)

## 1 INTRODUCTION

High-temperature and high-pressure components in large-scale steam generating power plants are manufactured from creep-resistant steels. Steam pipelines, as important parts of these components, are required to operate for many years under severe conditions of temperature and stress; therefore, they are usually designed for a certain lifetime, for example,  $10^5$  or  $2 \times 10^5$  h. However, because of uneven distribution of stresses, the lifetime of different elements is not the same.<sup>2</sup> The microstructure of materials operating under such conditions changes with time and accelerates the different mechanisms of degradation of these materials, such as creep, fatigue, thermal fatigue, creep-fatigue, progressive embrittlement, corrosion/oxidation, etc., of which the most important is the creep deformation. The damage caused by creep deformation is permanent.<sup>3</sup> The final evidence for the development of creep damage during service is the initiation and growth of discrete cracks, either by creep processes alone or by creep fatigue interactions. These may form either as a single crack at stress-concentrating features or as the final phase of more generalized damage, and both of them ultimately result in creep failure.<sup>4</sup> It is important to mention that the creep deformation is far from homogenous, also on the microstructural scale. One manifestation of this is the

formation of cavities at the grain boundaries between differently oriented crystals.<sup>5</sup> In some steels the grain-boundary cavitations develop early in life, progressing steadily through the stages of growth and linkage into microcracks before reaching the failure point. This behavior is generally characteristic of low-ductility steels, the cavities forming preferentially at grain boundaries orientated normal to the maximum principal stress on particles, such as sulfides or carbides.<sup>6,7</sup> Conversely, higher ductility materials may not exhibit detectable cavitations until a late stage in life and the cavities or voids may form intragranularly or at grain boundaries, supporting the maximum shear stress. For example, in the low-alloy steels and X20CrMoV121, the cavities become visible ( $N \approx 50\text{--}100 \text{ mm}^{-2}$ ) when a life fraction of between 0.3 and 0.55 have been consumed. But this usually differs in the case of welded joints. The lower residual creep ductility of the heat-affected zone (HAZ) and the creep rate of the surrounding base materials dictates the development rate of cavities and microcracks in the HAZ.<sup>8</sup> In these cases also premature damage in the form of cracks, which are parallel to the weld, may arise. There are two reasons for this: one is the increase of the stress due to the welding, the other one is the initial microstructure that influences the creep resistance of the steel.<sup>2</sup> In either case the detection of cavities as early as

possible is essential and this has become one of the major tools in any life-management program.<sup>4</sup>

The severity of creep cavitation and its effect on remaining life has been studied extensively and both qualitative and quantitative procedures have been variously developed or proposed. The semi-quantitative procedure proposed by Neubauer<sup>9,10</sup> is the best known and remains the basis for most procedures in use today. The degree of cavitation is described by five "damage parameters" ranging from "undamaged" through to "macro-cracked". The damage parameters are then related to the stage that the material has reached on a classic primary-secondary-tertiary creep curve and on the basis of these recommendations, future plant actions are made (**Figure 1**).<sup>2,4,11</sup> Similar procedures are incorporated in European guidelines for in-service damage assessment.<sup>12,13</sup> However, because of the high conservatism included into each of these theories, they are actually used as monitoring techniques, rather than life-prediction methods.<sup>14</sup>

The metallographic replication technique together with other conventional, non-destructive evaluation (NDE) methods form an important part of the base-line and progressive inspection philosophy of HTP components.<sup>8</sup> The replication technique is carried out at certain intervals on components that operate in such conditions that damage due to the creep deformation is present.<sup>2,14</sup> The initial damage due to the creep deformation always arises on the outer surface of steam pipelines and it is impossible to detect it with other non-destructive investigations because they are at the microscopic scale. Despite the relatively small area, the replicas are representative if they are taken from regions of components where stresses, deformations and temperatures are the

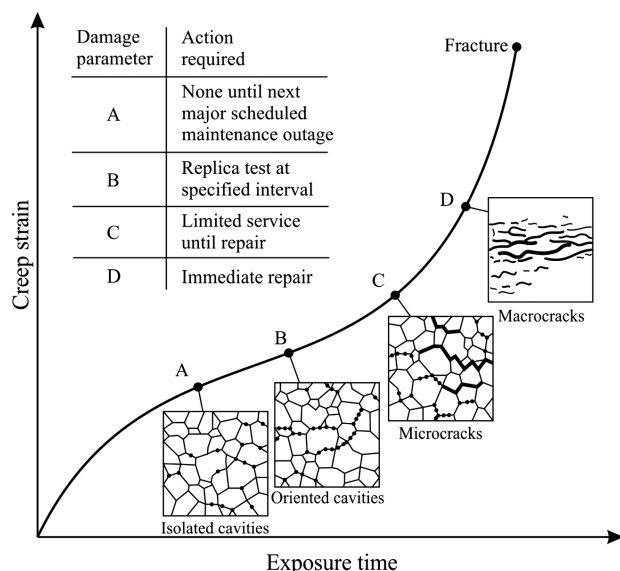


**Figure 1:** Degradation of steel depending on the duration of the creep deformation I

**Slika 1:** Degradacija jekla v odvisnosti od trajanja deformacije z lezenjem I

highest. Therefore, good experience is very important in these investigations.<sup>15</sup>

Along with the replication technique, in-situ hardness measurements can provide information of great importance regarding the actual condition of materials in HTP components. The hardness of all creep-resistant steels operating in the creep range is a function of time, temperature, and stress. The relative simplicity of hardness measurements on service components has promoted interest in using these for remnant-life assessment purposes, either as a means of determining or confirming the operating temperature, as a qualitative indicator of a material's condition, or in the extreme, as a means of a direct estimation of the remaining creep life.<sup>4</sup>

In the present work, both the metallographic replication technique and in-situ hardness measurements of pipeline bends and T-fittings as well as welded joints between them and the straight parts of steam pipelines were carried out. The aim was to evaluate their condition for possible damage due to creep deformation. Due to the microstructural features and different hardnesses on different regions of the welded joints, they are less resistant to creep deformation. For this reason, the inspection of welded joints is of particular importance. The pipeline is made of X20CrMoV121 steel. Before the shutdown, the pipeline was subjected to operating conditions of 530 °C and 95 bar for 150 000 h. The dimensions of the pipeline are 323.9 mm × 20 mm.

The investigation consisted of:

- preview and study of the pipeline's plan
- visual inspection of the pipeline
- replication on the bends
- replication on the welded joints
- hardness measurements on both the bends and the welded joints
- microstructural investigation using light microscopy

Based on the investigation carried out, the evaluation of the pipeline's condition according to the VGB<sup>1</sup> criteria (microstructural features, damages due to the creep deformation) was carried out.

## 2 EXPERIMENTAL

Microstructural investigations and hardness measurements were performed on the outer part of five bends, on welded joints between the bends and the straight parts of pipelines, and also on the base material and the welded joints of T-fittings. On three regions of welded joints, i.e., base material, heat-affected zone (HAZ) and the weld itself, the replication was performed.

Prior to the replication, the surface of chosen regions was properly prepared for this purpose. First, the surface was properly cleaned and dried with hot air. After that, the surface was ground using fine abrasive paper, in a depth of less than 0.2 mm. Low hand-pressure was applied during this step, in order to prevent any overheating or cold hardening of the material on the

surface. This procedure consisted of consecutive short grinding steps, applied in directions perpendicular to each other. After each of these steps, we had to remove the remains of the grinding process. After the grinding, the surface was carefully polished using a "Muvi-pol-3" electrolytic polisher, followed by the process of cleaning with alcohol and drying. The next step was the etching of the surface, also followed by cleaning and drying. In order to make sure that the surface is properly prepared, we used a portable optical microscope to observe the condition of this surface. Finally, a special solvent was overspread on the transparent replication foil of thickness 0.06 mm, and the foil was placed on the surface and pressed for approximately 60 s. The replicas were observed using a "Nikon Microphot FXA" optical microscope with a "Hitachi HV-C20A 3CCD" video camera at magnifications of 100-times and 200-times.

Using a "InstronDynaTestor" portable hardness-measuring instrument, we performed hardness measurements on the same locations where the replicas were taken. Measurements were performed at 5 different locations for each prepared surface by applying a load of approximately 20 N. The average of 5 measurements was taken as the actual value of the hardness. The instrument we used in this case gave us the possibility that through hardness measurements we could directly determine the corresponding values of the tensile strength.

### 3 RESULTS AND DISCUSSION

The microstructure on the outer side of the bends is a highly tempered martensite. A martensitic appearance in all the investigated locations is noticeable. We observed a few regions with numerous cavities or micro-voids without preferred orientation, which arose due to the creep deformation. The microstructural features are the same in all the observed locations (**Figures 2 and 3**).

The microstructure of the tempered martensite in the base material is the same as in the pipeline bends. The

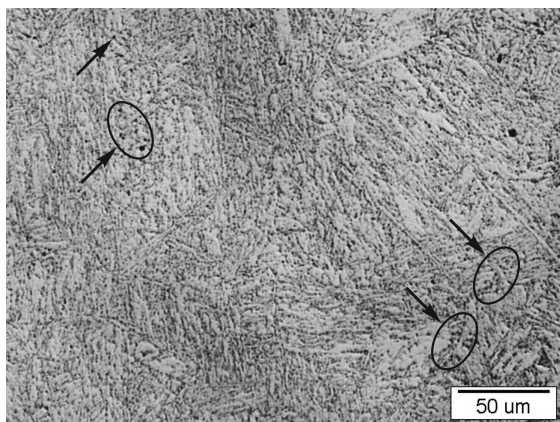


**Figure 2:** Microstructure of steel in the bend 1  
**Slika 2:** Mikrostruktura jekla na kolenu 1

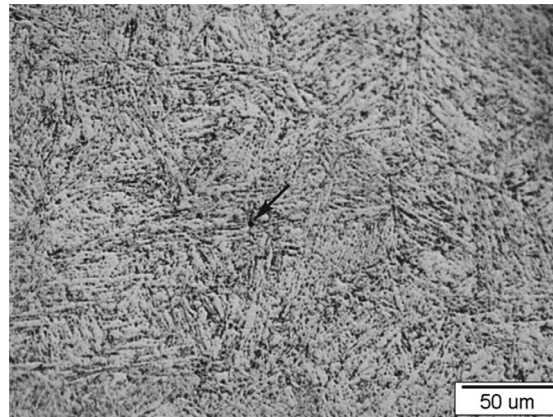


**Figure 3:** Microstructure of steel in the bend 5  
**Slika 3:** Mikrostruktura jekla na kolenu 5

microstructure of the welds is also a tempered martensite; however, it was observed that the size of the former austenite grains was larger compared to those of the base material. Because of welding effects, the tempered martensite microstructure in the transition region between the weld and the heat-affected zone is strongly blurred. In the heat-affected zone and in the weld material, which are loaded with internal steam pressure, stresses due to the welding and with additional static and dynamic loads during the operation (temperature fluctuations, bending moments, vibrations, etc.), we also observed a few micro-voids. The microstructural features of the welded joints are shown in **Figures 4, 5 and 6**.

The microstructural characteristics in the base material and in the welded joints of the T-fitting are the same as in the pipelines (**Figures 7, 8 and 9**). The base material has an appropriate microstructure of tempered martensite. In the microstructure of tempered martensite of the weld and the heat-affected zone there are a few regions with micro-voids, which as in the case of bends, have no preferred orientation.

The average hardness values measured using a portable instrument on the base material and on welded

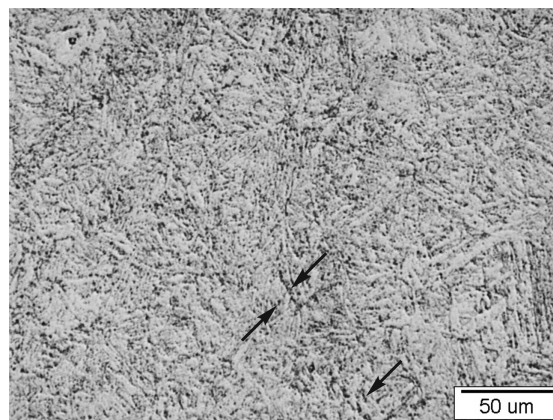


**Figure 4:** Microstructure of the base material in the welded joint of the bend 1  
**Slika 4:** Mikrostruktura osnovnega materiala ob zvaru na kolenu 1

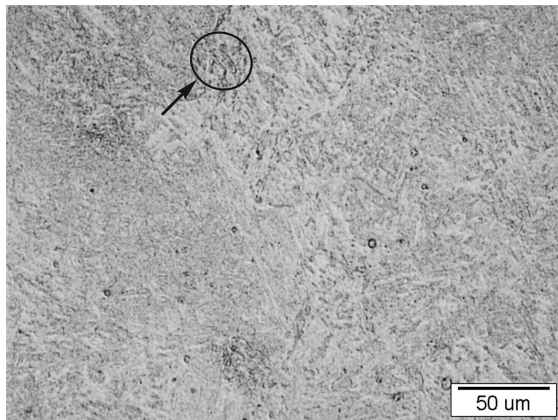


**Figure 5:** Microstructure of the weld in the welded joint of bend 1  
**Slika 5:** Mikrostruktura vara ob zvaru na kolenu 1

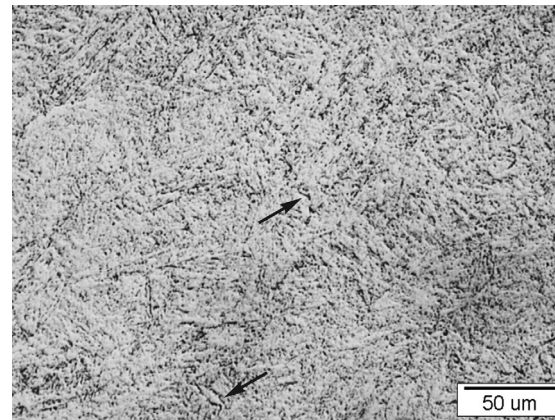


**Figure 8:** Microstructure of the weld in the welded joint of the T-fitting  
**Slika 8:** Mikrostruktura vara ob zvaru na T-kosu

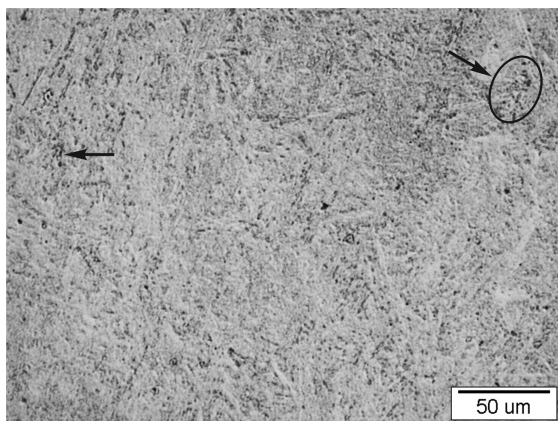


**Figure 6:** Microstructure of the HAZ in the welded joint of bend 1  
**Slika 6:** Mikrostruktura TVP ob zvaru na kolenu 1



**Figure 9:** Microstructure of the HAZ in the welded joint of the T-fitting  
**Slika 9:** Mikrostruktura TVP ob zvaru na T-kosu

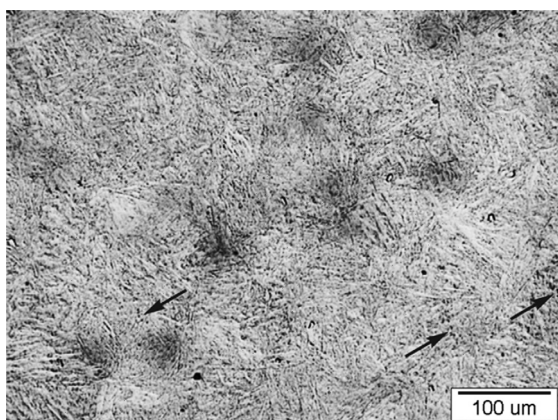


**Figure 7:** Microstructure of the base material in the welded joint of the T-fitting  
**Slika 7:** Mikrostruktura osnovnega materiala ob zvaru na T-kosu

joints are given in **Table 1**. The hardnesses of the base material, the heat-affected zone and the welds are appropriate. The lowest hardness of the material, namely 231 HV, corresponds to tensile strength of 741 N/mm<sup>2</sup>, whereas the highest value, 245 HV, corresponds to tensile strength of 785 N/mm<sup>2</sup>. These values, compared

**Table 1:** Average values of HV hardness for base material and welds, as well as the lowest and the highest values measured on the heat-affected zone

**Tabela 1:** Povprečne vrednosti trdote HV osnovnega materiala in varov ter najnižje in najvišje vrednosti, izmerjene v toplotno vplivanem področju

Elbow	Base material	Weld	Heat-affected zone
1	236 ± 7.9	264 ± 4.6	248–280
2	236 ± 3.9	275 ± 6.0	269–279
3	231 ± 5.7	281 ± 4.9	253–289
4	241 ± 8.5	287 ± 6.8	264–284
5	240 ± 7.3	269 – 279	257–286
T-fitting (A)	245 ± 9.4	248 ± 8.9	241–264
T-fitting (B)	239 ± 4.6	267 ± 6.2	263–278

to the values of the tensile strength of the steel X20CrMoV121 determined by the standard DIN 17 175 (690–840 N/mm<sup>2</sup>), are within the given limits.

For both bends and T-fittings, having minor non-localized micro-void damages, according to the VGB<sup>1</sup> classification, the steel corresponds to the 2b class. In addition, considering the residual life of these elements

under given service conditions and their current state (microstructure and hardness/tensile strength) they can continue to operate for an additional 45 000 h. It is recommended that a lifetime assessment should be taken after 25 000 h service exposure for safety reasons.

#### 4 CONCLUSIONS

Microstructural investigations using non-destructive evaluation (NDE) methods, i.e., the replication technique and hardness measurements with a portable instrument, were carried out. These investigations were performed on the outer part of five bends, on welded joints between the bends and the straight parts of pipelines, and also on the base material and the welded joints of T-fittings.

The microstructure of the base material, the welds and the heat affected-zone is tempered martensite. The martensitic appearance is noticeable. Numerous microvoids or cavities with no preferred orientation, which arise due to the creep deformation along the former austenite grain boundaries and along the martensite lamellas on the inspected sites were observed. For both bends and T-fittings, having minor, non-localized, micro-void damage, according to the VGB<sup>1</sup> classification, the steel corresponds to the 2b class.

The hardness of the bulk material, welds and the heat-affected zone is appropriate. The lowest hardness of the material, i.e., 231 HV, corresponds to the tensile strength of 741 N/mm<sup>2</sup>, whereas the highest value, 245 HV, corresponds to the tensile strength of 785 N/mm<sup>2</sup>. These values, compared to the values of the tensile strength of the steel X20CrMoV121, determined by the standard DIN 17 175 (690–840 N/mm<sup>2</sup>), are within acceptable limits. The mechanical properties of the initial state of the steel are unknown, and thus we cannot define the reduction of the mechanical properties based on 150 000 h of operation of the pipeline.

Considering the residual life of these elements under given service conditions and their current state (microstructure and hardness/tensile strength) it was concluded that these elements are in a good condition and can

continue to operate for an additional 45 000 h. It is recommended that a lifetime assessment, including more detailed investigations, should be performed after 25 000 h of service exposure for safety reasons.

#### 5 REFERENCES

- <sup>1</sup> VGB: Guideline for the Assessment of Microstructure and Damage Development of Creep Exposed Materials for Pipes and Boiler Components, Report VGB-TW 507, Germany 1992
- <sup>2</sup> F. Vodopivec: O poškodbah jekla v parovodih in metodah za njihovo opredelitev, *Železarski zbornik*, 24 (1990) 3, 145–152
- <sup>3</sup> J. Vojvodič - Gvardjančič, F. Vodopivec: Assessment of Residual Life of Steam Pipelines, *Kovine Zlit. Tehnol.*, 29 (1995) 1/2, 95–99
- <sup>4</sup> A. Saxena: *Comprehensive Structural Integrity*, Volume 5. Creep and high-temperature failure, Elsevier, Georgia Institute of Technology, USA, 2003
- <sup>5</sup> H. K. D. H. Bhadeshia, A. Strang, D. J. Gooch, Ferritic power plant steels: remnant life assessment and approach to equilibrium, *International Materials Reviews*, 43 (1998) 2, 45
- <sup>6</sup> C. J. Middleton, Reheat cavity nucleation and nucleation control in bainitic creep-resisting low-alloy steels: Roles of manganese sulphide, residual, and sulphur-stabilizing elements, *Metal Science*, 15 (1981), 154–167
- <sup>7</sup> B. J. Cane, C. J. Middleton: Intergranular creep cavity formation in low-alloy bainitic steels. *Metal Science*, 15 (1981), 295–301
- <sup>8</sup> H. Ferdinand van Zyl: An overview of material's engineering and research activities in TSI (ESKOM) with respect to life assessment and integrity of high temperature and stressed components, VGB-ESKOM International Materials Conference, Pretoria, South Africa, 2000
- <sup>9</sup> B. Neubauer, U. Wedel: *Advances in life prediction methods*, American Society of Mechanical Engineers, New York, 1983, 307–314
- <sup>10</sup> B. Neubauer: Creep and fracture of engineering materials and structures, *Proceedings of the 2<sup>nd</sup> International Conference*, Swansea, 1984, 1217–1226
- <sup>11</sup> R. P. Skelton: Low Cycle Fatigue, *Materials Science and Engineering*, 35(1978), 287–298
- <sup>12</sup> P. Auerkari, J. Salonern, K. Borgreen: Towards unified evaluation of replica inspections for power plant applications, *Proceedings of the 6<sup>th</sup> International Conference on Creep and Fatigue*, Institute of Mechanical Engineering, London, 1996, 905–928
- <sup>13</sup> Ch. Laire, M. Eyckmans: Evaluating the condition and remaining life of older power plants, *VGB PowerTech*, 10 (2001), 2, 98–102
- <sup>14</sup> D. Kmetič, J. Vojvodič - Tuma, B. Arzenšek, M. Dvoršek, J. Lenart: Damage to steam pipe made of 14 MoV 6 3 steel, *Mater. Tehnol.*, 37 (2003) 3/4, 155–160



## THE INFLUENCE OF THE CHEMICAL COMPOSITION OF STEELS ON THE NUMERICAL SIMULATION OF A CONTINUOUSLY CAST SLAB

### VPLIV KEMIČNE SESTAVE JEKEL NA NUMERIČNO SIMULACIJO KONTINUIRNO LITE PLOŠČE

**Josef Stetina, Frantisek Kavicka**

Brno University of Technology, Technicka 2, 616 69 Brno, Czech Republic.  
stetina@fme.vutbr.cz

*Prejem rokopisa – received: 2010-10-20; sprejem za objavo – accepted for publication: 2011-02-21*

The chemical composition of steels has a significant influence on the actual concasting process, and on the accuracy of its numerical simulation and optimization. The chemical composition of steel affects the thermophysical properties (heat conductivity, specific heat capacity and density in the solid and liquid states) and often requires more time than the actual numerical calculation of the temperature fields of a continuously cast steel slab. Therefore, an analytical study of these thermophysical properties was conducted. The order of importance within the actual process and the accuracy of the simulation were also determined. The order of significance of the chemical composition on the thermophysical properties was determined with respect to the metallurgical length. The analysis was performed by means of a so-called calculation experiment, i.e., by means of the original numerical continuously cast model developed by the authors of this paper. It is convenient to conduct such an analysis in order to facilitate the simulation of each individual case of continuously cast steel, thus enhancing the process of optimization.

Keywords: concast slabs, chemical composition, numerical model, solidification

Kemična sestava jekla ima pomemben vpliv na dejansko kontinuirno lije ter na točnost numerične simulacije in optimizacije. Kemična sestava jekla vpliva na termične lastnosti (na toplotno prevodnost, specifično toploto in gostoto v trdnem in tekočem stanju) pogosto zahteva več časa kot dejansko numerični izračun temperaturnega polja kontinuirno lite jeklene plošče. Zato je bila izvedena analitična študija teh termofizikalnih lastnosti. Zaporedja pomembnosti samega procesa in natančnost simulacije so bili tudi določeni. Vrstni red pomena kemijske sestave na termofizikalne lastnosti je bil določen glede na metalurško dolžino. Analiza je bila izvedena s tako imenovanim poskusom izračuna, tj. z uporabo prvotnega numerično kontinuirnega litega modela avtorjev tega članka. To je priročno za izvajanje teh analiz, da bi se olajšala simulacija za vsak posamezni primer kontinuirnega litja, kar spodbujaja proces optimizacije.

Ključne besede: kontinuirno uliti drogovi, nihajoče oznake, numerični model, strjevanje

## 1 INTRODUCTION

The production of steels, alloys and metallurgical products in general is constantly developing. Materials with high utility parameters are more in demand and traditional production is being replaced by better quality steel. More and more sophisticated aggregates using more sophisticated technological procedures are being implemented. In order to maintain competitiveness, diversify production and expand into other markets, it is necessary to monitor the technological development.

In the case of concasting, it is not possible to fulfil these requirements without the application of models of all caster processes dependent on thermal-mechanical relationships. These models can be applied both off-line and on-line. An off-line model is the one where the calculations typically take a longer time than the actual casting process. An on-line model runs in real time – taking the data directly from the operation – and its calculation runs in real time.

These models will support the design of new and the redesign of old machines, they will facilitate the

identification and quantification of any potential defects and the optimization of the various operational conditions in order to increase the productivity and minimize the occurrence of defects. The process of the solidification of concast steel is influenced by many factors and conditions, among which are the following:

- Complete turbulent transient flow within a comprehensive geometry (input jet and liquid metal in the slab).
- Thermodynamic reactions between the casting powder and the solidifying slab.
- Heat transfer between the liquid and solid powder on the surface of the slab.
- Dynamic movement of the liquid steel inside the mould on the liquid-phase–mushy-zone interface, including the influence of gravity, oscillations and the casting speed.
- Heat transfer in a superheated melt considering the turbulent flow.
- Transition (mixture) composition of the steel during the change of class.

- Heat and mechanical interaction in the area of the meniscus between the solidifying meniscus, the solid powder and the liquid steel.
- Heat transfer from the surface of the solidified shell into the space between the shell and the working surface of the mould (including the layers of the casting powder and the air gap).
- Mass transfer of the powder during its vertical movement through the gap between the shell and the mould.
- Contact of the solidified slab with the mould and support rollers.
- The formation of crystals inside the melt.
- The process of micro-segregation and macro-segregation.
- The occurrence of shrinkages as a result of temperature contraction of the steel and the initialization of internal stresses.
- The occurrence of stress and strain in the solidified shell as a result of external influences such as the friction inside the mould, bulging between rollers, rolling, temperature stress and strain.
- The occurrence of cracks as a result of internal stresses.
- The flow of steel as a result of the electromagnetic stirring and the influence of the stirring on the temperature field and the primary structure.
- The occurrence of stress and strain as a result of unbending of the inside the segments or in the rolling mill.
- Radiation between the various surfaces.
- Cooling as a result of convection beneath the water or the water-air jets.

With respect to the complexity of the investigation into the influence of all of the above-mentioned factors, it is not possible to develop a mathematical model that would cover all of them. It is best to group them according to the three main types of influence:

- Heat and mass transfer
- Mechanical
- Structural

The primary and deciding one is the influence of heat and mass transfer because it is the temperature field that gives rise to the mechanical and structural influences. The development of a model of the temperature field (of a slab) with an interface for providing data for mechanical stress and strain models and structure models is therefore a top-priority task <sup>1</sup>.

## 2 MODEL OF THE TEMPERATURE FIELD OF A SLAB

The 3D model was first designed as an off-line version and later as an on-line version so that it could work in real time. After corrections and testing, we are working towards its implementations on any caster

thanks to the universal nature of the code. The numerical model takes into account the temperature field of the entire slab (from the meniscus of the level of the melt in the mould to the cutting torch) using a 3D mesh containing more than a million nodal points.

The solidification and cooling of a concast slab is a general problem of 3D transient heat and mass transfer. If the heat conduction within the heat transfer is decisive, the process is described by the Fourier-Kirchhoff equation (Equation 1). It describes the temperature field of the solidifying slab in all three of its states: at the temperatures above the liquidus (i.e., the melt), within the interval between the liquidus and solidus (i.e., in the mushy zone) and at the temperatures below the solidus (i.e., the solid state). In order to solve these it is convenient to use the explicit numerical method of finite differences. The numerical simulation of the release of latent heats of phase or structural changes is carried out by introducing the enthalpy function dependent on the temperature  $T$ , preferably in the form of enthalpy related to the unit volume  $H_v$ . The latent heats are contained here (Figure 1). After the automated generation of the mesh (pre-processing) ties on the entry of the thermophysical material properties of the investigated system, including their dependence on temperature – in the form of tables or using polynomials. They are namely the heat conductivity  $k$ , the specific heat capacity  $c$  and the density  $\rho$  of the cast metal.

The temperature distribution in the slabs described by the enthalpy balance equation

$$\frac{\partial H_v}{\partial \tau} = \frac{\partial}{\partial x} \left( k \cdot \frac{\partial T}{\partial x} \right) + \frac{\partial}{\partial y} \left( k \cdot \frac{\partial T}{\partial y} \right) + \frac{\partial}{\partial z} \left( k \cdot \frac{\partial T}{\partial z} \right) + \left( u \cdot \frac{\partial H_v}{\partial x} + v \cdot \frac{\partial H_v}{\partial y} + w \cdot \frac{\partial H_v}{\partial z} \right) \quad (1)$$

This simplified equation (1), suitable for application on radial-casters with a great radius, where only the speed (of the movement of the slab) component  $w$  in the  $z$ -direction is considered, is:

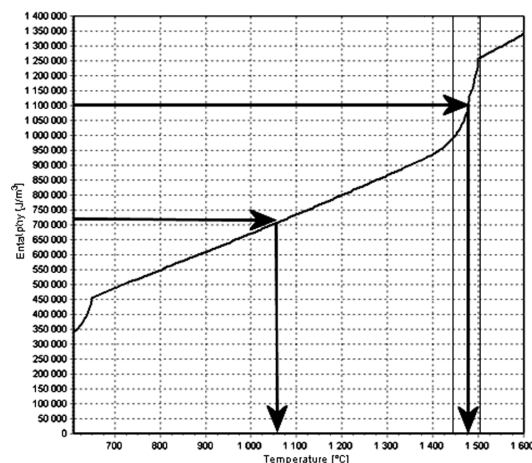


Figure 1: Enthalpy function of typical carbon steel  
Slika 1: Entalpijska funkcija tipičnih ogljikovih jekel

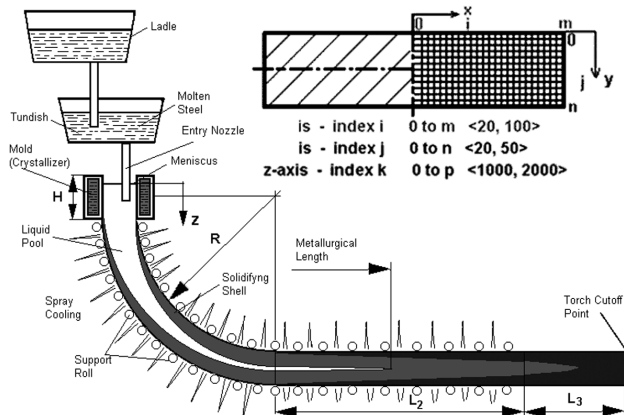


Figure 2: The mesh and definition of the coordinate system  
Slika 2: Mreža in opredelitev koordinatnega sistema

$$\frac{\partial H_v}{\partial \tau} = k \cdot \left( \frac{\partial^2 T}{\partial x^2} + \frac{\partial^2 T}{\partial y^2} + \frac{\partial^2 T}{\partial z^2} \right) + w \cdot \frac{\partial H_v}{\partial z} \quad (2)$$

The enthalpy  $H_v$  as a thermodynamic function of temperature must be known for each specific steel. It is dependent on the composition of the steel and on the rate of cooling. The dependence of the function  $H$  for typical carbon steel is in Figure 1.

Figure 2 shows that the task is symmetrical along the  $x$ -axis; it is therefore sufficient to investigate only half of the cross-section with the following boundary conditions (3a-3e)

1.  $T = T_{cast}$  at the meniscus (3a)
2.  $-k \frac{\partial T}{\partial n} = 0$  at the plane of symmetry (3b)
3.  $-k \frac{\partial T}{\partial n} = h \cdot (T_{surface} - T_a)$  in the mould (3c)

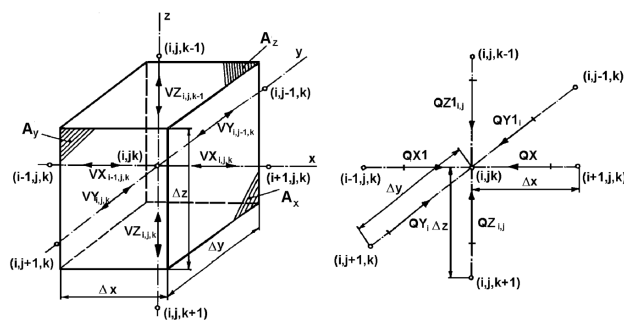


Figure 3: The thermal balance diagram for the general nodal point of the network  
Slika 3: Diagram toplotnega ravnovesja v splošni točki mreže

Table 1: Selected classes of steel with their compositions used for calculation  
Tabela 1: Izbrani razredi jekel in njihove sestave, w/%

Class	Group	Ceq	C	Mn	Si	P	S	Cu	Ni	Cr	Mo	V	Ti	Al	Nb	Tsol	Tliq
11325	2	0.067	0.050	0.225	0.025	0.010	0.010	0.150	0.150	0.150	0.040	0.050	0.0025	0.045	0.030	1499.8	1529.8
21026	5	0.235	0.150	1.075	0.300	0.0175	0.010	0.150	0.200	0.100	0.040	0.045	0.001	0.040	0.015	1451.4	1514.2
31087	3	0.275	0.190	1.450	0.200	0.015	0.010	0.100	0.150	0.100	0.040	0.010	0.001	0.040	0.030	1438.7	1510.6
11500	4	0.326	0.270	0.550	0.275	0.015	0.010	0.150	0.150	0.125	0.040	0.050	0.025	0.040	0.030	1423.2	1507.4
13180	6	0.826	0.75	1.050	0.250	0.0175	0.010	0.125	0.200	0.150	0.050	0.100	0.050	0.040	0.025	1322.7	1467.7

$$4. -k \frac{\partial T}{\partial n} = h \cdot (T_{surface} - T_a) + \sigma \varepsilon \cdot (T_{surface}^4 - T_a^4)$$

in the secondary and tertiary cooling zones (3d)

$$5. -k \frac{\partial T}{\partial n} = q$$

beneath the support rollers (3e)

The initial condition for solving is the setting of the initial temperature in individual points of the mesh. A suitable value is the highest possible temperature, i.e., the casting temperature.

Figure 3 illustrates the thermal balance of an elementary volume (general nodal point  $i, j, k$ ) of the network.

An unknown enthalpy of the general nodal point of the slab in the next time step ( $\tau + \Delta\tau$ ) is expressed by the explicit formula:

$$H_{v_{i,j,k}}^{(\tau + \Delta\tau)} = H_{v_{i,j,k}}^{(\tau)} + (QZ1_{i,j} + QZ2_{i,j} + QY1_{i,j} + QY2_{i,j} + QX1 + QX2) \frac{\Delta\tau}{\Delta x \cdot \Delta y \cdot \Delta z} \quad (4)$$

The heat flow through the general nodal point ( $i, j, k$ ) in the  $z$ -direction is described by the following equations

$$QZ_{i,j} = VZ_{i,j,k} (T_{i,j,k+1}^{(\tau)} - T_{i,j,k}^{(\tau)}) - A_z \cdot w \cdot H_{v_{i,j,k}}^{(\tau)} \quad (5)$$

$$\text{Where } VZ_{i,j,k} = k \cdot A_z / \Delta z$$

Figure 1 indicates how the temperature model for the calculated enthalpy in equation (4) determines the un-

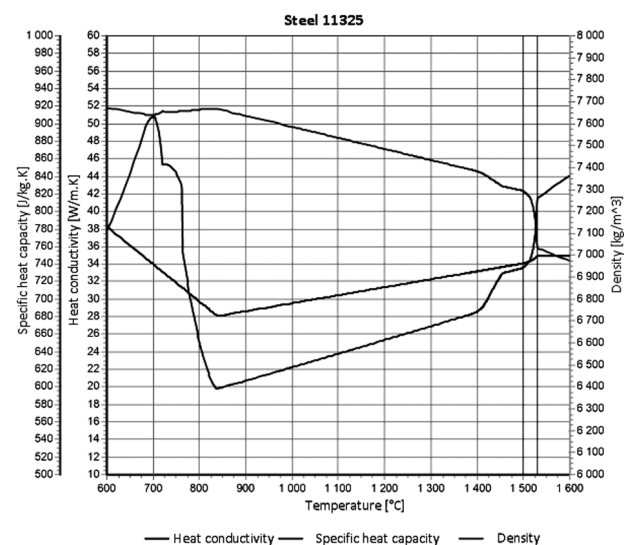


Figure 4: Thermophysical properties of the 11325 class steel from group 2 (first row of Table 1.)

Slika 4: Termofizikalne lastnosti jekla razreda 11325 iz skupine 2 (prva vrstica table 1)

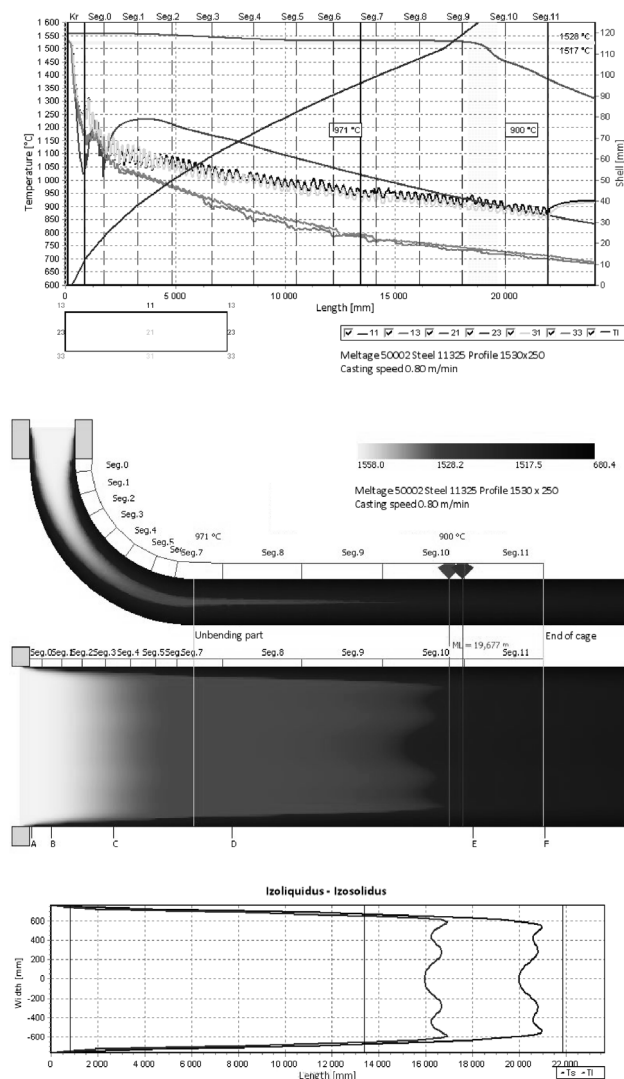


Figure 5: Temperature field of the 11325 class steel slab  
Slika 5: Temperaturno polje jekla razreda 11325

known temperature. The enthalpy function is not known as an analytical function but as a set of table values, and therefore the inverse calculation of the temperature is numerically a very demanding problem. In the dynamic model where the calculation must run at least as fast as the flow of the process in real time, the method in which the interpolation values are calculated at 0.1 °C intervals even before the actual calculation was chosen. The temperature for the relevant enthalpy is then determined using modern search methods in the table.

### 3 THE EFFECT OF THE CHEMICAL COMPOSITION ON THE RESULTANT TEMPERATURE FIELD

A real concasting operation casts up to several hundred classes of steel. It would therefore be difficult to set the concasting and other relevant technological parameters for all of them. That is why steels are

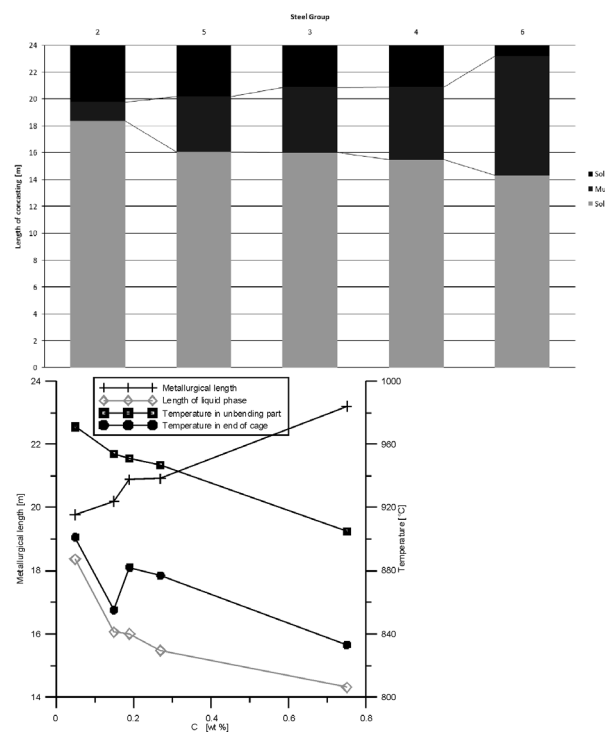


Figure 6: Comparison of the length of the liquid phase and the metallurgical length for various classes of steel  
Slika 6: Primerjava dolžine tekoče faze in metalurške dolžine za različne razrede jekla

subdivided into groups, mostly according to their carbon content, preferably according to the so-called equivalent carbon content, given by:

$$C_{eq} = C - 0.1Si + 0.04Mn - 0.04Cr + 0.1Ni - 0.1Mo \quad (6)$$

A single class of steel was selected from each group for the analyses below. Table 1 contains the recommended compositions of these steels, together with the temperatures of the liquidus and solidus. Figure 4 illustrates an example of the dependence of the thermo-physical properties on the temperature for the 11325 class steel<sup>2</sup>. Figure 5 presents the calculated temperature field for this class of steel. These calculations were also performed for the remaining classes<sup>3</sup>. In order to analyse the influence of the chemical composition on the temperature field more clearly, the other concasting parameters were selected to be identical, i.e., a casting speed of 0.8 m/min, a superheating temperature of 30 °C and the profile of the slab equal to (1530 × 250) mm, just like the flow of water through the secondary-cooling zone. In practice, a different cooling mode is selected for each different class of steel.

Figure 6 proves the main parameters of the resulting temperature field as the effect of the chemical composition of five different steels.

### 4 CONCLUSIONS

This paper introduces a 3D numerical model of the temperature field (for the concasting of steel) in the form

of in-house software and has been implemented in the operations of EVRAZ VITKOVICE STEEL. The model includes the main thermodynamic transfer phenomena during the solidification of concasting. The presented model is a valuable computational tool and an accurate simulator for investigating transient phenomena in slab-caster operations, and for developing control methods, the choice of an optimum casting strategy for steel with different chemical compositions.

## NOMENCLATURE

$A$	area	[m <sup>2</sup> ]
$c$	specific heat capacity	[J/(kg K)]
$w(\text{C}_{\text{eq}})$	equivalent carbon content	%
$w(\text{C})$	mass composition of carbon	%
$h$	heat-transfer coefficient	[W/(m <sup>2</sup> K)]
$H_v$	volume enthalpy	[J/m <sup>3</sup> ]
$k$	heat conductivity	[W/(m K)]
$L_{\text{LIQ}}$	length of the liquid phase	[m]
$L_{\text{MET}}$	metallurgical length	[m]
$T$	temperature	[K]
$T_a$	ambient temperature	[K]
$T_{\text{cast}}$	melt temperature	[°C]
$T_{\text{surface}}$	temperature in unbending part	[°C]
$T_{\text{unbending}}$	temperature in unbending part	[°C]
$T_{\text{end}}$	temperature in end of cage	[°C]
$q$	specific heat flow	[W/m <sup>2</sup> ]

$QX, QY, QZ$	heat flows	[W]
$x, y, z$	axes in given direction	[m]
$u, v, w$	casting speed in given direction	[m/s]
$VX, VY, VZ$	heat conductivity	[W/K]
$\rho$	density	[kg/m <sup>3</sup> ]
$\sigma$	Stefan-Boltzmann constant	[W/(m <sup>2</sup> K <sup>4</sup> )]
$\varepsilon$	emissivity	[-]
$\tau$	time	[s]

## ACKNOWLEDGEMENTS

This analysis was conducted using a program devised within the framework of the GA CR Project No. 106/09/0940, 106/08/0606.

## 5 REFERENCES

- <sup>1</sup> J. Miettinen, Louhenkilpi, J. Laine, Solidification analysis package IDS. Proceeding of General COST 512 Workshop on Modelling in Materials Science and Processing, M. Rappaz and M. Kedro eds., ECSC-EC-EAEC, Brussels, Luxembourg, (1996)
- <sup>2</sup> A. Richard, Kai Liu Harding, Ch. Beckermann, A transient simulation and dynamic spray cooling control model for continuous steel casting, Metallurgical and materials transactions, 34B (2003) 6, 297–302
- <sup>3</sup> J. Stetina, The dynamic model of the temperature field of concast slab. Ph.D. Thesis, Technical University of Ostrava, Ostrava 2007, 106



## PREDICTION OF THE MECHANICAL PROPERTIES OF CAST Cr-Ni-Mo STAINLESS STEELS WITH A TWO-PHASE MICROSTRUCTURE

### NAPOVED MEHANSKIH LASTNOSTI LITIH Cr-Ni-Mo NERJAVNIH JEKEL Z DVOFAZNO MIKROSTRUKTURO

Milan Malešević, Jelena V. Tuma, Borivoj Šuštaršič, Predrag Borković

Institute of Metals and Technology, Lepi pot 11, 1000 Ljubljana, Slovenia  
milan.malesevic@imt.si

Prejem rokopisa – received: 2011-03-07; sprejem za objavo – accepted for publication: 2011-03-15

The results of mechanical tests on Cr-Ni-Mo stainless steels were analyzed to find a correlation between the Charpy-V impact toughness (*CVN*), the Vickers hardness (*HV5*) and the tensile strength  $R_m$  with the time and temperature of isothermal ageing. These tests were performed on three alloys with different chemical compositions and delta ferrite contents. The alloys were designated as the volume fractions of *A* (2 %), *B* (11 %) and *C* (with 27 % of delta ferrite). All the results were then described with the most suitable function. After that, a computer program for the prediction (calculating) of the mechanical properties (impact toughness *CVN*, Vickers hardness *HV5* and tensile strength  $R_m$ ) was made. The program application was written in the Visual Basic 6 environment. With this program it is possible to predict the change of the *CVN*, *HV5* and  $R_m$  of Cr-Ni-Mo stainless steels depending on time, aging temperature and the delta ferrite content of the material for aging temperatures from 290 °C to 350 °C (step 10 °C), and delta ferrite content from 2 % to 27 % (step 1 %). To avoid mistakes and to focus on a time period of practical importance, the aging time is limited to 40 years. The principle used here allows us to predict the mechanical properties of other materials with any other chemical composition. However, the confirmation of this requires additional experimental data.

Keywords: Cr-Ni-Mo stainless steels, impact toughness, Vickers hardness, tensile strength, delta ferrite content, empirical method, program application, Visual Basic 6

Na osnovi mehanskih preizkusov na Cr-Ni-Mo nerjavnem jeklu smo izvršili analizo vpliva temperature in časa izotermnega žarjenja na Charpy-V udarno žilavost (*CVN*), trdoto po Vikersu (*HV5*) in natezno trdnost ( $R_m$ ). Mehanske preizkuse smo izvršili pri treh zlitinah z različno kemijsko sestavo in vsebnostjo delta ferita. Zlitine smo označili z volumenski deleži *A* (2 %), *B* (11 %) in *C* (27 % delta ferita). Vse eksperimentalne rezultate smo opisali z najbolj primerno empirično funkcijo. Potem smo izdelali računalniški program za napoved (izračun) mehanskih lastnosti (*CVN*, *HV5* in  $R_m$ ) v odvisnosti od časa in temperature izotermnega žarjenja (staranja). Programska aplikacija je napisana v okolju Visual Basic 6. S tem programom je mogoče predvideti spremembo *CVN*, *HV5* in  $R_m$  Cr-Ni-Mo nerjavnega jekla, odvisno od časa, temperature staranja in vsebnosti delta ferita v materialu, za temperature staranja od 290 °C do 350 °C (korak 10 °C) in vsebnosti delta ferita od 2 % do 27 % (korak 1 %). Da bi se izognili napakam in se osredinili na časovno obdobje, ki ima praktični pomen, je čas omejen za obdobje 40 let. Z uporabo istega načela je tudi mogoče napovedati mehanske lastnosti drugih materialov z drugačno kemijsko sestavo. Za potrditev tega potrebujemo nove eksperimentalne podatke.

Ključne besede: nerjavna jekla Cr-Ni-Mo, udarna žilavost, trdota po Vikersu, natezna trdnost, vsebnost delta ferita, empirična metoda, programska aplikacija, Visual Basic 6

## 1 INTRODUCTION

The idea is to make a computer-program application able to simulate the process of aging of Cr-Ni-Mo stainless steels with a two-phase microstructure. These steels are used for the structural elements of older nuclear power plants<sup>1,2,3</sup>. On the basis of the input data (aging time, aging temperature and delta ferrite content of the steel) this program calculates and predicts the impact toughness, hardness and tensile strength of a given steel. It is also able to draw diagrams for the change of each mechanical property with respect to the aging time. This program is based on pure experimental results and methods.

## 2 EXPERIMENTAL PART

### 2.1 Experimental data

The results obtained on three different alloys, designated as *A* (with the volume fraction 2 % of  $\delta$ -ferrite), *B* (11 %) and *C* (27 %) were used<sup>4</sup>. The alloys were aged (isothermally annealed) for up to two years at three different temperatures, 290 °C, 320 °C and 350 °C, for one day, seven days, one month, six months, one year and two years. The impact toughness (**Table 3**), Vickers hardness (**Table 4**) and tensile strength (**Table 5**) were determined on these samples. The tests were also performed before the aging. All the tests were performed at room temperature (20 °C). The average delta ferrite content (**Table 2**) was determined with a FERITSCOPE MP30, Fisher, Germany.

**Table 1:** Average chemical composition of the selected alloys in volume fractions ( $\phi/\%$ )

**Tabela 1:** Povprečna kemična sestava izbranih zlitin ( $\phi/\%$ )

	A	B	C
C	0.06	0.07	0.06
Si	0.43	0.67	1.68
Mn	1.59	1.04	0.67
P	0.03	0.03	0.03
S	0.01	0.01	0.01
Cr	18.0	21.7	20.8
Ni	11.9	11.0	9.0
Mo	1.84	2.03	2.46

**Table 2:** Average delta ferrite content ( $\phi/\%$ )

**Tabela 2:** Povprečna vsebnost delta ferita ( $\phi/\%$ )

Alloy	A	B	C
Delta ferrite content	2	11	27

**Table 3:** Average Charpy impact toughness; CVN/J

**Tabela 3:** Povprečna udarna žilavost po Charpyju; CVN/J

Alloy	A	B	C
Initial state	130	134	107
Aging time (h)	Aging temperature 290 °C		
24	138	109	127
168	163	87	123
720	119	117	120
4320	101	108	113
8760	149	103	61
17520	121	62	53
Aging time (h)	Aging temperature 320 °C		
24	145	112	106
168	112	80	108
720	106	94	54
4320	176	57	33
8760	113	33	48
17520	105	34	30
Aging time (h)	Aging temperature 350 °C		
24	155	112	103
168	102	69	76
720	155	47	28
4320	145	50	19
8760	100	34	21
17520	99	38	14

**Table 4:** Average Vickers hardness  $H_V/HV5$ 
**Tabela 4:** Povprečna trdota po Vickersu  $H_V/HV5$ 

Alloy	A	B	C
Initial state	138	174	207
Aging time (h)	Aging temperature 290 °C		
24	135	167	208
168	132	171	213
720	139	170	210
4320	132	166	207
8760	140	164	208
17520	133	174	218
Aging time (h)	Aging temperature 320 °C		
24	134	169	208
168	133	168	212
720	134	172	220
4320	134	173	221
8760	134	175	224
17520	139	183	238
Aging time (h)	Aging temperature 350 °C		
24	133	163	210
168	141	174	214
720	139	182	228
4320	131	181	230
8760	134	181	233
17520	153	187	248

**Table 5:** Average tensile strength  $R_m$  /MPa

**Tabela 5:** Povprečna natezna trdnost  $R_m$  /MPa

Alloy	A	B	C
Initial state	371	556	684
Aging time (h)	Aging temperature 290 °C		
24	472	552	675
168	489	560	714
720	503	550	712
4320	501	561	682
8760	501	561	732
17520	479	560	705
Aging time (h)	Aging temperature 320 °C		
24	481	546	666
168	494	556	717
720	480	570	732
4320	490	568	722
8760	491	580	696
17520	492	604	765
Aging time (h)	Aging temperature 350 °C		
24	488	560	695
168	485	563	713
720	490	571	733
4320	486	594	766
8760	485	608	760
17520	495	610	824

## 2.2 Modelling of the functions

The methodology of this procedure is explained on the alloy C and the impact-toughness results, as an example. All the results were introduced into a diagram and the characteristic points of the impact-toughness functions for all three aging temperatures are generated. For this operation we used a simple program for drawing diagrams called Graph<sup>5</sup>. The distribution of these characteristic points is shown in **Figure 1**. Each point represents the average value of the impact toughness obtained by the Charpy-V test. Then the program generates automatically the most suitable and optimum function (**Figure 2**), which for the impact toughness is:

$$CVN = \frac{a+b \cdot t}{1+c \cdot t+d \cdot t^2} \quad (1)$$

The most suitable and appropriate selected empirical functions describing the change of hardness and tensile strength with time at a constant temperature are:

$$H_V = a \cdot t^b \quad (2)$$

$$R_m = a \cdot t^b \quad (3)$$

where CVN (J) is the impact Charpy-V toughness,  $a$ ,  $b$ ,  $c$ ,  $d$  are the empirically determined materials coefficients, and  $t$  (h) is the time

## 2.3 Creating a database of functions

Only functions for the temperatures 290 °C, 320 °C and 350 °C could be developed from the available experimental data. However, the goal was also to predict the changes of the impact toughness at intermediate temperatures in between the experimental temperatures, i.e., for (300, 310, 330 and 340) °C. It was assumed that the

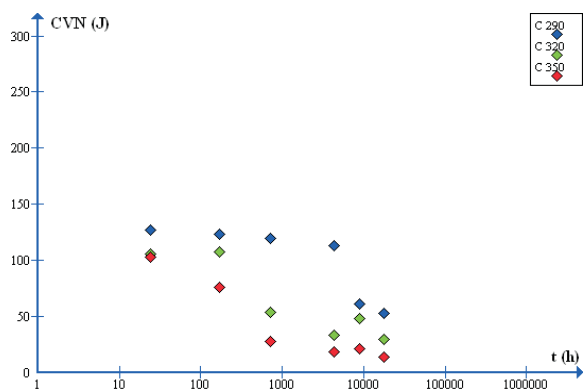


**Figure 1:** Distribution of the impact-toughness characteristic points of alloy C, at 290, 320 and 350°C

**Slika 1:** Karakteristične točke udarne žilavosti zlitine C, pri (290, 320 in 350) °C

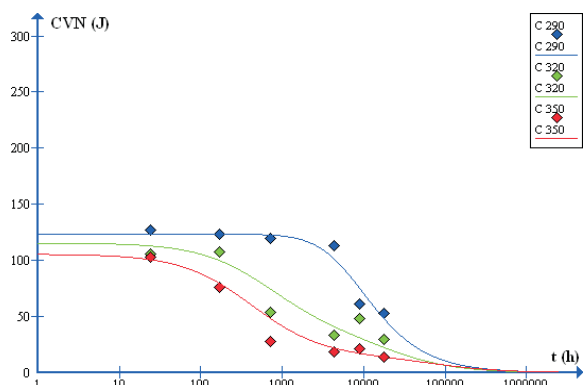


**Figure 2:** Impact-toughness functions of alloy C, at (290, 320 and 350) °C

**Slika 2:** Funkcije udarne žilavosti zlitine C, pri (290, 320 in 350) °C

functions of the temperatures 300 °C and 310 °C lie between the functions for 290 °C and 310 °C, while the functions for 330 °C and 340 °C lie between 320 °C and 350 °C.

For the determination of the characteristic points of the functions for intermediate temperatures some characteristic mathematical relations were used. The relation (4) is determined on the basis of the diagram in **Figure 3**, where all the important points for the temperatures

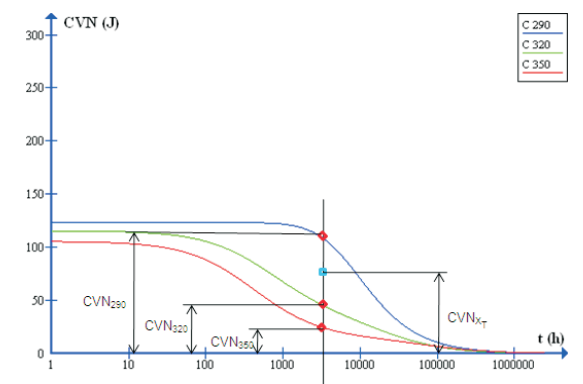


**Figure 3:** Characteristic values from equation (4)

**Slika 3:** Značilne vrednosti iz enačbe (4)

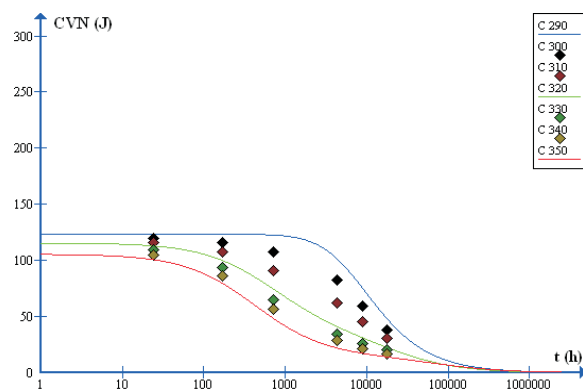


**Figure 4:** Calculating the points for the (300, 310, 330 and 340) °C functions

**Slika 4:** Izračun točk za funkcije (300, 310, 330 in 340) °C

between 290 °C and 320°C are marked. The same principle is used for the temperatures between 320 °C and 350°C and the relation (5) was obtained.

$$\begin{aligned} (CVN_{290} - CVN_{320}) : (CVN_{290} - CVN_{x_1}) &= (320 - 290) : (x_1 - 290) \\ \Rightarrow (CVN_{290} - CVN_{x_1}) \cdot (320 - 290) &= (CVN_{290} - CVN_{320}) (x_1 - 290) \\ \Rightarrow CVN_{290} - CVN_{x_1} &= \frac{(CVN_{290} - CVN_{320}) \cdot (x_1 - 290)}{320 - 290} \quad (4) \\ \Rightarrow CVN_{x_1} &= \frac{(CVN_{290} - CVN_{320}) \cdot (x_1 - 290)}{320 - 290} \end{aligned}$$

$$\begin{aligned} (CVN_{320} - CVN_{350}) : (CVN_{320} - CVN_{x_1}) &= (350 - 320) : (x_1 - 320) \\ \Rightarrow (CVN_{320} - CVN_{x_1}) \cdot (350 - 320) &= (CVN_{320} - CVN_{350}) (x_1 - 320) \\ \Rightarrow CVN_{320} - CVN_{x_1} &= \frac{(CVN_{320} - CVN_{350}) \cdot (x_1 - 320)}{350 - 320} \quad (5) \\ \Rightarrow CVN_{x_1} &= \frac{(CVN_{320} - CVN_{350}) \cdot (x_1 - 320)}{350 - 320} \end{aligned}$$

With the help of these two relations (4 and 5) all the characteristic points for all the functions were calculated. During the next step the functions were determined and generated. These functions now describe the way that the impact toughness of alloy C changes with time, at ageing temperatures of (290, 300, 310, 320, 330, 340 and 350) °C. The same principle as for the impact toughness was used to determine the functions for the Vickers hardness (2) and the tensile strength (3), for all three alloys A, B

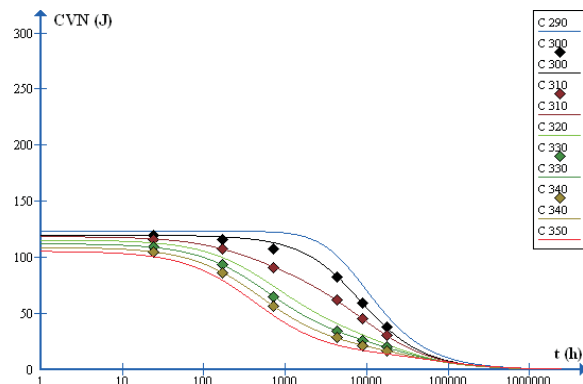


**Figure 5:** Generating the functions for (300, 310, 330 and 340) °C

**Slika 5:** Prikaz generiranja funkcij od (300, 310, 330 in 340) °C

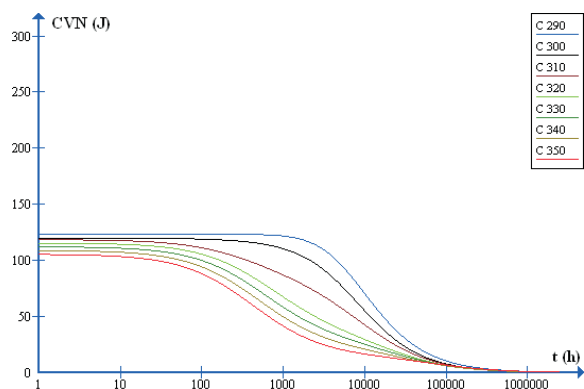


**Figure 6:** All *C* functions from 290 °C to 350 °C  
**Slika 6:** Vse *C* funkcije od 290 °C do 350 °C

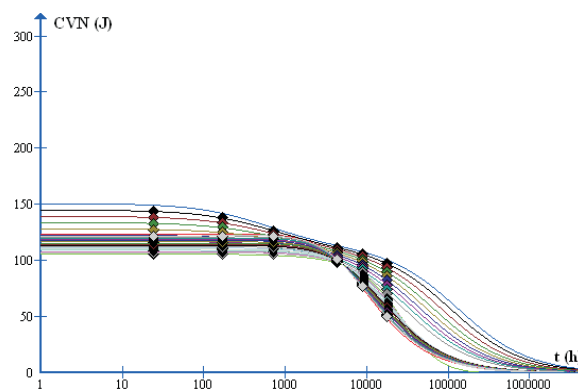


**Figure 9:** Generating the functions for all delta ferrite contents between (2, 11 and 27) %, at an aging temperature of 290 °C  
**Slika 9:** Generiranje funkcij za vse vsebnosti delta ferita med (2, 11 in 27) %, pri temperaturi 290 °C

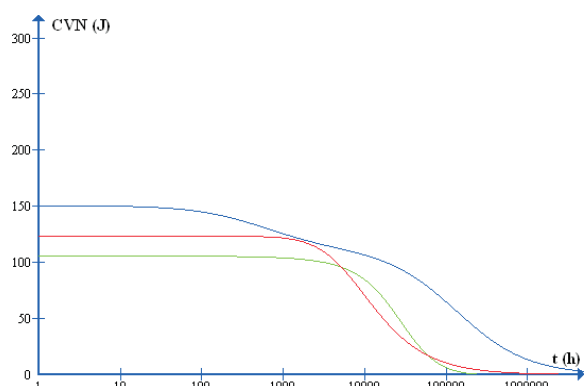


**Figure 7:** Functions of alloy *A* (blue), *B* (green) and *C* (red) at an aging temperature of 290 °C  
**Slika 7:** Funkcije zlitin *A* (modra), *B* (zelena) in *C* (rdeča) pri temperaturi staranja 290 °C

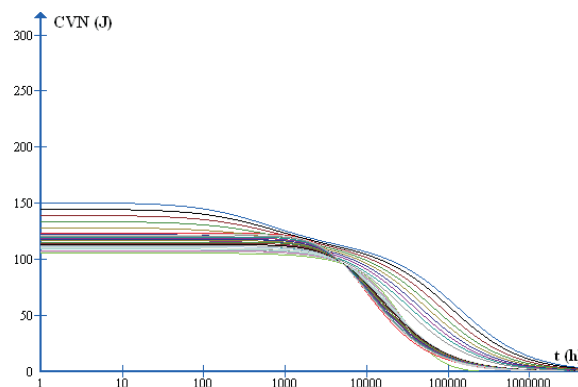


**Figure 10:** Functions for delta ferrite contents between (2, 11 and 27) %, at an aging temperature of 290 °C  
**Slika 10:** Funkcije za vsebnosti delta ferita med (2, 11 in 27) %, pri temperature staranja 290 °C

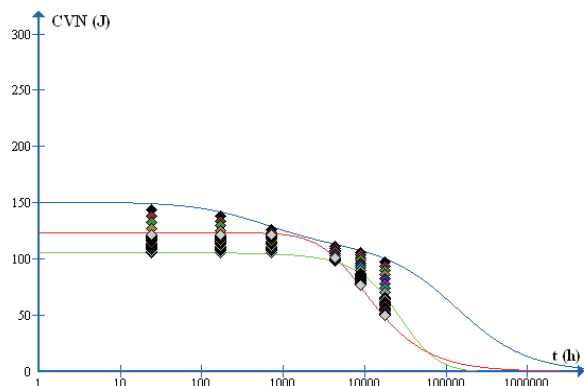


**Figure 8:** Calculating the points for functions with a delta ferrite content between (2, 11 and 27) %, at an aging temperature of 290 °C  
**Slika 8:** Izračun točk za funkcije z vsebnostjo delta ferita med (2, 11 in 27) % pri temperaturi staranja 290 °C

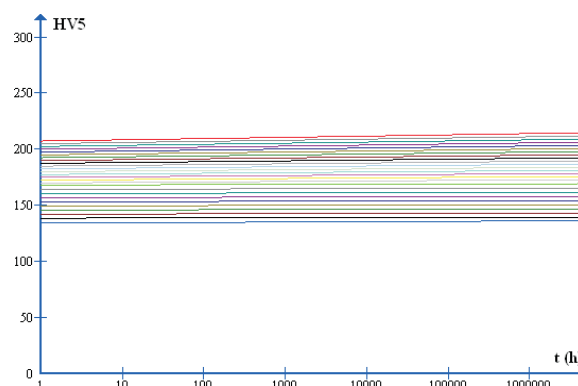


**Figure 11:** Functions of Vickers hardness for delta ferrite contents between (2, 11 and 27) % and an aging temperature of 290 °C  
**Slika 11:** Funkcije Vickersove trdote za vsebnosti delta ferita med (2, 11 in 27) % in temperaturo staranja 290 °C

and *C*. Subsequently, the functions had to be divided according to the temperatures, i.e., divided into 7 groups for the ageing temperatures (290, 300, 310, 320, 330, 340 and 350) °C. The functions of the alloys *A*, *B* and *C* at the ageing temperature of 290 °C are shown in **Figure 7**. At the next step the functions for the alloys which have a delta ferrite content between the three charac-

teristic values of (2, 22 and 27) %, were determined by covering of all the delta ferrite contents between 2 % and 27 % (step 1). This is shown in **Figures 8, 9 and 10**. The same principle is used for calculating the functions for the Vickers hardness and tensile strength changes. These

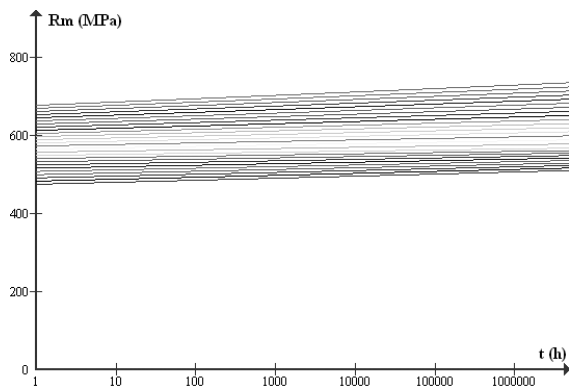


Figure 12: Functions of tensile strength for delta ferrite contents between 2 % and 27 % and an aging temperature of 290°C

Slika 12: Funkcije natezne trdnosti za vsebnosti delta ferita med 2 % in 27 % ter temperaturo staranja

ID	Field1	Field2	Field3	Field4	Field5
2	131.85498	0.1189022	0.000873106	2.2458677E-08	
3	133.4828	4.822271	0.038179437	1.0024048E-06	
4	139.4828	5.122271	0.04473837	1.1324048E-06	
5	137.44318	2.9696777	0.027883283	7.2286015E-07	
6	137.17977	2.2810663	0.023504677	6.1692755E-07	
7	137.20803	1.8757987	0.021416267	5.700671E-07	
8	137.40357	1.3808586	0.020233367	5.4824076E-07	
9	137.61922	1.3241139	0.019426528	5.3835786E-07	
10	137.88067	1.1180297	0.018879187	5.3839697E-07	
11	137.80433	0.8957298	0.018136087	5.3160628E-07	
12	133.54119	0.75207943	0.015551288	4.7916884E-07	
13	129.72055	0.62082151	0.012299916	4.2194048E-07	
14	126.5468	0.51856536	0.011882375	3.7481795E-07	
15	123.80158	0.43153354	0.0098712786	3.3341422E-07	
16	121.4124	0.3613676	0.0086042663	2.9712314E-07	
17	119.26062	0.30233401	0.007524935	2.6375125E-07	
18	119.26062	0.2933401	0.007248935	2.3375125E-07	
19	119.26062	0.28233401	0.00724935	2.3375125E-07	
20	118.86062	0.26233401	0.00724935	2.3375125E-07	
21	110.87665	0.092932792	0.003271347	0.7422431E-07	
22	110.87665	0.09392792	0.003571347	0.7422431E-07	
23	109.87665	0.09392792	0.003571347	1.0422431E-07	
24	108.75027	0.075125886	0.0031952639	8.3244839E-08	
25	107.71818	0.05934872	0.0028745184	6.382118E-08	
26	106.80541	0.046246797	0.0020668701	4.6271161E-08	
27	105.56396	0.035737785	0.0023693144	3.0589798E-08	

Figure 13: Database of functions of the impact toughness

Slika 13: Baza podatkov funkcij udarne žilavosti

ID	Field1	Field2	Field3
2	130.94838	0.0077963995	
3	133.47601	0.0095118391	
4	136.36942	0.010760218	
5	139.2841	0.011926909	
6	142.19119	0.013041852	
7	145.11171	0.014091424	
8	148.03118	0.015091069	
9	150.97042	0.016027655	
10	153.90134	0.016926906	
11	157.24343	0.017832558	
12	159.13435	0.018518611	
13	161.42842	0.018522159	
14	163.71907	0.018878696	
15	166.00696	0.019223082	
16	168.29898	0.019557387	
17	170.5957	0.019876819	
18	172.88895	0.020190965	
19	175.17929	0.020495018	
20	177.47368	0.020790728	
21	179.77256	0.021073602	
22	182.06797	0.021352505	
23	184.36033	0.021622928	
24	186.65667	0.021886373	
25	188.95736	0.022138613	
26	191.25456	0.022387896	
27	193.70505	0.022492301	

Figure 14: Database of functions of the Vickers hardness

Slika 14: Baza podatkov funkcij Vickersove trdote

ID	Field1	Field2	Field3
2	484.88228	0.0009583562	
3	489.07065	0.0027766891	
4	493.63342	0.0044748894	
5	498.2334	0.0061107043	
6	502.88549	0.0076805062	
7	507.59043	0.0091887284	
8	512.32854	0.01064257	
9	517.10149	0.01210456	
10	521.92441	0.013393808	
11	527.51971	0.014488886	
12	533.79045	0.015280355	
13	540.81875	0.015940556	
14	547.8525	0.016387518	
15	554.88732	0.016914937	
16	561.93235	0.01742561	
17	568.98314	0.017919522	
18	576.03832	0.018399148	
19	583.09346	0.018864386	
20	590.15784	0.019315707	
21	597.22696	0.019753015	
22	604.29968	0.020178483	
23	611.3715	0.020591949	
24	618.45182	0.020993718	
25	625.53608	0.021383641	
26	632.62333	0.021763651	
27	639.70703	0.022492301	

Figure 15: Database of functions of the tensile strength

Slika 15: Baza podatkov funkcij natezne trdnosti

functions (the example of the aging temperature of 290 °C) are shown in Figures 11 and 12.

### 2.3.1 Saving the functions in the Microsoft Office Access database

As we can see, the selected functions are determined with different coefficients. The functions for the impact toughness with four, and functions for Vickers hardness and tensile strength with only two, coefficients. For this reason, all the functions are saved into the database simply by saving their coefficients. Examples of functions saved are shown in Figures 13, 14 and 15.

### 2.4 Program application

The program application was written in the Visual Basic 6 environment and was connected, using the

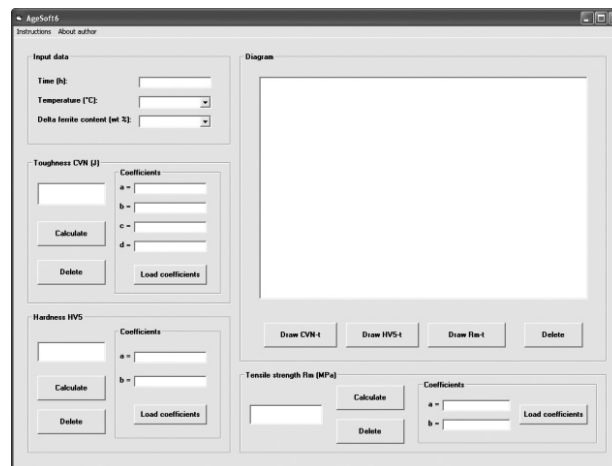


Figure 16: Main window of the "AgeSoft6" program

Slika 16: Glavno okno "AgeSoft6" programa

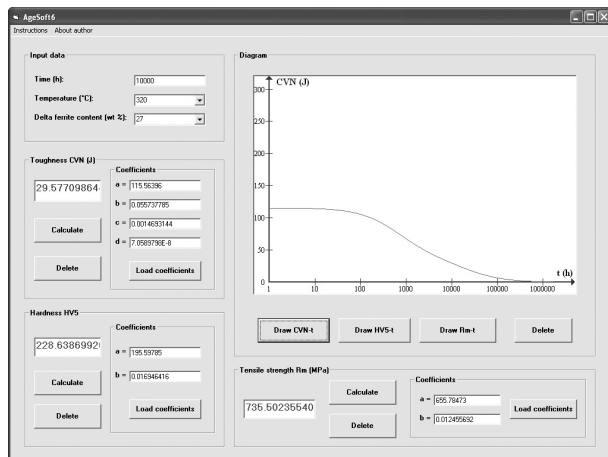


Figure 17: Calculated values  
Slika 17: Izračunane vrednosti

program code, with Microsoft Office database of functions. The main window of this program, called "AgeSoft6", is shown in Figure 16. The working principle of "AgeSoft6" is very simple. The user first inputs the "input data" and then on the basis of the input data, the software selects the appropriate function from the database. Next, the software includes the function coefficients into the equation, written in program code and calculates the results. Except for the modes for calculating the mechanical properties, there is also a mode for drawing the diagrams that show us how each function of each mechanical property changes over time. One example with calculated values and the CVN-t diagram for the alloy with 27 % of delta ferrite, aged at 320 °C for 10 000 h, is shown in Figure 17.

### 3 RESULTS AND DISCUSSION

With this program it is possible to predict the affect of the ageing time, temperature and the content of delta ferrite, for ageing temperatures from 290 °C to 350 °C (step of 10 °C) and delta ferrite contents from 2 % to 27 % (step of 1 %) on the Charpy impact toughness (CVN), Vickers hardness (HV5) and tensile strength ( $R_m$ ) of Cr-Ni-Mo stainless steels. Experimental results were available for an ageing time of 2 years. These results were used for the developing of functions that describe the change of the mechanical properties also for ageing

times longer than 2 years. With the help of these functions the program calculates the mechanical properties for up to 40 years (350 400 h) of ageing. However, mistakes in the results can occur, due to possible technical mistakes during the mechanical tests performed. If the calculated value of the CVN is lower than 20 J the program gives an alarm with a warning that the CVN is below a critical value.

### 4 CONCLUSIONS

The developed program is purely empirical and is made on the basis of the experimental data obtained for Cr-Ni-Mo stainless steels, so it corresponds in principle only to these kinds of steels with these chemical properties and ageing conditions. To have more value the program must be more universal. Therefore, in the next stage of the development of this program, experimental data for cast Cr-Ni duplex stainless steels will be used. The creation of a universal computer program that describes the ageing behaviour of any type of steel is probably too optimistic and at the moment this task is too difficult.

### 5 REFERENCES

- Jelena V. Tuma, Borivoj Šuštaršič, Franc Vodopivec: The effect of ageing temperature and time on the mechanical properties of Fe-NiCrMo alloys with different contents of delta ferrite, *Nucl. Eng. Des.*, 238 (2008) 7, 1511–1517
- Jelena V. Tuma, Borivoj Šuštaršič, Roman Celin, Franc Vodopivec: The mechanical properties of two-phase Fe-NiCrMo alloys at room temperature and 290 °C after ageing in the temperature range 290–350 °C, *Mater. Tehnol.* 43 (2009) 4, 179–187
- Roman Celin, Jelena V. Tuma, Boris Arzenšek: Effects of ageing a two-phase Fe-NiCrMo alloy on the strain hardening at room temperature and at 290 °C, *Mater. Tehnol.* 43 (2009) 5, 251–255
- B. Šuštaršič, J. V. Tuma, D. Kmetič, R. Celin, B. Arzenšek, B. Breskvar, F. Vodopivec, M. Godec, T. Drglin, J. Janovec, I. Naglič, R. Šturm, L. Kosec, B. Kosec, P. Škraba, N. Grubelj, P. McGuinness, B. Saje, Z. Račič, S. Šumlaj: Research of structural brittleness of two-phase stainless steels, Final report on the results of research project, Institute of metals and technology, University of Ljubljana, NTF-Department for materials and metallurgy, Ljubljana, 2004.
- Graph – is an open source application used to draw mathematical graphs in a coordinate system. The program makes it very easy to visualize a function and paste it into another program. It is also possible to do some mathematical calculations on the functions. Copyright © 2009 by Ivan Johansen

## RELATIONSHIP BETWEEN MECHANICAL STRENGTH AND YOUNG'S MODULUS IN TRADITIONAL CERAMICS

### ODVISNOST MED MEHANSKO TRDNOSTJO IN YOUNGOVIM MODULOM PRI TRADICIONALNI KERAMIKI

Igor Štubňa<sup>1</sup>, Anton Trnák<sup>1,2</sup>, Peter Šín<sup>1</sup>, Radomír Sokolář<sup>3</sup>, Igor Medved<sup>1,2</sup>

<sup>1</sup>Dpt. of Physics, Constantine the Philosopher University, A. Hlinku 1, 949 74 Nitra, Slovakia

<sup>2</sup>Dpt. of Materials Engineering and Chemistry, Czech Technical University, Thákurova 7, 166 29 Prague, Czech Republic

<sup>3</sup>Institute of Building Materials, Faculty of Civil Engineering, Technical University, 602 00 Brno, Veveří 95, Czech Republic  
istubna@ukf.sk

*Prejem rokopisa – received: 2010-10-04; sprejem za objavo – accepted for publication: 2011-05-27*

A verification of theoretical linearity between mechanical strength and Young's modulus was performed with quartz porcelain samples both green and fired. The experiments were carried out at the room temperature and at elevated temperatures up to 1000 °C. The results obtained for green samples showed relatively scattered values  $\sigma_f(E)$  around the linear function. A regression coefficient of the linear fitting ( $R = 0.803$ ) is not sufficient for a clear linearity  $\sigma_f(E)$ . The relationship  $\sigma_f(E)$  is clearly linear for a fired sample and was confirmed in the temperature interval 20–1000 °C. For this case, the regression coefficient of the linear fitting is 0.976.

Key words: ceramics, Young's modulus, flexural strength, firing

Teoretična linearnost med mehansko trdnostjo in Youngovim modulom je bila preverjena na vzorcih iz kremenovega porcelana, zelenih in žganih. Poizkusi so bili izvršeni pri sobni temperaturi in pri povišanih temperaturah do 1000 °C. Pri rezultatih iz zelenih vzorcev je imela vrednost  $\sigma_f(E)$  precejšnje odmike od linearnosti. Regresijski koeficient linearnega ujemanja ( $R = 0.803$ ), kot jasno merilo linearnosti  $\sigma_f(E)$ , je premajhen. Odvisnost  $\sigma_f(E)$  je jasno linearna za žgane vzorce in je bila potrjena za vzorce, žgane v intervalu temperature 20–1000 °C. Za žgane vzorce je koeficient regresije 0.976.

Ključne besede: keramika, Youngov modul, upogibna trdnost, žganje

## 1 INTRODUCTION

Mechanical parameters are important characteristics of ceramic materials. Each ceramic product is mechanically stressed in technological processes during drying and firing and, as well as in actual service. Both flexural strength and Young's modulus are among the most important physical parameters of ceramic material and appear in theoretical models and calculations related to permissible loading the ceramic products. They also play crucial roles (together with a coefficient of thermal expansion and coefficient of thermal conductivity) in the calculation of the maximum firing rate.

The linear relationship between mechanical stress and strain follows directly from Hooke's law <sup>1</sup>. In the simplest one-dimensional case, the Hooke's law takes a form of  $\sigma = E\varepsilon$ , where  $\sigma = F/S$  is the stress ( $F$  is a loading force and  $S$  is area of the sample cross-section) and  $\sigma = \Delta l/l$  ( $\Delta l$  is extension/contraction of the sample and  $l$  is its initial length). A quantity  $E$  is Young's modulus which characterizes elastic properties of the sample material.

A measurement of Young's modulus based directly on the equation  $\sigma = E\varepsilon$  requires a relatively high stress to reach a measurable deformation. It can influence the structure of the tested material and create microcracks in

brittle materials such as ceramics. For that reason, a flexion of the sample is often used for ceramic materials. For example, by static three-point-bending, Young's modulus  $E$  and mechanical strength  $\sigma_f$  are determined by relations <sup>2</sup>

$$E = \frac{4Fl^3}{3\pi d^4 y}, \sigma_f = \frac{8F_f l}{\pi d^3} \quad (1a, 1b)$$

for a circular cross-section, where  $y$  is a flexion in the middle between the supports,  $l$  is a support span,  $d$  is a diameter of the sample and  $F_f$  is the loading force, at which a rupture occurred. These equations combined, provides the following

$$\sigma_f = \frac{6d}{l^2} y_f E \quad (2)$$

where  $y_f$  is flexion of the sample at the instant of the rupture. In analyzing other methods of simultaneous measuring of the mechanical strength and Young's modulus, the similar result is obtained. There is linearity between the mechanical strength and Young's modulus

$$\sigma_f = Ky_f E \quad (3)$$

where constant  $K$  contains dimensions of the sample and specific geometrical parameters of mechanical design of an experiment. The character of the parameter  $y_f$  is given via experiment, e.g. it is flexion (as in the described

example), or extension (contraction) of the sample in different experiments.

In contrast to the modulus of elasticity, values of flexural strength depend on the method used and on the dimensions of the sample. Ceramic material is characterized by fragility. Ceramic samples under mechanical load exhibit Hooke's law until reaching the critical deformation when a rupture of the sample occurs. A typical relationship between the flexion and loading force of the porcelain sample in the three-point-bending test is depicted in **Figure 1**.

Hypothetically, linearity between the mechanical strength and Young's modulus is valid when Young's modulus is measured, not simultaneously with mechanical strength, and even when different methods are used for their measurement, e.g., the static method for mechanical strength and dynamical method for Young's modulus.

The mechanical strength depends on the crack initiator presence in the most loaded area (e.g., in the middle of the sample if the three-point-bending is used). These initiators are not identical and produce the rupture of the samples at different loading forces and brings relatively high scatter of values of mechanical strength<sup>2,3</sup>. A relationship between the mechanical strength and the size of the sample is also known<sup>2,3,4,5</sup>. This property of the mechanical strength requires a relatively high number of samples. If a temperature dependence of the mechanical strength is required, e.g. for 10 temperatures, more than one hundred of samples must be used.

On the other side, elastic modulus is an integral value which does not depend on accidental occurrence of the big crack in the some peculiar place of the sample. That is, if some number of the samples is measured, the elastic modulus varies only in a small extent. Thus, we need substantially less number of samples for the measuring the elastic modulus than the mechanical strength. Beside that, the elastic modulus does not depend on the sample size.

An advantage of the measurement of the elastic modulus comparing to the mechanical strength can lead to a suggestion to utilize the linear relationship between these qualities and substitute the measurement of the

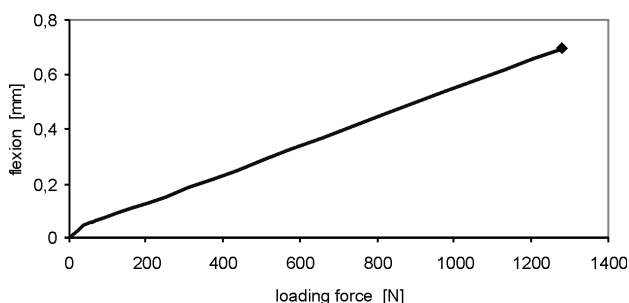


**Figure 1:** Dependence of the flexion on the loading force. Point (◆) corresponds with a rupture

**Slika 1:** Odvisnost med upogibom in obremenitvijo. Točka (◆) je označba za prelom

mechanical strength with the measurement of Young's modulus and having the value of Young's modulus, calculate the mechanical strength according to equation  $\sigma_f = \text{const} \cdot E$ . But we have never met such procedure. The linear relationship  $\sigma_f(E)$  was used for rejection of ceramic components with substandard mechanical properties<sup>6</sup>.

In our previous work<sup>7</sup>, we found the constant of proportionality in equation  $\sigma_f = \text{const} \cdot E$  for porcelains with reference to data given by porcelain manufacturers and research laboratories. The regression function for this relationship is  $\sigma_f \approx 1.21 \cdot 10^{-3} E$ ,  $R^2 = 0.6354$ , where  $\sigma_f$  is in MPa and  $E$  is in GPa. By using this relationship it is possible to evaluate approximately the flexural strength or Young's modulus if one of them is known. However, poor regression coefficient, which is a consequence of the different values taken from different sources, does not allow use equation  $\sigma_f = \text{const} \cdot E$  for sufficiently faithful and accurate conversion of the Young's modulus into the mechanical strength.

The objective of this paper is verification of equation  $\sigma_f = \text{const} \cdot E$  for green porcelain mixture during its firing and after the firing.

## 2 EXPERIMENTAL

Samples were made from a plastic mass of the mass fractions 50 % kaolin and clay, 25 % quartz, 25 % feldspar and water for manufacturing quartz porcelain high-voltage insulators. The cylindrical samples were made with the laboratory extruder. After drying in the open air, the samples contained  $\approx 1$  % of physically bounded water. The final dimensions of the green sample for thermomechanical analysis (mf-TMA) after drying, were  $\Phi 11 \text{ mm} \times 150 \text{ mm}$  and  $\Phi 11 \text{ mm} \times 120 \text{ mm}$  for flexural strength test. The volume mass of the green sample material  $1822 \text{ kg/m}^3$  was determined from the sample weight and dimensions.

Young's modulus was measured by a non-destructive sonic resonant technique – sensitive and reliable at elevated temperatures<sup>8</sup>. This method is based on measuring the resonance frequency, which is used for the calculating of Young's modulus, if the volume mass and

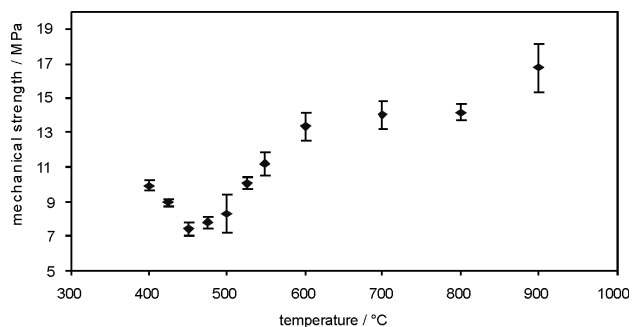


**Figure 2:** Mechanical flexural strength measured at the actual temperature

**Slika 2:** Upogibna trdnost, izmerjena pri naraščajoči temperaturi

dimensions of the sample are known. Using a flexural vibration, Young's modulus may be calculated for a cylindrical sample with a uniform square cross-section with the formula<sup>1,9</sup>

$$E = 1.26193 \left( \frac{l^2 f}{d} \right)^2 \rho T \quad (4)$$

where  $f$  is a resonant frequency of the fundamental mode,  $\rho$  is a volume mass,  $l$  is the length and  $d$  is the diameter of the sample. A value  $T$  is a correction coefficient, to be used if  $l/d < 20$ . For  $l/d = 15$  and Poisson's ratio  $\mu \approx 0.2$ , the correction coefficient  $T$  was taken from a table given in<sup>1</sup>,  $T = 1.01983$ .

Mechanical strength  $\sigma_f$  was determined by the three-point-bending test from Eq. (1b) at elevated temperatures during heating as well as at room temperature.

### 3 RESULTS AND DISCUSSION

Two experiments were performed. In the first, green samples were heated with a rate 5 °C/min and broken at the temperatures (400, 425, 450, 475, 500, 550, 600, 700, 800 and 900) °C in a regime of a constant rate of the loading force, 2 N/s. The results shown in **Figure 2** are similar to the results presented in<sup>10</sup>.

The green sample was also subjected to modulated-force mechanical thermal analysis (mf-TMA) to obtain values of Young's modulus at the temperatures referred to above. The Young's modulus was calculated from Eq. (4), where the resonant frequency was measured. The dimensions and mass of the sample assumed to be constant. The relationship Young's modulus versus temperature is depicted in **Figure 3**.

The relationship between mechanical strength and Young's modulus was verified, see **Figure 4**. The courses of graphs in **Figure 2** and **Figure 3** are similar, but the expected linear function, see **Figure 5**, is only approximately valid. In addition, the regression function in **Figure 4** does not fulfill a requirement  $\sigma_f \rightarrow 0$ , if  $E \rightarrow 0$ . A cause of the relatively low value of the regression coefficient of the linear fitting,  $R = 0.803$ , is uncertain up to now.

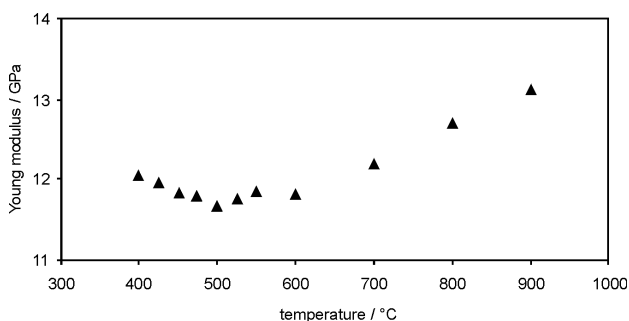


**Figure 3:** Young modulus measured at the actual temperature  
**Slika 3:** Youngov modul, izmerjen pri naraščajoči temperaturi

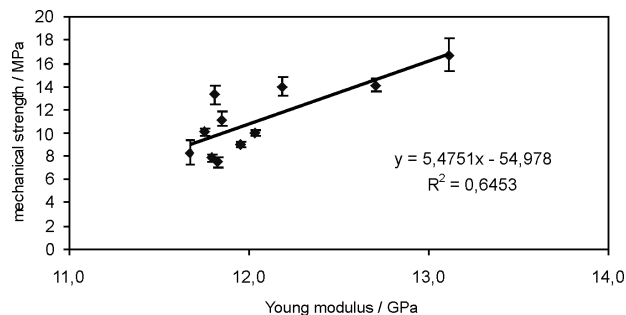


**Figure 4:** Relationship between mechanical strength and Young modulus measured at the actual temperature

**Slika 4:** Odvisnost med mehansko trdnostjo in Youngovim modulom pri različni temperaturi

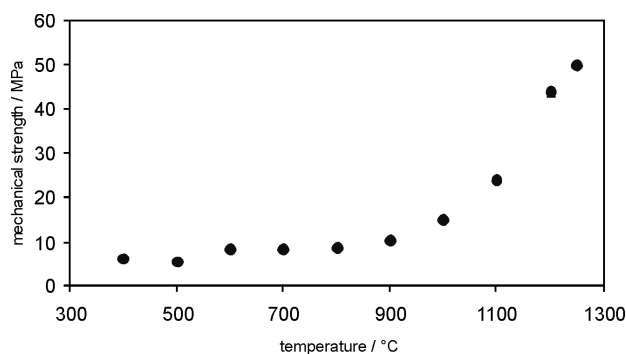


**Figure 5:** Dependence of the mechanical flexural strength on the firing temperature

**Slika 5:** Odvisnost upogibne trdnosti od temperature žganja

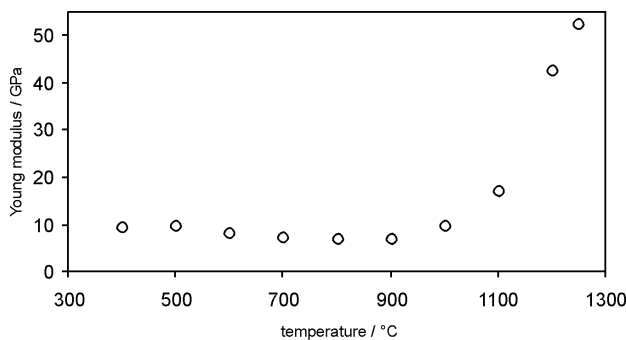


**Figure 6:** Dependence of Young modulus on the firing temperature

**Slika 6:** Odvisnost med Youngovim modulom in temperaturo žganja

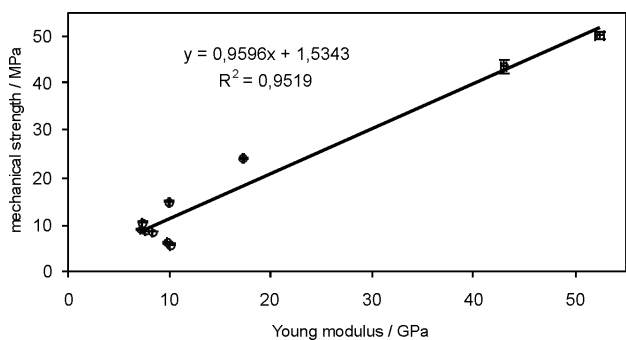


**Figure 7:** Relationship between mechanical strength and Young modulus measured at the room temperature

**Slika 7:** Odvisnost med mehansko trdnostjo in Youngovim modulom, izmerjena pri sobni temperaturi

In the second experiment, sets of 8 green samples were heated up to (400, 500, 600, 700, 800, 900, 1000, 1100, 1200 and 1250) °C with a rate 5 °C/min and then freely cooled in the oven. The sets of 8 samples were used for measuring Young's modulus and then for measuring the mechanical strength, both at room temperature. The results are displayed in **Figure 5, 6**, where the relationship between the mechanical strength and Young's modulus versus firing temperature is shown. A high similarity can be observed between these graphs. A relationship presented in **Figure 7** is very close to the linear dependence. The regression coefficient of the linear fitting  $R = 0.976$  is high and confirms the linearity between these material properties and the physically correct condition of  $\sigma_f \rightarrow 0$ , if  $E \rightarrow 0$  is nearly met. This permits using the dynamical measurement of Young's modulus of one sample rather than the measurement of the mechanical strength which typically requires more than 15 samples.

#### 4 CONCLUSION

A verification of theoretical linearity between mechanical strength and Young's modulus was performed with quartz porcelain samples, both green and fired. The experiments were carried out at room temperature and at elevated temperatures up to 1000 °C.

The results obtained for green samples showed relatively scattered values  $\sigma_f(E)$  around the linear function. Thus a regression coefficient of the linear fitting ( $R = 0.803$ ) is not sufficient for a conclusion with regard of a strong linearity  $\sigma_f(E)$ .

The relationship  $\sigma_f(E)$  is clearly linear for fired sample and confirmed in the temperature interval

20–1000 °C by the regression coefficient of the linear fitting of 0.976.

**Acknowledgements:** This work was supported by the grants VEGA 1/0216/09 and APVV SK-CZ-0005-09 and the Ministry of Education, Youth and Sports of the Czech Republic, under the project No. MSM: 6840770031. The authors thank the ceramic plant PPC Čab for providing green ceramic samples.

#### 5 REFERENCES

- <sup>1</sup> Schreiber, E. – Anderson, O. – Soga, N.: *Elastic constants and their measurements*. McGraw-Hill Book Co., New York 1973
- <sup>2</sup> Menčík, J.: *Strength and fracture of glass and ceramics*. SNTL Praha, 1990 (in Czech)
- <sup>3</sup> Bortzmeyer, D. – Langguth, G. – Orange, G.: Fracture mechanics of green products. *J. Europ. Ceram. Soc.*, 11 (1993), 9–16
- <sup>4</sup> Yondong Xu – Laifei Cheng – Litong Zhang – Dantao Yan – Chang You: Optimization of sample number for Weibull function of brittle materials strength. *Ceramics International*, 27 (2001), 239–241
- <sup>5</sup> Sedrakjan L. G.: *On statistical theory of strength*. Armjanskij institut stroitel'nykh materialov Jerevan 1958 (in Russian)
- <sup>6</sup> Moskovento, I. B.: Low-frequency acoustic control of physico-mechanical properties of refractory components. *Refractories and Industrial Ceramics*, 45 (2004), 289–293
- <sup>7</sup> Štubňa, I. – Sláviková, J. – Vozár, L.: Relationship between mechanical strength and Young's modulus of porcelain. *Industrial Ceramics*, 28 (2008), 153–154
- <sup>8</sup> Štubňa, I. – Trník, A. – Vozár, L.: Determination of Young's modulus of ceramics from flexural vibration at elevated temperatures. *Acta Acustica united with Acustica*, 97 (2011), 1–7
- <sup>9</sup> Standard ASTM C 1161-02b: *Standard test method for flexural strength of advanced ceramics*. (published in August 2002, Standard Documents, Philadelphia, USA)
- <sup>10</sup> Kozík, T. – Štubňa, I.: Mechanical strength of electroceramic material in dehydroxylation region. *Silikáty*, 25 (1981), 237–241 (in Slovakian)